

**ASSESSING THE UTILITY OF PASSIVE
OPTICAL POLARIMETRIC
OBSERVATIONS FOR THE
CHARACTERIZATION OF RESIDENT
SPACE OBJECTS**

**ÉVALUATION DE MESURES
POLARIMÉTRIQUES OPTIQUES
PASSIVES POUR LA
CARACTÉRISATION DES OBJECTS
SPATIAUX EN ORBITE TERRESTRE**

A Thesis Submitted to the Division of Graduate Studies
of the Royal Military College of Canada
by

Carl Clancy, BTech(Av)

Flight Lieutenant, Royal Australian Air Force

In Partial Fulfillment of the Requirements for the Degree of
Master of Science in Space Science

April, 2016

© This thesis may be used within the Department of National Defence
but copyright for open publication remains the property of the author.

Acknowledgments

I would like to thank the Royal Australian Air Force and the Royal Military College of Canada for the opportunity presented to me to study abroad. Most importantly, I would also like to thank my supervisor Major Donald Bédard and co-supervisor Dr. Gregg Wade for their enthusiasm, support and effort that have enabled this thesis. Thanks is due to my fellow students, Majors Wayne Karperien, Tyler Gill, Kelly Freitag, Lt. Jason Shaw and Mr. Alex Willison from the Space Surveillance Research Laboratory and Physics Department, for their advice, support, ideas and friendship. Thanks Samantha.

Abstract

The protection and management of valuable Earth orbits and operational satellites for military, commercial and research objectives are widely recognised as tasks of urgency and complexity. A critical component of this task is the tracking, characterization and identification of these active satellites as well as the space debris objects that pose a threat to them. As such, advances in methods and technologies to improve these functions are constantly being investigated. One such broad method being employed to enhance space situational awareness (SSA) is the analysis of sunlight reflected from Earth-orbiting satellites. There are a number of studies that have focused on studying variations in the intensity of the reflection to learn more about a satellite's operational status and activity, however there is very little research on how the polarization of the reflected light could be used to gain additional knowledge about the reflecting body. To understand the utility of doing so as a means of characterizing satellites and space debris objects, an experiment was designed and conducted to gain insight into the trends of relative reflective polarimetric behaviors of some common spacecraft construction materials.

For this thesis, five material samples were studied: two types of triple-junction photovoltaic cells, a bare 6061-T6 aluminum panel and a white-coated aluminum panel. The samples were mounted on a goniometer in which the illumination and reflection angles could be precisely controlled. The samples were then illuminated with a collimated unpolarised white light meant to simulate the Sun. The reflected light from the sample was then analysed using a dichroic linear polariser and a charge-coupled device (CCD) sensitive to optical wavelength light. From these measurements, the Stokes parameters were determined and the degree of linear polarisation and angle of polarisation calculated. The resulting values were plotted to allow an assessment of the trends in the polarimetric characteristics of each material with respect to illumination and observation geometries.

The findings from this research project yielded two significant outcomes. First, the results provide a general understanding of how the polarisation trends of the reflected light vary as the illumination and observational geometry is changed. Second, the polarisation trends differed between samples for a given illumination and observational geometry. It can be concluded from these results that studying the polarimetric characteristics of light reflected from resident space objects can aid in their characterization and ultimately contribute to the advancement of gaining and maintaining SSA.

Résumé

La protection et gestion d'orbites et de satellites opérationnels à des fins militaires, commerciales, et de recherche sont des tâches reconnues comme étant urgentes et complexes. Un élément essentiel de cette tâche est le suivi, la caractérisation et l'identification de ces satellites ainsi que les débris spatiaux qui constituent une menace pour eux. À ce titre, de nouvelles méthodes et technologies sont constamment recherchées afin d'améliorer ces fonctions. Une des méthodes utilisées pour perfectionner la connaissance de la situation spatiale (CSS) est l'analyse de la lumière du soleil qui est réfléchiée des satellites en orbite terrestre. Quoique qu'il y a plusieurs études qui ont porté sur l'analyse des variations de l'intensité cette lumière pour en apprendre davantage sur le statut et l'activité opérationnelle d'un satellite, il y a très peu de recherches qui ont cherchées à comprendre la façon dont la polarisation cette lumière pourrait être utilisée pour acquérir des connaissances supplémentaires sur le corps réfléchissant. C'est donc avec cet objectif que l'expérience, présentée dans cette thèse, fut établie. Le but de l'expérience était de mieux comprendre les tendances polarimétriques de la lumière réfléchiée par des matériaux communément utilisés dans la construction de satellites et véhicules spatiaux.

Cinq échantillons furent caractérisés, soit deux piles photovoltaïques, un panneau d'aluminium de type 6061-T6 sans recouvrement et un autre peint en blanc. Les échantillons ont été placés sur un goniomètre dans lequel la géométrie d'illumination et d'observation peuvent être contrôlés avec précision. Ces échantillons furent ensuite illuminés avec une lumière non-polarisée voulant simulée celle du soleil. La lumière réfléchiée de l'échantillon a ensuite été analysées en utilisant un polarisateur linéaire dichroïque et une caméra à dispositif de couplage de charge (CCD) sensible au longueur d'onde visible. Les paramètres de Stokes furent calculés et le degré de polarisation linéaire et l'angle de polarisation calculée. Les valeurs ainsi obtenues pour tous les échantillons ont été comparées pour permettre une évaluation des tendances dans les caractéristiques polarimétriques de chaque matériau par rapport à

l'éclairage et d'observation des géométries.

Les résultats de cette recherche ont mené à deux résultats importants. Premièrement, les résultats démontre que la polarisation de la lumière réfléchie de matériaux utilisés pour la construction de satellites varie en fonction de la géométrie d'illumination et d'observation. Deuxièmement, cette polarisation varie aussi selon l'échantillon qui était éclairé. Ces résultats permettent alors de conclure que l'étude des caractéristiques polarimétriques de la lumière réfléchie par des satellites et débris spatiaux pourraient potentiellement aider à la caractérisation de ces objets et ultimement contribuer à l'ammélioration de la CSS.

Contents

Acknowledgments	ii
Abstract	iii
Résumé	v
List of Tables	x
List of Figures	xi
List of Acronyms	xvi
1 Introduction	1
1.1 Background	1
1.2 Fundamentals of Polarimetry	2
1.2.1 The nature of light	2
1.2.2 Polarisation special cases	6
Fully polarised light	6
1.2.3 Unpolarised light	6
1.2.4 Partially polarised light	6
1.3 The Stokes Parameters	7
1.4 Polarisation states as Stokes parameters	10
1.4.1 Unpolarised/Natural light	11
1.4.2 Fully polarised light	11
1.4.3 Partially polarised light	12
1.4.4 Degree and angle of polarisation	13
1.4.5 Methods of polarisation	15
Reflection	15
Dichroism	18
Birefringence	18

	Scattering	19
	Polariser performance	21
1.5	Aim of the research project	21
1.6	Thesis outline	22
2	Literature survey	23
2.1	Fundamentals of reflectance	23
2.2	Phase angle	25
2.3	Photometry	27
	2.3.1 Broadband photometry	27
	2.3.2 Light curves	28
	2.3.3 Spectrophotometry	32
2.4	Polarimetry	34
	2.4.1 Active Polarimetry	34
	Spectralon	38
	2.4.2 Passive Polarimetry	38
	2.4.3 Un-resolved Issues	42
3	Laboratory Experiment	43
3.1	Introduction	43
	3.1.1 Background	43
	3.1.2 Experimental objectives and scope	43
	3.1.3 Experimental requirements	44
3.2	Experimental set-up	44
	3.2.1 Collimated white light	45
	3.2.2 Goniometer	46
	3.2.3 Analyzer	47
	3.2.4 Imaging system	49
	Lens	50
	Filter wheel	51
	CCD	51
	Alignment	52
3.3	Material samples	52
3.4	Data collection	54
	3.4.1 Master dark and bias	56
	3.4.2 Master flat	57
	3.4.3 Co-ordinate System	59
3.5	Data reduction	62
	3.5.1 Analysis area	63
	3.5.2 Stokes parameter retrieval	64

3.5.3	Polarisation retrieval	65
4	Results	67
4.1	Spectralon standard plate	68
4.2	Polarimeter analysis	73
4.2.1	Model comparison	73
4.2.2	Data replication	76
4.2.3	Error and uncertainty estimation	78
4.3	Integration time	78
4.4	General results	81
4.4.1	6061-T6 Aluminum	85
4.4.2	White-painted panel	87
4.4.3	Emcore TJPV cell	89
4.4.4	Azur TJPV cell	91
5	Discussion	93
5.1	Degree and angle of linear polarisation	94
5.2	Integration times	94
5.3	Geometry dependency	98
5.4	Characteristics of different materials	99
6	Conclusion	100
6.1	Future work	101
	Bibliography	102
	Appendices	106
A	Stokes Parameters	107
B	Mueller calculus and decomposition	109
B.1	Mueller calculus	109
B.2	Mueller decomposition	111
C	Results	112
C.1	Aluminum	112
C.2	White panel	115
C.3	Emcore TJPV cell	118
C.4	Azur TJPV cell	121
D	Resume	124

List of Tables

2.1	A review of notable recent works in the characterization of spacecraft materials using active polarimetry and Mueller matrix decomposition.	37
3.1	Operating parameters of the analyzing polaroid provided by Thorlabs, Inc [45].	48
3.2	Specifications for the Canon EF 24mm f/2.8 lens.	50
3.3	Specifications for the SBIG ST-2000XM CCD.	51

List of Figures

1.1	A conceptual illustration of the total \mathbf{E} wave (black) as a combination of two orthogonal waves. Note, the component X and Y waves are in phase.	4
1.2	An illustration showing the elliptical progression of the tip of the \mathbf{E} vector (black) in the $+Z$ direction, as a vector addition of out of phase, orthogonal X (red) and Y (blue) components.	5
1.3	Illustration of the combination of ellipse orientation and rotation light components. The axes are component wave amplitudes.	5
1.4	A representation of the polarisation ellipse showing the relationships between ellipse angles and electric field magnitudes, developed from Tinbergen [17].	9
1.5	Graphical description of the Stokes parameter conventions presented by Shurcliff [12] and Tinbergen [17], and adapted from the IAU convention [20]. In all cases direction of propagation is into the page.	10
1.6	Conceptual diagram showing main component considerations for reflection polarisation.	16
1.7	An illustration of reflection polarisation phenomenon occurring at Brewster's Angle.	17
1.8	A conceptual illustration of a simplified TJPV cell and the multi-layer nature of its reflective properties.	17
1.9	Illustration of the operating principle of a dichroic polariser, in this case a wire grid [14].	19
1.10	Illustration of unpolarised light incident upon birefringent material, in this case a Wollaston prism. Adopted from Hecht [14] and Pedrotti [15].	20
1.11	Illustration of polarisation induced by scattering. Adopted from Hecht [14].	20

2.1	Graphical description of bi-directional reflection distribution function, adapted from Nicodemus [26]	25
2.2	Constituent angles of Sun-satellite-observer geometry in the satellite body reference coordinate system as illustrated by Jolley [6, 29]. <i>Obs</i> points towards the observer, and <i>Sun</i> points towards the Sun.	26
2.3	Example of broadband filter transmission factors as a function of wavelength.	28
2.4	Illustration showing the Earth’s rotational effect on the phase angle while observing a single geostationary satellite as viewed from a position above the North Pole, and looking down at the orbital plane. The Sun is located towards the bottom of the page. Adapted from Bédard [7].	29
2.5	Two examples of light curves constructed by Jolley [6] for geostationary satellites, Intelsat 805 and Anik F1.	30
2.6	Instrumental magnitudes of Anik F1 on the night of 4th November 2013. Blue data at three second resolution courtesy of Mr. Mike Earl, and the green data at two minute resolution [6]	31
2.7	Results produced by Bédard, showing the spectral response of four different solar cells at the same observational geometry [7].	33
2.8	Conceptual illustration of the optical elements required for active polarimetry. Adapted from Goldstein [40].	35
2.9	Illustration of phase angle in an active polarimetry system.	36
2.10	A plan view of the experiment conducted by Culp <i>et al.</i> [8], showing the general layout as provided by the authors.	39
2.11	Example of the results obtained by Culp <i>et al.</i> for an Aluminum sample [8].	41
3.1	A conceptual representation of the experimental layout.	45
3.2	A photograph of the experiment with the light suppression boards removed.	46
3.3	Light system components.	47
3.4	The two rotary stages of the goniometer with the 6061-T6 sample mounted in the sample holder. The black tape seen on the lower portion of the sample suppresses light being reflected from the sample holder onto the surface of the sample. Note the analyzer rotary stage mounted on the post, aligned vertically with the sample.	48
3.5	Linear polariser transmission performance, supplied by Thorlabs.	49
3.6	Analyzer rotary stage with analyzer polaroid mounted. Note, the rotary stage has rotated the optical axis of the polariser to the 90° position.	50

3.7	Experiment samples	53
3.8	Data acquisition flow	55
3.9	Example of a raw data image showing the Azur TJPV cell, at $\theta_i = 45^\circ$. Note the dust spots and the rings within the disk, assumed to be artefacts of the lens.	56
3.10	Master dark image.	57
3.11	Master flat production process. This process is completed for each of the four analyzer orientations. The master bias and master dark images are external inputs.	58
3.12	Example of a master flat sub-section image of the same size seen in Figure 3.17 at the specular observation angle, with $\theta_i=45^\circ$. This image has been produced with a high contrast color map to show the circular features of Figure 3.17 that can be removed by utilizing a master flat reduction. Note the dust object in the lower left hand corner corresponding to the same in Figure 3.17.	59
3.13	A graphical definition of the coordinate system used for the experiment.	60
3.14	Plan view illustration of the experiment showing the angles of illumination and observation	61
3.15	An illustration of the experiment showing the effect of the physical laboratory boundaries on the experiment, specifically on the illumination angles used.	61
3.16	The data image reduction process.	63
3.17	Analysis area of the Azur TJPV seen in Figure 3.9. This area is 192 x 232 pixels in size. The same dust feature and large circular patterns can be seen as in Figure 3.9.	64
3.18	Example of the analysis area selection assessment and feedback. The red and blue rectangles are the areas used to produce the histograms in Figure 3.18(a).	66
4.1	Spectralon DOLP, AOP and total intensity as a function of observation angle (θ_{obs}).	69
4.2	DOLP and AOP as a function of incident light angle (θ_i), compared to the total intensity (I). The DOLP and AOP values are presented as solid lines, and the I values are the broken lines.	70
4.3	DOLP, AOP and total intensity (I) of the Spectralon sample as a function of incident light angle (θ_i) and observation angle (θ_{obs}).	72
4.4	DOLP for Spectralon calculated from the experiment and an empirical model.	75

4.5	DOLP with error bars set at 1σ for 10 individual DOLP calculations. The raw data images were taken at a variety of times of the day and after varying times of source light and CCD operation. . .	77
4.6	Example integration times for all samples. Sub-figure 4.6(a) illustrates all observation locations at $\theta_i = 45^\circ$, and Sub-figure 4.6(b) illustrates the measurements at the specular direction for all θ_i . . .	80
4.7	DOLP and AOP for each material as a function of incident light angle (θ_i), calculated at the specular reflection direction.	82
4.8	DOLP v total intensity at the specular observation direction for the 6061T6 aluminium and white panel. The solid lines provide the values of the sample, and the broken lines for the Spectralon. . .	83
4.9	DOLP v total intensity at the specular observation direction for the Emcore and Azur TJPV cells.	84
4.10	DOLP, AOP and total intensity (I) of the aluminum sample as a function of incident light angle (θ_i) and observation angle (θ_{obs}). . .	86
4.11	DOLP, AOP and total intensity (I) of the white-painted panel sample as a function of incident light angle (θ_i) and observation angle (θ_{obs}).	88
4.12	DOLP, AOP and total intensity (I) of the Emcore TJPV cell sample as a function of incident light angle (θ_i) and observation angle (θ_{obs}).	90
4.13	DOLP, AOP and total intensity (I) of the Azur sample as a function of incident light angle (θ_i) and observation angle (θ_{obs}).	92
5.1	The total time required to acquire all data images necessary to produce one set of reduced Stokes vector calculations for the $\theta_i = 45^\circ$ illumination geometry.	96
5.2	Duty cycle of the analyzer with respect to the total data acquisition time period for the white painted panel at the $\theta_i = 45^\circ$ illumination geometry.	97
B.1	Description of the 16 individual illumination/detected polarisation characteristic pairs used in a full Lu-Chipman Muller matrix decomposition. Adapted from Pasqual <i>et al.</i> [11].	111
C.1	6061T6 DOLP with respect to θ_{obs} and θ_i	113
C.2	6061T6 AOP with respect to θ_{obs} and θ_i	114
C.3	White painted panel DOLP with respect to θ_{obs} and θ_i	116
C.4	White painted panel AOP with respect to θ_{obs} and θ_i	117
C.5	Emcore TJPC cell DOLP with respect to θ_{obs} and θ_i	119

C.6 Emcore TJPV cell AOP with respect to θ_{obs} and θ_i 120
C.7 Azur TJPC cell DOLP with respect to θ_{obs} and θ_i 122
C.8 Azur TJPV cell AOP with respect to θ_{obs} and θ_i 123

List of Acronyms

ADU	- Analogue to Digital Unit
AOP	- Angle of Linear Polarisation
BRDF	- Bi-directional Reflectance Distribution Function
CCD	- Charge Coupled Device
DOLP	- Degree of Linear Polarisation
IAU	- International Astronomical Union
NSP	- Normalized Stokes Parameters
RAAF	- Royal Australian Air Force
RMCC	- Royal Military College of Canada
RSO	- Resident Space Object
SAT	- Small Aperture Telescope(s)
SED	- Spectral Energy Distribution
SSA	- Space Situational Awareness
SSRL	- Space Surveillance Research Laboratory
TJPV	- Triple Junction Photo-Voltaic cell

1 Introduction

1.1 Background

Since the beginning of the space race in 1957 with the launch of Sputnik 1, human endeavors to exploit and explore have resulted in a once-pristine near-Earth space environment becoming heavily populated. Presently, there are over 15,000 man-made objects greater than 10cm being continuously tracked, and there are estimates of 500,000 smaller objects also being in orbit [1]. The task of protecting and managing our near-Earth space environment for future use in light of this large population of resident space objects (RSOs), particularly from events of exponential collision growth, called the *Kessler Effect* [2] is extremely important, and only increases as the population grows. Our understanding of where these objects are located, their origin, composition, size, mass and numerous other characteristics is one of the tasks of Space Situational Awareness (SSA), an effort that is internationally recognized by industry, governments and militaries as urgent. By collecting this information, modeling and estimates of object decay, origin and size can be obtained. Information like this can then be used to assist with spacecraft and orbit design, object avoidance and even health monitoring of operational spacecraft amongst numerous other methods of space environment management. As a result, advances in methods and technologies to enhance the SSA mission are constantly being investigated.

One such broad method that has shown a level of promise in helping to achieve the wider SSA mission is that of collecting and analyzing the light reflected from RSOs in order to infer specific RSO characteristics [3–5]. Photometric analysis, including broadband photometry [6] and spectroscopy [7] using small aperture telescopes is an avenue of investigation currently being undertaken at the Royal Military College of Canada (RMCC). Another kind of photometric analysis that provides promise for SSA advancement is the study of the polarimetric characteristics of RSO reflections. Much work has

been done into various methods of polarimetric investigation [8–11]; however the utility of applying polarisation characterization to the practical problem of SSA is far from being fully investigated and confirmed.

1.2 Fundamentals of Polarimetry

This section presents the fundamental characteristics of the nature of light, viewed in the classical context as a transverse electromagnetic wave. An explanation of light polarisation is provided and the *Stokes parameters* are introduced as a way of quantifying and representing the characteristics of polarisation.

1.2.1 The nature of light

Begin with Maxwell's equations in free space in differential form:

$$\nabla \cdot \mathbf{E} = 0 \quad (1.1)$$

$$\nabla \times \mathbf{E} = -\frac{\partial \mathbf{B}}{\partial t} \quad (1.2)$$

$$\nabla \cdot \mathbf{B} = 0 \quad (1.3)$$

$$\nabla \times \mathbf{B} = \mu_0 \epsilon_0 \frac{\partial \mathbf{E}}{\partial t} \quad (1.4)$$

where μ_0 and ϵ_0 is the permeability and permittivity of free space respectively. Taking the curl of Equation 1.2 to isolate \mathbf{E} and similarly for Equation 1.4 for \mathbf{B} gives:

$$\begin{aligned} \nabla \times (\nabla \times \mathbf{E}) &= -\frac{\partial}{\partial t} \nabla \times \mathbf{B} \\ &= -\mu_0 \epsilon_0 \frac{\partial^2 \mathbf{E}}{\partial t^2} \end{aligned} \quad (1.5)$$

$$\begin{aligned} \nabla \times (\nabla \times \mathbf{B}) &= \mu_0 \epsilon_0 \frac{\partial}{\partial t} \nabla \times \mathbf{E} \\ &= \mu_0 \epsilon_0 \frac{\partial^2 \mathbf{B}}{\partial t^2} \end{aligned} \quad (1.6)$$

Utilizing the vector identity:

$$\nabla \times (\nabla \times F) = \nabla(\nabla \cdot F) - \nabla^2 F \quad (1.7)$$

where $\nabla^2 F$ provides the vector Laplacian of the vector field F , and the simplification:

$$c_0 = \frac{1}{\sqrt{\mu_0 \epsilon_0}} \quad (1.8)$$

Equations 1.5 and 1.6 simplify to:

$$\frac{\partial^2 \mathbf{E}}{\partial t^2} - c_0^2 \cdot \nabla^2 \mathbf{E} = 0 \quad (1.9)$$

$$\frac{\partial^2 \mathbf{B}}{\partial t^2} - c_0^2 \cdot \nabla^2 \mathbf{B} = 0 \quad (1.10)$$

which are transverse wave equations for the electric (\mathbf{E}) and magnetic (\mathbf{B}) fields in free space with a phase velocity of the speed of light in a vacuum (c_0).

By considering only the electric field component of the radiation (as the movement of electric charges resulting from the applied influence of the electric field is readily measurable as a current), a sinusoidal waveform traveling in the $+Z$ direction with a speed c provides a general solution to the electric field wave equation. Shurcliff[12] notes that the magnitudes of the electric and magnetic wave components of the radiation are proportional, therefore understanding the behavior of one allows an understanding of both, with the concentration on the electric component being an artefact of convention.

The electric field wave (\mathbf{E}), assumed without loss of generality to be propagating in the $+Z$ direction, can be constructed from orthogonal components (\mathbf{E}_x and \mathbf{E}_y) using harmonic waveform expressions which are general solutions to the electric field wave equations as:

$$\mathbf{E}_x = E_x \cos(kz - \omega t) \quad (1.11)$$

$$\mathbf{E}_y = E_y \cos(kz - \omega t + \xi) \quad (1.12)$$

where:

$$\mathbf{E} = \mathbf{E}_x + \mathbf{E}_y \quad (1.13)$$

E_x and E_y are the amplitudes of the wave components, ξ represents the phase difference between the two components, k is the wave number, ω is the angular frequency and t is time. The addition of these component waves to produce \mathbf{E}

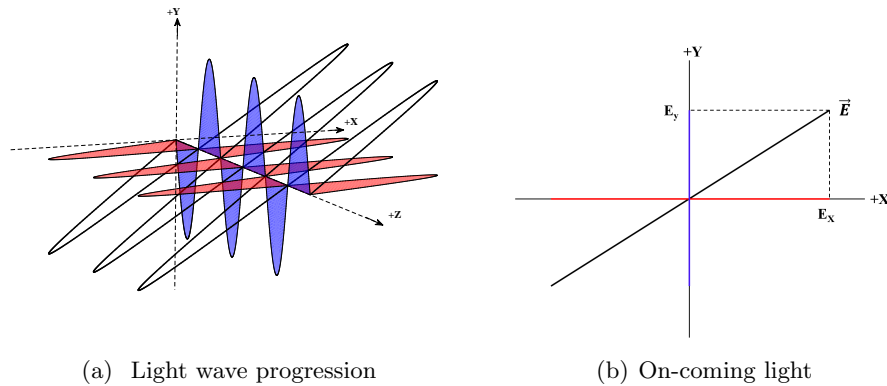


Figure 1.1: A conceptual illustration of the total \mathbf{E} wave (black) as a combination of two orthogonal waves. Note, the component X and Y waves are in phase.

is illustrated in Figure 1.1(a). The same situation can be observed by looking towards the oncoming light wave from a position located on the $+Z$ axis. Figure 1.1(b) illustrates the result.

In the general case of nonzero \mathbf{E}_x , \mathbf{E}_y and ξ , and provided there is no long-term coherency between the component of the light[12–15], the tip of the electric field vector of the propagating wave sweeps out a helical path in space. This can be seen in Figure 1.2, again by locating a point of view for an observer on the $+Z$ axis and looking in the direction of the origin. A fixed ellipse will be observed.

This wave equation formulation allows for the visualization of two distinct behaviors of the the wave; preferred orientation and direction of rotation. The preferred orientation is a function of the relative amplitudes of the two components \mathbf{E}_x and \mathbf{E}_y , and the rotation by their relative phase given by ξ seen in Equation 1.12. These behaviors are combined to form the ellipse seen in Figure 1.2. This ellipse is called the *polarisation ellipse*, with the preferred orientation and rotation of the electric wave component of the beam of light \mathbf{E} being described as the light's *polarisation*. This concept is illustrated in Figure 1.3.

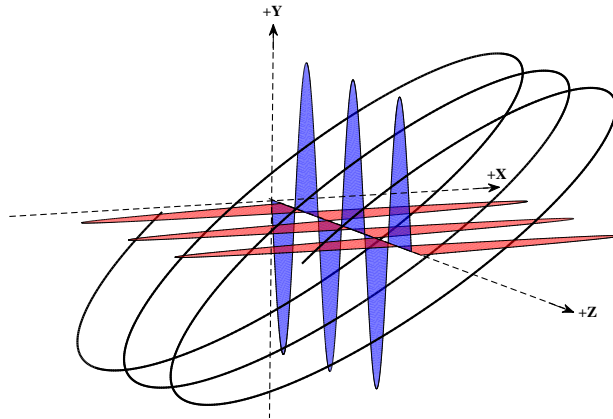


Figure 1.2: An illustration showing the elliptical progression of the tip of the E vector (black) in the $+Z$ direction, as a vector addition of out of phase, orthogonal X (red) and Y (blue) components.

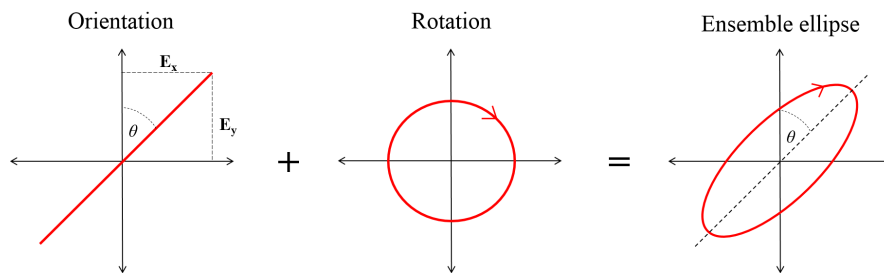


Figure 1.3: Illustration of the combination of ellipse orientation and rotation light components. The axes are component wave amplitudes.

1.2.2 Polarisation special cases

As discussed in Subsection 1.2, light is generally elliptically polarised [12]. This state of polarisation occurs when there is no coherency between the component waves, and the relative phase (ξ) is neither zero nor a whole negative or positive integer multiple of π . This is the case illustrated by Figure 1.2.

Fully polarised light

When $\xi = 0$ or $n\pi$ (where n is an integer), the component light waves will produce an ensemble light wave without a circular component. In this instance the light is referred to as *linearly polarised*. In other words, the general case polarisation ellipse has collapsed to a straight line. The relative magnitudes of the component light waves will still provide orientation information however. This is the case illustrated by Figure 1.1.

A second special case occurs when $\xi = \left(\frac{\pi}{2}\right) \pm n\pi$ and $E_x = E_y$. This set of conditions results in an ensemble wave ellipse that is perfectly circular and has a rotation direction, either left-handed or right-handed.

In both of these special cases, the light can be described as being *totally polarised*.

1.2.3 Unpolarised light

When there is no discernible orientation or rotation direction, then the light is said to be *unpolarised*. The addition of the component waves in this situation will sum to zero as given by;

$$\mathbf{E} = \sum E_x \cos(kz - \omega t)\hat{\mathbf{x}} + E_y \cos(kz - \omega t + \xi)\hat{\mathbf{y}} = 0 \quad (1.14)$$

It should be noted that the light wave still exists and has time dependent progression as the component waves still have an amplitude (E_x and E_y), but no polarisation preference is apparent.

1.2.4 Partially polarised light

Partially polarised light can be viewed as a superposition of correlated and uncorrelated waves resulting in a non-zero net \mathbf{E} . In this case, the ellipse will

have either, or both, a discernible orientation and direction of rotation.

$$\mathbf{E} = \sum E_x \cos(kz - \omega t) \hat{\mathbf{x}} + E_y \cos(kz - \omega t + \xi) \hat{\mathbf{y}} \neq 0 \quad (1.15)$$

This is the situation illustrated in Figures 1.2. The ratio of unpolarised to polarised light is referred to as the *degree of polarisation*.

Clarke [16] provides a general description of the polarisation ellipse in terms of the component wave amplitudes E_x and E_y , and the relative phase difference between these waves (ξ) constructed and adapted from Equations 1.11 and 1.12 as:

$$\frac{|\mathbf{E}_x|^2}{E_x^2} + \frac{|\mathbf{E}_y|^2}{E_y^2} - \frac{2|\mathbf{E}_x||\mathbf{E}_y|\cos\xi}{E_x E_y} = \sin^2 \xi \quad (1.16)$$

1.3 The Stokes Parameters

The polarisation content of a beam of light can be described using the Stokes parameters, named for Sir George Gabriel Stokes who first suggested the method in 1852 [13, 17]. The Stokes parameters represent measures of radiant energy per unit time per unit area, or the flow of radiant energy in specific vibration directions of the electric field of the incident light beam [16, 17].

A more in-depth definition for the Stokes parameters based on that presented by Shurcliff [12] and refreshed by Hecht [13, 14] is found in Appendix A. It provides a description based on the ‘operational use’ of the Stokes parameters and should be referred to for a more thorough description.

The ability of the Stokes parameters to describe the polarisation characteristics of light contrasts favorably with other representations such as Jones parameters which are valid for fully polarised light only [15, 17, 18]. Another advantage of using Stokes parameters for polarimetric SSA investigation at optical wavelengths is that the Stokes parameters are easily able to be retrieved from a series of observations made using a telescope and a charge-coupled device (CCD) camera. An optical element with a polarizing characteristics is used in this process. This optical element, used to test or analyze the polarisation of the incoming light is often referred to as the *analyzer*. The *analyzer* nomenclature is used throughout this work.

There are four Stokes parameters, and they are normally collected into a four-element column vector called the *Stokes Vector*, \vec{S} , given as:

$$\vec{S} = \begin{bmatrix} S_0 \\ S_1 \\ S_2 \\ S_3 \end{bmatrix} \equiv \begin{bmatrix} I \\ M \\ C \\ S \end{bmatrix} \equiv \begin{bmatrix} I \\ Q \\ U \\ V \end{bmatrix} \quad (1.17)$$

with the equivalencies showing some of the different representations of the Stokes Parameters. Walker's form I, Q, U and V will be used throughout [16].

For the purpose of describing the Stokes vector in terms of a quantity that is measurable, definitions for each parameter in terms of the *polarisation ellipse* seen in Figure 1.4 and the intensity of optical measurements are provided. Firstly, the relationship between the amplitudes of the component waves and the intensity measurement provided by the CCD is explained by Clarke [16]. The irradiance (I ; the time averaged transmission of energy per unit area per unit time) of the beam of light is proportional to the square of the amplitude of its electric field (\mathbf{E}) given by:

$$I = \frac{c\epsilon}{2} |\mathbf{E}|^2 \quad (1.18)$$

where c is the speed of light and ϵ is the dielectric constant of the medium the light is passing through. This allows the measurement of the intensity of a beam of light to be related to its amplitude. From the formulation of the nature of light presented, specifically by using Maxwell's equations as opposed to the more precise quantum theory, the measurements required can be time-averaged intensity measurements such as those provided by a CCD.

Definitions for the Stokes parameters are provided by Tinbergen [17] and Berry [19], and assume a perfect analyzer and a metering system free from polarisation bias. They are presented as:

$$\begin{bmatrix} I \\ Q \\ U \\ V \end{bmatrix} = \begin{bmatrix} E^2 \\ E^2 \cos 2\beta \cos 2\chi \\ E^2 \cos 2\beta \sin 2\chi \\ E^2 \sin 2\beta \end{bmatrix} = \begin{bmatrix} I_{total} \\ I_0 - I_{90} \\ I_{45} - I_{135} \\ I_{rh} - I_{lh} \end{bmatrix} \quad (1.19)$$

where χ provides the angle of polarisation, or orientation of the polarisation ellipse, $\tan \beta$ the axial ratio of the ellipse and E is related to the *amplitude of the electric field vibration* [17]. The $I_{subscript}$ values indicate intensities

measured by a light meter like a CCD. The I_{total} is the total intensity, and the I_n values are the intensities with the analyzer positioned in the optical path with its optical axis located at n degrees with respect to an arbitrary axis orthogonal to the direction of progression of the beam of light. The I_{rh} and I_{lh} intensities are measured using a circular polarisation analyzer. The sign conventions for these definitions are shown graphically in Figure 1.4. The ellipse can be further visualized by using Figure 1.2, locating a point of view at the origin and looking in the direction of $+Z$.

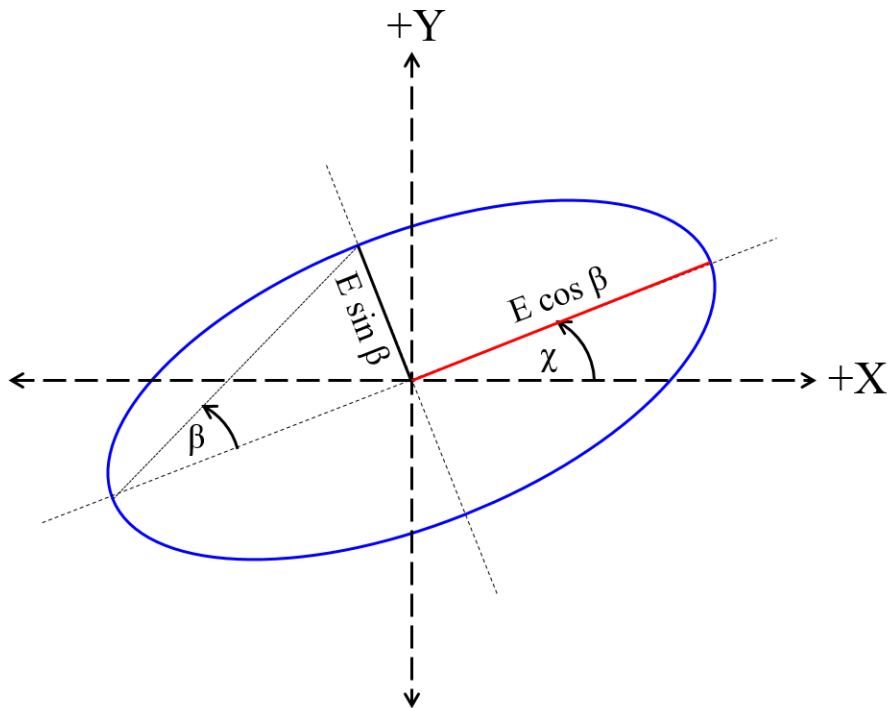


Figure 1.4: A representation of the polarisation ellipse showing the relationships between ellipse angles and electric field magnitudes, developed from Tinbergen [17].

Equation 1.19 allows simple descriptions of each of the Stokes parameters. I provides the total intensity of the light beam, Q describes the preference of the beam to have a horizontal (positive values) or vertical (negative values) polarisation, U denotes whether the beam has a preference to vibrate in the $45^\circ/225^\circ$ plane (positive values) or in the $135^\circ/315^\circ$ plane (negative

values) and V denotes whether a right-handed propagation (positive values), or left-handed (negative values) circular polarisation exists. These convention explanations are provided by Shurcliff [12] and Tinbergen [17], and are adapted from the conventions provided by the International Astronomical Union (IAU) [20] and are explained graphically in Figure 1.5, noting that the observer is looking *towards* the source and the axes are aligned with the laboratory horizontal and vertical directions. The axes are the magnitudes of the component wave amplitudes.

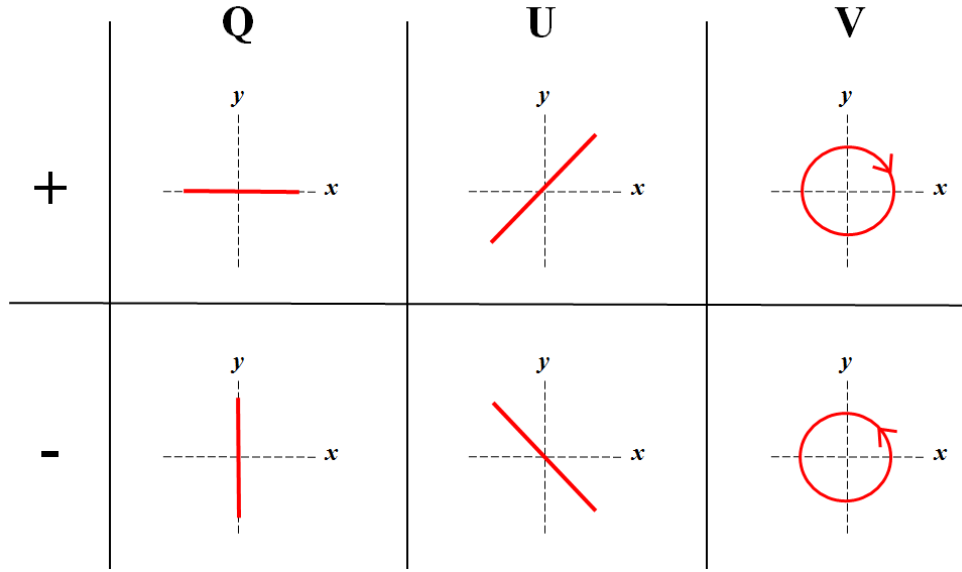


Figure 1.5: Graphical description of the Stokes parameter conventions presented by Shurcliff [12] and Tinbergen [17], and adapted from the IAU convention [20]. In all cases direction of propagation is into the page.

1.4 Polarisation states as Stokes parameters

As seen in Section 1.2.1, light can exist in a state of complete polarisation, partial polarisation, or in a totally unpolarised state. A description of these three states is presented in terms of the Stokes parameters and their measurable intensities. These descriptions will aid the reader in appreciating the experimental portions of this work, including the experimental concept and production of results. Derivations of the degree and angle of polarisation in

terms of the Stokes parameters are presented, concentrating on their linear characteristics. Finally, brief explanations of two pertinent modes of polarisation are provided as is an explanation for general performance measures of polarisers.

1.4.1 Unpolarised/Natural light

From Equations 1.14 and 1.19 it can be seen that if the Q , U and V parameters are zero and the total incident irradiance is I_{total} , or:

$$\vec{S} = \begin{bmatrix} I_{total} \\ 0 \\ 0 \\ 0 \end{bmatrix} \quad (1.20)$$

it can be seen that the only characteristic of the beam of light is its intensity incident on the measuring system. This is characteristic of a completely unpolarised state, and is often referred to as *natural light*. For practical purposes it could be assumed that the undisturbed light provided by the Sun is completely unpolarised [17].

1.4.2 Fully polarised light

Through a similar analysis of the Stokes parameters as seen in Section 1.4.1 it is apparent that if the measured flux for any of the Q , U or V parameters is the same as the I_{total} , then the entire irradiance of the beam of light exists purely in the polarisation state indicated by that Stokes parameter. For example, the relation from Hecht [13, 14]:

$$I_{total} = I_0 + I_{90} \quad (1.21)$$

would indicate that the measured beam of light with a total intensity I_{total} is contained within the orthogonal intensities of I_0 and I_{90} . This relation holds true for the I_{45} and I_{135} , and I_{rh} and I_{lh} intensities as well. A more useful Stokes parameter representation of fully polarised light can be given by:

$$Q^2 + U^2 + V^2 = I^2 \quad (1.22)$$

where it can be seen that the sum of the square of all the Stokes parameters will equal the square of the total flux. It is apparent that when this relation is true, there is no component of the incident light flux that cannot be described by some measure of polarised light. In other words, the incident flux on the

light analyzing system is completely polarised as was predicted in Section 1.2.2 when $\epsilon = 0$ or a whole integer multiple of $\left(\frac{\pi}{2}\right)$ and $E_x = E_y$. The requirement to square the right-hand terms comes from the possibility that the Q , U and V parameters may be negative as seen in Section 1.3. Recalling that the V parameter describes the circular polarisation direction of the polarisation ellipse, the requirement for a light beam to be fully linearly polarised becomes:

$$Q^2 + U^2 = I^2 \quad (1.23)$$

This is the situation illustrated by Figure 1.1.

1.4.3 Partially polarised light

For the case of partially polarised light, the total light wave can be described as consisting of an ensemble of unequal polarised and unpolarised components according to Stokes' *additivity theorem* [16], provided there is no addition of coherent beams; a condition not expected to occur in naturally produced light.

As was briefly discussed in Sections 1.2.4 with Equation 1.15, it would be expected that with partially polarised light an inequality will result when considering the Stokes parameters:

$$Q^2 + U^2 + V^2 < I^2 \quad (1.24)$$

indicating that a portion of the incident light does not contribute to the characteristics of the polarisation ellipse, and can therefore be regarded as unpolarised. Stokes' additivity theorem can then be described as:

$$I_{total} = I_p + I_u \quad (1.25)$$

where I_p is the fully polarised portion of the total light beam I_{total} , and I_u the unpolarised light portion. This aligns with considering polarised light as being an ensemble of polarised and unpolarised waves. Equation 1.25 can then be re-written in terms of measurable intensities and Stokes parameters by substituting Equations 1.22 and 1.14 into Equation 1.25. The result is:

$$\vec{S} = \begin{bmatrix} I \\ Q \\ U \\ V \end{bmatrix} = \begin{bmatrix} I_0 + I_{90} \\ I_0 - I_{90} \\ I_{45} - I_{135} \\ I_{rh} - I_{lh} \end{bmatrix} + \begin{bmatrix} I_{total} - (I_0 + I_{90}) \\ 0 \\ 0 \\ 0 \end{bmatrix} \quad (1.26)$$

It follows that the unpolarised portion of the the light beam will be a subtraction of the polarised intensity from the total intensity, as seen in Equation 1.19. For practical reasons the intensity values measured for each Stokes parameter are normalized by the I_{total} parameter resulting in the Normalized Stokes Parameters (NSP), given by:

$$\vec{S}_n = \begin{bmatrix} \frac{I_{total}}{I_{total}} \\ \frac{I_{total}}{I_0 - I_{90}} \\ \frac{I_{total}}{I_{45} - I_{135}} \\ \frac{I_{total}}{I_{rh} - I_{lh}} \\ \frac{I_{total}}{I_{total}} \end{bmatrix} = \begin{bmatrix} 1 \\ q \\ u \\ v \end{bmatrix} \quad (1.27)$$

which are shown constructed from their constituent intensity measurements. This form illustrates a core relation for this work, noting that the v Stokes parameter is not obtained in a linear analysis.

1.4.4 Degree and angle of polarisation

Hecht [13] provides a relation to determine the fraction of polarised light (P) to unpolarised light intensity using the measurable polarised irradiance I_p and unpolarised irradiance I_u from Equation 1.25:

$$P = \frac{I_p}{I_p + I_u} \quad (1.28)$$

This can be given in terms of the NSP [17] for a partially polarised beam as:

$$P = \sqrt{q^2 + u^2 + v^2} \quad (1.29)$$

When considering the linear components of the polarisation ellipse (that is, the q and u parameters only), the degree of linear polarisation (DOLP) can be obtained using:

$$DOLP = \sqrt{q^2 + u^2} \quad (1.30)$$

While understanding the direction of the circularly polarised component of the polarisation ellipse would give the most thorough appreciation of the polarisation characteristics, the linear parameters described by q and u provide enough information to differentiate between states of polarisation for the purposes of this investigation. As such, the use of DOLP throughout this work is the basis for comparative measures of polarisation.

In addition to the degree of polarisation determination, the orientation of the major axis of the polarisation ellipse as seen in Figure 1.4, given as χ , is the *angle of polarisation*. This quantity has also been variously referred to in literature as the *position angle* (ϕ) [21] and the *direction of vibration* (ξ) [16]. As such, it will be referred to as *AOP* for the remainder of this work. It should not be confused with the similar *polarisation angle* or Brewster's angle which will be described in Section 1.4.5.

The AOP gives insight into the orientation of the axis of the polarisation ellipse. Consider a polarisation state where the light is fully linearly polarised in the horizontal axis. In this case the angle of polarisation would be 0° , and similarly if it was fully polarised in the vertical axis, the angle of polarisation would be 90° . If the light contains a polarisation tendency outside these directions while not being circularly polarised, then the angle subtended by the horizontal axis and the major axis of the polarisation ellipse becomes the AOP.

Recalling the definitions of the q and u parameters from Equation 1.19, an expression for AOP can be arrived at. Firstly:

$$Q = E^2 \cos 2\beta \cos 2\chi \quad (1.31)$$

$$U = E^2 \cos 2\beta \sin 2\chi \quad (1.32)$$

which can be rearranged and simplified to:

$$\frac{U}{Q} = \frac{\sin 2\chi}{\cos 2\chi} \quad (1.33)$$

and:

$$\tan(2\chi) = \frac{U}{Q} \quad (1.34)$$

Correcting for AOP nomenclature and NSPs gives:

$$AOP = \frac{1}{2} \tan^{-1} \left(\frac{u}{q} \right) \quad (1.35)$$

which serves as the final form for the calculation of AOP from the Stokes parameters [12, 13, 17].

Equations 1.30 and 1.35 allow an almost complete reconstruction of the polarisation ellipse by directly measuring reflected light intensities through a

linear analyzer, with the last missing piece of information being the ‘handedness’ of the ellipse. They are the basic equations used in the presented experiment to perform the required polarimetric operations.

1.4.5 Methods of polarisation

Generally, there are four methods through which light will be polarised upon interaction with a medium; through selective absorption (dichroism), upon reflection or scattering, and through birefringence [15]. As this work deals primarily with light reflected from samples and by extension that reflected from RSOs, only reflection will be explained in detail. Notwithstanding, short descriptions of dichroism, scattering and birefringence are provided.

A brief introduction to the performance measures of a dichroic polariser and Malus’ Law is also presented.

Reflection

The reflection mode of polarisation, as it applies to this work, is presented conceptually in Figure 1.6. The Sun provides the illumination, the RSO the object the polarising element, and then a telescope to collect the light, an analyser to sample to polarisation of the collected light and the CCD to measure the light.

Étienne Malus studied the effect of reflection polarisation from dielectric materials in 1808 [13, 14, 22]. The resulting work conducted by Young and Fresnel [23] allow a simple understanding of the phenomenon by assuming a transverse wave nature of light and an electron-oscillator model [12] of the surface of the material.

First, considering the plane of incidence illustrated in Figure 1.7 to be that containing the incident beam of unpolarised light and the refracted and reflected beams, it can be seen that the electron oscillators near the surface of the material will radiate in the plane of incidence as a result of the in-plane \vec{E} field of the refracted light. The reflected beam will then contain a trend to polarisation in the direction *perpendicular* to the plane of incidence (and parallel to the surface). At a particular angle of incident light, the angle between the reflected and refracted beams will be 90° at which point the entirety of the in-plane polarisation component will be refracted. This leaves only the perpendicular component to be reflected. This angle θ_B (a function

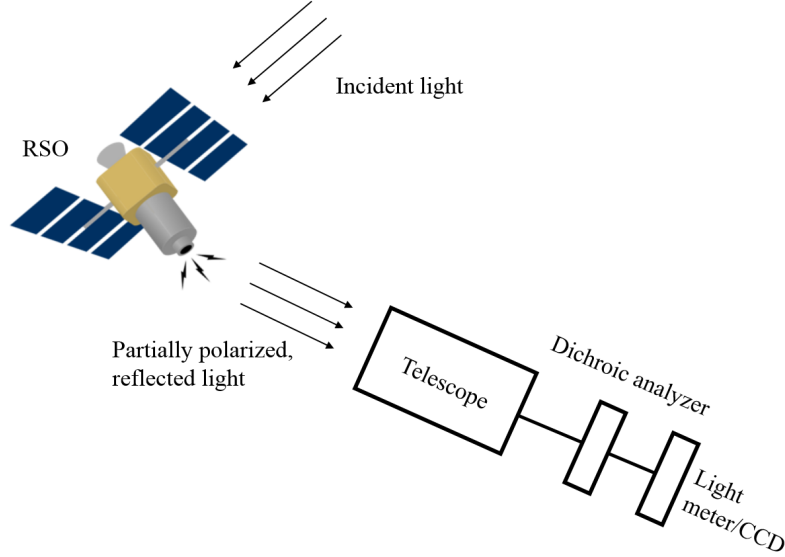


Figure 1.6: Conceptual diagram showing main component considerations for reflection polarisation.

of the refractive indices of the medium the light travels through n_t and the surface it irradiates n_i) is termed ‘Brewster’s Angle’, for Sir David Brewster who first derived it empirically [13, 14]. It is given by:

$$\theta_B = \arctan \left(\frac{n_t}{n_i} \right) \quad (1.36)$$

This is the physical mode through which the RSOs in question are able to produce a level of polarisation upon the reflected light. It should be noted that the description given relies on a dielectric material with the problem becoming more complicated for magnetic, nonconducting materials [12, 15].

By way of example, the light incident upon a simplified generic tripple junction photo-voltaic (TJPV) cell illustrated in Figure 1.8, adapted from Fatemi [24], can be transmitted and reflected from and through numerous layers, each with a different refractive index. A combination of the reflection phenomenon illustrated above can then result in a reflected beam with polarization characteristics different to the incident beam [15].

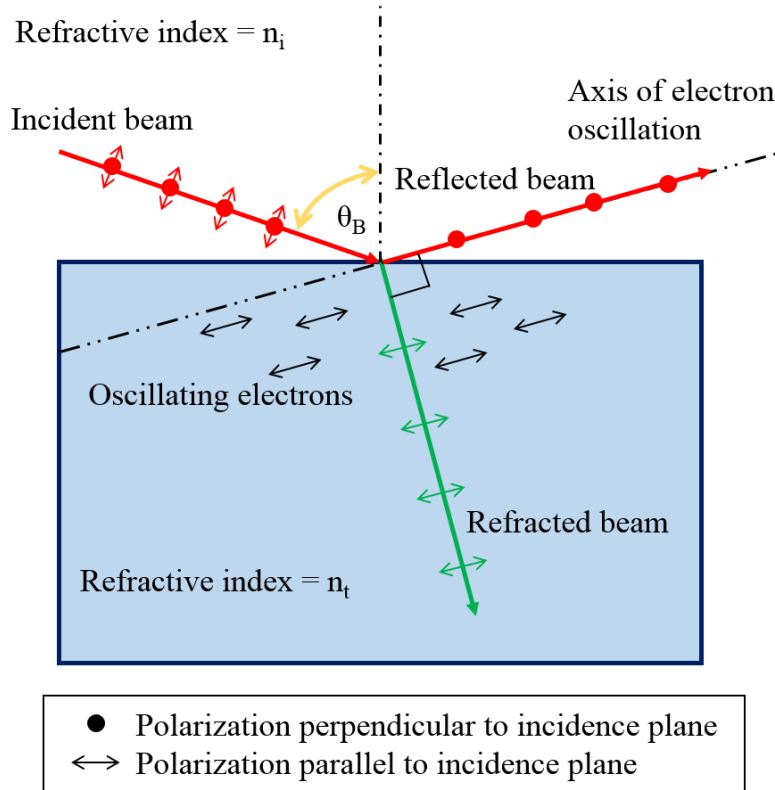


Figure 1.7: An illustration of reflection polarisation phenomenon occurring at Brewster's Angle.

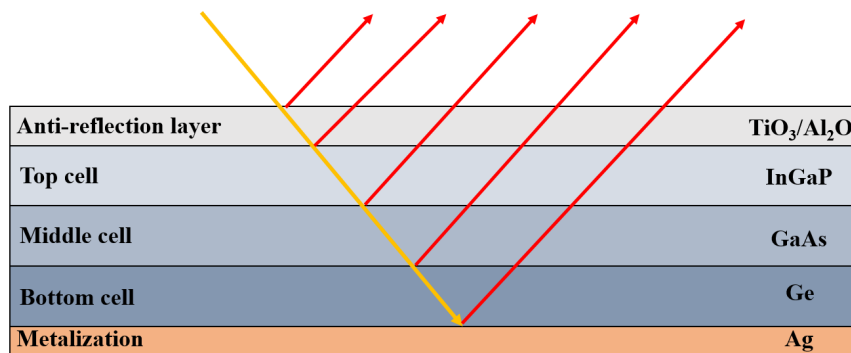


Figure 1.8: A conceptual illustration of a simplified TJPV cell and the multi-layer nature of its reflective properties.

Dichroism

Broadly speaking, dichroism refers to the selective absorption of one of the orthogonal polarisation components of an incident beam. The nature of the dichroic material is anisotropic, being essentially invisible to one orientation of polarised light (called the *fast*, *optical* or *transmission* axis somewhat interchangeably), and opaque to the orthogonal orientation (along the *extinction* axis). There are numerous dichroic materials, ranging from man-made wire grids, crystals and films with the term ‘polaroid’ coming from E.H. Land’s discovery in 1938 of stretched hydrocarbon films that were able to polarise light [25]. He named this film *Polaroid* which became the commercial brand name of the material. Regardless of the type or method of construction however, the basic operating phenomenon is the same.

The wire grid provides a ready example to explain the operation of dichroic polarisers. Figure 1.9 provided by Hecht [14] illustrates a wire grid polariser with the transmission axis established within the horizontal plane of the diagram. It can be seen that the horizontally polarised component of the natural light incident upon the polariser is able to pass through the closely spaced vertical wires, while the vertical portion is absorbed, or blocked. Similarly, if the wire grid polariser’s transmission axis was rotated 90° so that the wire grid was orientated horizontally, then only the vertically polarised component of the light would be able to pass through. While this example uses an obvious wire grid, all dichroic polarisers are essentially acting in the same fashion. In polaroid film, the wires are replaced by stretched hydrocarbon molecules [14]. In a dichroic crystal, the wires are replaced by oscillating molecules.

Birefringence

Simplistically, polarisation through birefringence is as a result of the production of two refracted beams due to two different refraction indices for a single material [15]. Just as a dichroic polariser displays a preferential absorption or transmission for a particular orientation of polarised light, so too does a birefringent material treat the polarised components of an incident light beam anisotropically, that is, in a directionally dependent manner.

The anisotropic treatment of light incident upon a material is a result of anisotropic molecule binding forces [15][14] within that material. As an incident light beam enters the material, the orthogonally polarised components of the light will experience different refractive indices depending on the op-

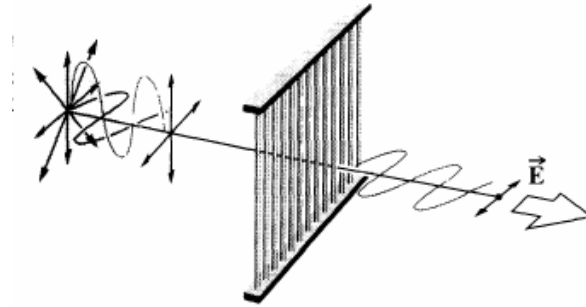


Figure 1.9: Illustration of the operating principle of a dichroic polariser, in this case a wire grid [14].

tical axis of the material. As the light beam progresses the two orthogonal components will begin to diverge. With due regard given to the required path lengths to achieve full component separation, the light beam can exit the material as two distinct, orthogonal linearly polarised beams. Materials of this nature, such as calcite, can be constructed to form prisms that better illustrate the general phenomenon. Figure 1.10, adapted from Hecht [14] and Pedrotti [15] shows a Wollaston prism and the effect it has on an incident beam of unpolarised light. A Wollaston prism is constructed from two portions of birefringent crystal, joined such that their optical axes are perpendicular to each other, and the intended direction of incident light.

Scattering

By appreciating the transverse nature of the light wave, and a linearly polarised light wave in particular, it follows that the direction of vibration of the incident light will be perpendicular to the direction of propagation. Once this light wave impacts a scattering particle, the particle will in turn begin to vibrate in the same direction as the incident light wave vibration. If an observer views the light scattered from the particle at a location perpendicular to the direction of propagation of incident light, the vibration of the particle will be unobservable. If the same thought process is applied with unpolarised incident light however, it can be surmised that the observer at the same perpendicular location will be able to observe a vibration only in a direction normal to the plane of observation [14]. This is illustrated in Figure 1.11.

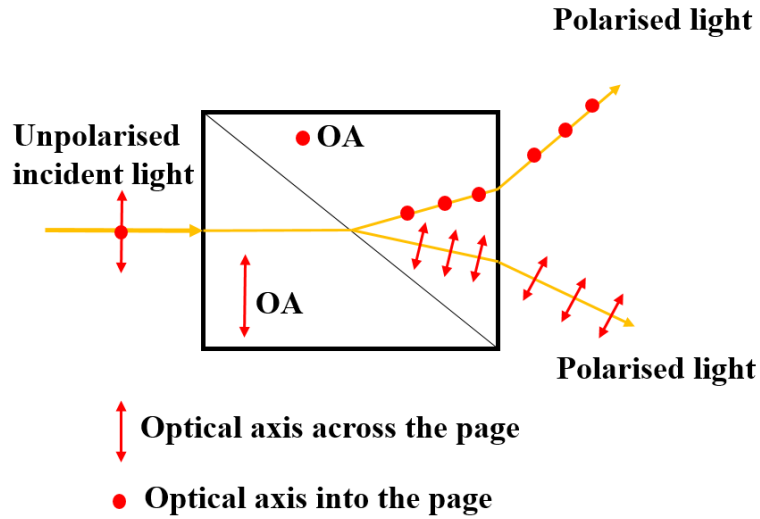


Figure 1.10: Illustration of unpolarised light incident upon birefringent material, in this case a Wollaston prism. Adopted from Hecht [14] and Pedrotti [15].

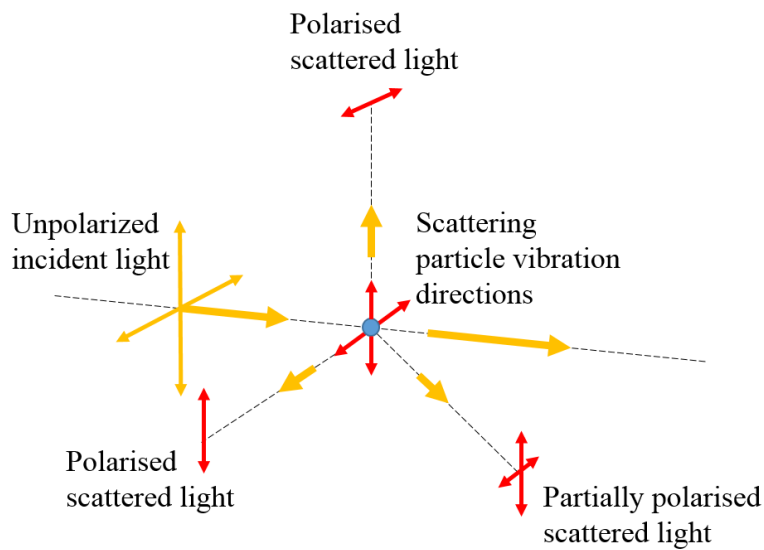


Figure 1.11: Illustration of polarisation induced by scattering. Adopted from Hecht [14].

Polariser performance

The performance of dichroic polarisers is generally provided as a wavelength-dependent transmission factor $T(\lambda)$ of the incident light component with a polarisation aligned with the fast axis of the polariser. This can be expressed as:

$$T(\lambda) = \frac{I_{out}(\lambda)}{I_{in}(\lambda)} \quad (1.37)$$

The extinction ratio (ER) is defined by the transmittance (t_1) of polarised incident light aligned with the fast axis of the polariser to the transmittance of the incident light orthogonal to the polariser's fast axis (t_2) expressed as:

$$ER = 10 \log \left(\frac{t_2}{t_1} \right) \quad (1.38)$$

Of use, Malus' Law provides a relation for describing the intensity of linearly polarised light transmitted through a perfect polariser with a fast axis at an angle θ to the orientation of the incident light (I_0) as:

$$I(\theta) = I_0 \cos^2 \theta \quad (1.39)$$

As polarisers are generally not perfect and therefore an extinction ratio will almost always exist, Malus' law will similarly begin to diverge as θ approaches 90° .

1.5 Aim of the research project

The primary aim of this thesis was to advance the use of visible-wavelength reflectance polarimetry in the space surveillance mission by utilizing CCD observation techniques to determine the polarisation characteristics of a sampling of materials used in the construction of spacecraft. By determining the instrumental polarisation characteristics of the materials over a range of illumination and observation angles, the benefits of further research into this field could be suggested. A complimentary aim was to suggest design parameters for a polarimeter built to operate with the telescopes and CCDs used by RMCC in support of optical SSA research.

To achieve these aims, an experiment was designed to mimic where possible the data acquisition and data reduction processes that would be employed

with CCDs and small aperture telescopes to ensure its applicability to follow-on research efforts within RMCC's Space Surveillance Research Laboratory (SSRL).

1.6 Thesis outline

A review of previous work into both CCD broadband photometry and polarimetry, focusing on artificial satellites and their techniques and results will be presented in Chapter 2. Chapter 3 describes a laboratory experiment conducted to verify and confirm the basis of polarimetric analysis of artificial satellite materials. Specifically, the experiment will determine whether satellite material samples provide differential polarisation characteristics with regard to the observational geometry, sample and a standard surface. Chapter 4 presents typical results of the experiment, while Chapter 5 will discuss these results with reference to the thesis aims. Chapter 6 provides a summary of the conclusions made throughout the work, and makes recommendations for further avenues of investigation. Appendix C contains the complete set of results produced.

2 Literature survey

This literature survey aims to provide an overview of the use of photometry for the characterization of RSOs as applied to the SSA mission. In order to understand the benefits of polarimetric methods, a review of the advantages of broadband photometry, or color photometry and spectro-photometry is useful for contextual background. Firstly, a description of reflectance will be presented as will the notion of *phase angle*, both used to explain the observer-RSO-Sun geometry and its impact on photometric observations. A review of these concepts will be pertinent to the understanding of the literature and will be critical to understanding further chapters of this work. This chapter presents the background to the basics of the reflectance of RSOs, primarily to understand the challenges of optical observation. The state of active polarimetry will be presented, including an explanation of Mueller calculus, a method of material polarimetric modeling and optical element characterization. Lastly, the work done in passive polarimetric characterization of RSO materials will be presented.

2.1 Fundamentals of reflectance

In order to study the polarisation characteristics of artificial RSOs, it is necessary to first understand the dependent factors involved in the reflectance of light from these objects. This is distinct from the explanation of reflection polarisation seen in Section 1.4.5. The importance of this distinction can be appreciated by considering the I Stokes parameter, the definition for which was presented in Section 1.3. As I can correspond to the intensity of signal detected and analyzed by an optical telescope and CCD camera in any photometric RSO observation campaign, understanding the geometry of RSO observations is also required for polarimetric investigations.

A large body of work investigating the reflectance of RSO's already ex-

ists. Bédard [7] and Jolley [6] provide excellent theoretical, experimental and practical examples.

The bi-directional reflectance distribution function (BRDF) is defined by Nicodemus *et al.* [26] as the ratio of reflected irradiance to incident radiance on a surface within a unit steradian, with spatial dependency on the incident and reflectance directions. Nicodemus *et al.* also provide an alternative description; that the BRDF of an object is the measure of reflectance of that object with a directional dependency. The partial form for the BRDF (f_r) is given by Nicodemus as:

$$f_r(\theta_i, \phi_i; \theta_r, \phi_r) \equiv \frac{dL_r(\theta_i, \phi_i; \theta_r, \phi_r; E_i)}{[L_i(\theta_i, \phi_i) \cdot \cos \theta_i d\omega_i]} \quad (2.1)$$

where the θ and ϕ angles are defined graphically in Figure 2.1, E_i provides the incident flux, L_i the reflected flux and ω_i and ω_r providing the unit steradian solid angles of the incident and reflection fluxes respectively. Bédard [7] provides a similar description, with further derivation introducing a wavelength dependency. Of note, Pont *et al.* [27] provide a three dimensional description of the same geometric construction based upon opaque materials with a smooth micro-scale and rough macro-scale surfaces [27]. By modeling the situation they are able reach similar conclusions; that is, there is a spectral influence upon reflection that is sensitive to both the illumination and observation geometry. Pont *et al.* and Bhandari *et al.* [28] similarly extend this conclusion to the polarimetric characteristics of the reflected flux as well.

In any event, this thesis does not intend to present a thorough revision of the reflectance and observation work previously completed. It is worth noting though, that the bi-directional reflectance distribution function (BRDF) will be a factor in achieving accurate polarimetric observations of RSOs.

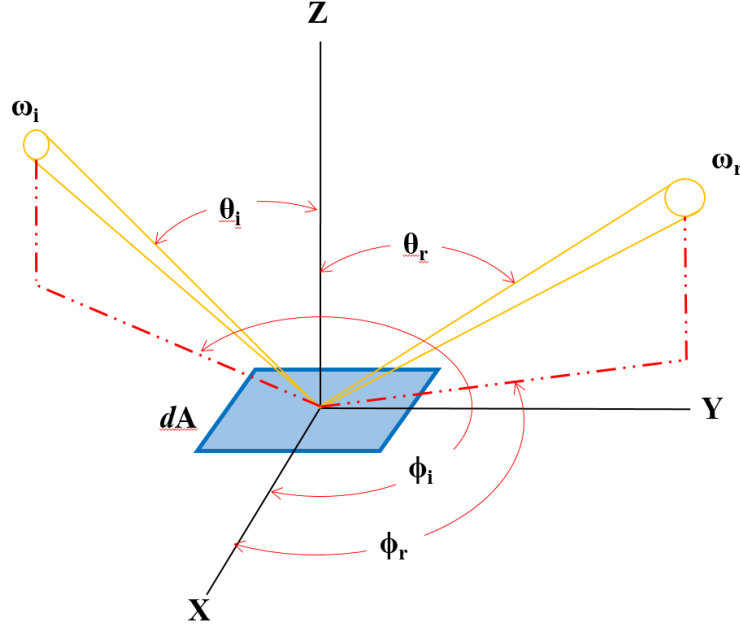


Figure 2.1: Graphical description of bi-directional reflection distribution function, adapted from Nicodemus [26]

2.2 Phase angle

As was seen in Section 2.1, an object's BRDF is dependent on the illumination-object-observer geometry. This illumination-object-observer geometry when viewed in the passive, optical observation of artificial Earth-orbiting satellite context becomes the Sun-satellite-observer geometry. This geometry is often referred to by the term *phase angle*, hereafter represented by α . Kervin *et al.* [29] provide definitions of α that allow it to be related to the the angles introduced in Figure 2.1. Figure 2.2, developed from Nicodemus [26], Bédard [7] and Jolley [6] provides a graphical representation of the constituent angles of this geometry given in the satellite body reference coordinate system. It can be seen by inspection that the angles θ_{obs} , ϕ_{obs} , θ_{Sun} and ϕ_{Sun} describe the same values as represented by θ_i , ϕ_i , θ_r and ϕ_r respectively from Figure 2.1.

With this geometric equality, Kervin *et al.* [29] provide a mathematical description of α that will be used throughout this work. Firstly, vectors originating at the RSO and pointing at the Sun ($\hat{n}_{Sun}(t)$) and the observer ($\hat{n}_{obs}(t)$)

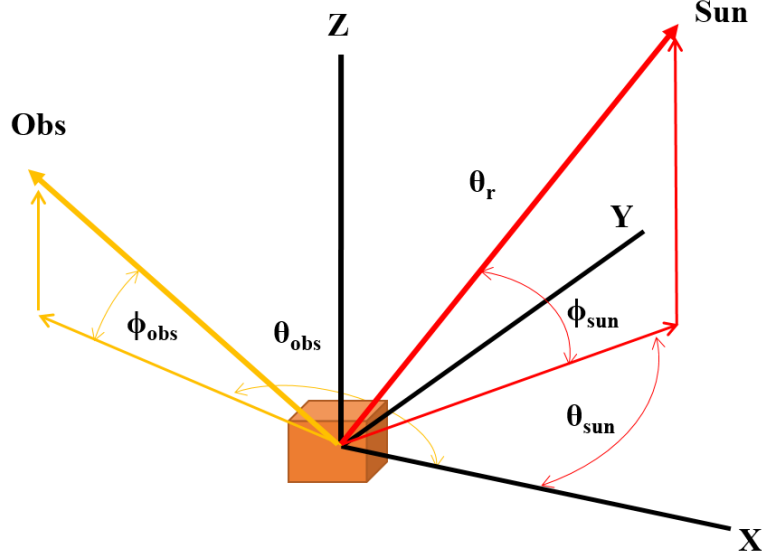


Figure 2.2: Constituent angles of Sun-satellite-observer geometry in the satellite body reference coordinate system as illustrated by Jolley [6, 29]. *Obs* points towards the observer, and *Sun* points towards the Sun.

are given as:

$$\begin{aligned}
 \hat{n}_{Sun}(t) &= [\cos \theta_{Sun}(t) \cos \phi_{Sun}(t)]\hat{\mathbf{X}} + [\sin \theta_{Sun}(t) \cos \phi_{Sun}(t)]\hat{\mathbf{Y}} + \\
 &[\sin \phi_{Sun}(t)]\hat{\mathbf{Z}} \\
 \hat{n}_{obs}(t) &= [\cos \theta_{obs}(t) \cos \phi_{obs}(t)]\hat{\mathbf{X}} + [\sin \theta_{obs}(t) \cos \phi_{obs}(t)]\hat{\mathbf{Y}} + \\
 &[\sin \phi_{obs}(t)]\hat{\mathbf{Z}}
 \end{aligned} \tag{2.2}$$

where the t relation describes the dependency of the observation geometry on the time-dependent relative positions of the Sun and the Earth-located observer. In the laboratory environment the location of the illumination and observer can be fixed and therefore do not necessarily have a time dependency. This allows the time dependent nature of α to be disregarded in the experimental definition. The final definition then becomes the angle between the observation and Sun unit vectors (\hat{n}_{obs} and \hat{n}_{Sun}) provided by the arc-cosine of the dot product:

$$\alpha = \arccos[\hat{n}_S \cdot \hat{n}_{obs}] \tag{2.3}$$

As Kervin *et al.* point out however, using α to describe RSO observations is often done as no precise knowledge of the RSO attitude is available. For this work the precise attitude of the RSO (the test sample or object) is known and can be related to the instrumental coordinate reference frame. This allows the laboratory experiment geometry to be described in terms of the two constituent illumination (Sun) angles, and the two observer (sensor) angles.

The use of the term *phase angle* then becomes somewhat obsolete for this work, except perhaps for relating the experiment to the practical RSO observation problem, or other studies where the term is used in place of more accurate angular descriptions.

2.3 Photometry

Photometry as a science deals with the measurement of photon flux [23]. In the RSO characterization and SSA context, photometry can generally apply to those techniques used to observe an RSO, ordinarily using a telescope/CCD pairing, with the detected light signals being analyzed for spacecraft characterizing features. The ability to differentiate between closely spaced satellites and to suggest individual satellite characteristics such as health, probable mission and surface characteristics are some of the contributions photometry is able to make [6]. General descriptions of the sub-techniques within the science of photometry can be given as broadband photometry, spectrophotometry and polarimetry.

2.3.1 Broadband photometry

Typically, the use of wavelength isolating transmission filters used to investigate specific regions of the incident light frequency spectrum is called broadband photometry. An example of the transmission profile for four such filters is provided at Figure 2.3 and shows the Johnson/Bessel [30] BVRI filter transmission responses as a function of wavelength. They are called the *blue*, *visual*, *red* and *infrared* filters for the areas of the spectrum in which they transmit or isolate.

A significant amount of research into broadband photometry has been conducted, with potential being shown to discriminate between closely-spaced satellites [31, 32], to suggest surface composition of orbital debris [33] and even to delineate the bus type of a satellite [34] amongst many other advances.

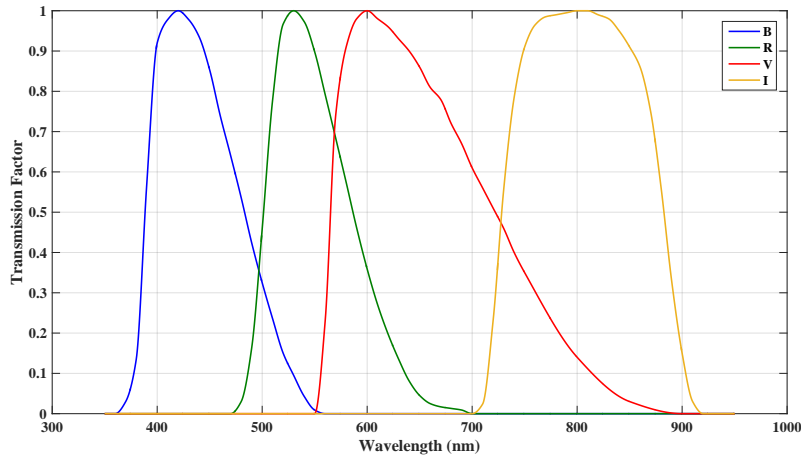


Figure 2.3: Example of broadband filter transmission factors as a function of wavelength.

Cowardin also investigated the use of forming ratios of the different color responses [33]. This was built upon by Bédard [7] by plotting the time resolved color ratios with respect to the reflection geometry. He suggests that a level of surface material identification can be performed based on a catalogue of color ratios of common spacecraft materials.

2.3.2 Light curves

The data acquired from broadband photometry investigations is ordinarily plotted with respect to the time it was acquired. By doing so, the different color responses of the target object can be compared to each other as α changes. The changes in α over a single night of observations can be explained by considering the phase angle of a geostationary satellite. Figure 2.4 illustrates the changes in α for four different observations taken at times t_1 to t_4 from the same location. While the situation is complicated by factors such as satellite design, atmospheric effects and season, the impact on the phase angle can be appreciated.

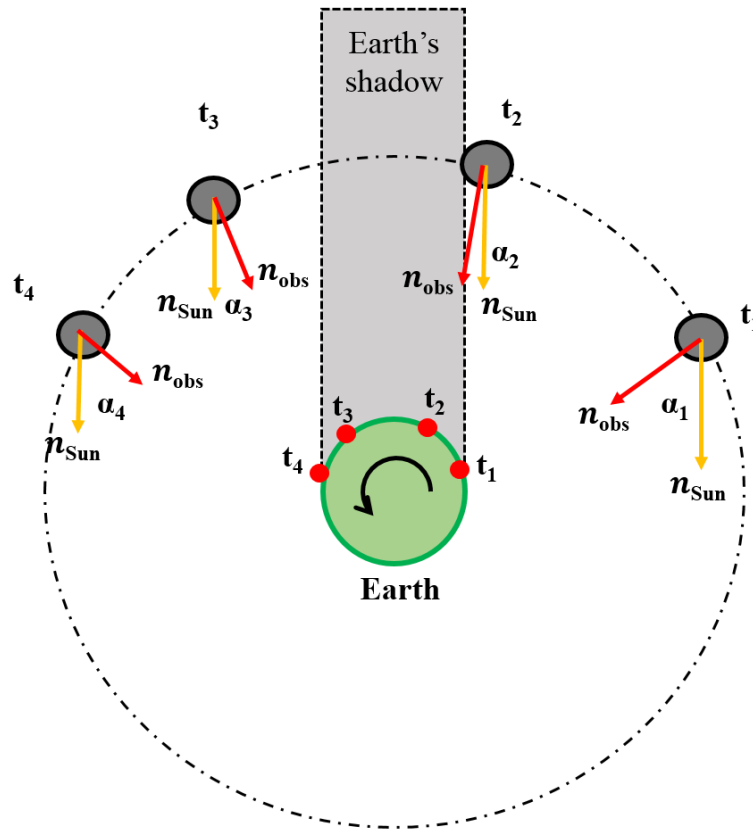


Figure 2.4: Illustration showing the Earth's rotational effect on the phase angle while observing a single geostationary satellite as viewed from a position above the North Pole, and looking down at the orbital plane. The Sun is located towards the bottom of the page. Adapted from Bédard [7].

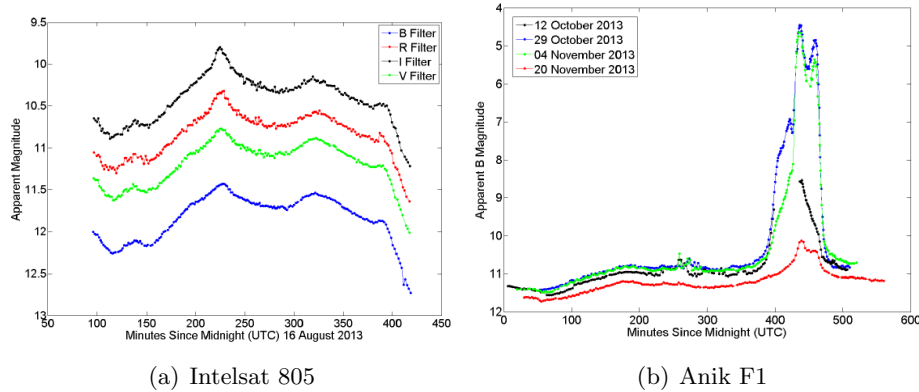


Figure 2.5: Two examples of light curves constructed by Jolley [6] for geostationary satellites, Intelsat 805 and Anik F1.

As the magnitude of the phase angle changes over a single night’s observations, it is normal to plot data results against a time. This type of plot is called a *light curve* and shows the apparent magnitude of the satellite with respect to time. Two examples of this nature are provided by Jolley [6] seen in Figure 2.5. Figure 2.5(a) shows the different color light curves over one night of observations, while Figure 2.5(b) shows the impact of the changing season to the light curve produced from the total flux.

These plots show the changing nature of the the broadband photometric light curves with respect to time (and hence phase angle). It can be appreciated that as different surfaces of the RSO are illuminated, the light curves produced for the different colors may exhibit different features. While specific analysis of light curves is beyond the scope of this work, it should be noted that there is a dependency on the observation and illumination geometry of the RSO being observed. It follows that analysis of these light curves may provide characterizing information about the RSO.

Additional challenges are still present with this technique however. An example given is by Jolley [6] who notes that observations of higher temporal resolution can reveal RSO reflection signal features previously undiscovered [6]. Figure 2.6 illustrates this with the the blue data being the visual magnitude of the unfiltered light reflected from the Anik F1 spacecraft seen in Figure 2.5(b), taken at three second intervals and the green data being taken

of the same object at the same but at a rate of approximately one image every two minutes. It can be seen that there are variations in brightness of the target that cannot be seen in the lower resolution data. While the variations in brightness in both the higher and lower temporal resolution data remain largely unexplained, the implication that temporal resolution is an important consideration to optical observations.

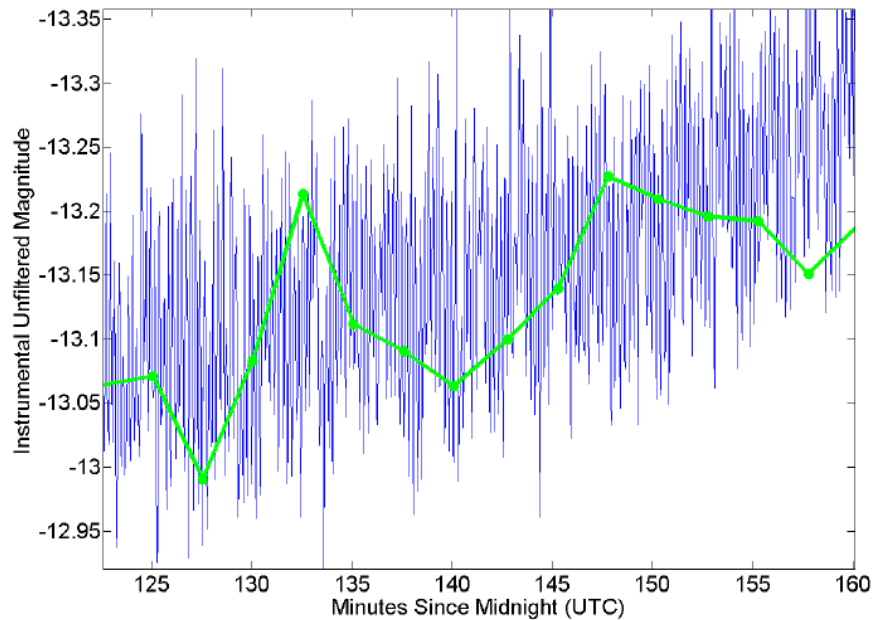


Figure 2.6: Instrumental magnitudes of Anik F1 on the night of 4th November 2013. Blue data at three second resolution courtesy of Mr. Mike Earl, and the green data at two minute resolution [6]

Conversely, the same illustration leads Jolley to suggest that small aperture telescopes exhibit particular advantages to the advancement of the photometric study of RSOs through their portability, affordability and ease of use [6]; as both sets of data were obtained using small aperture telescopes. A general conclusion can be drawn that small aperture telescopes provide a level of observational flexibility to researchers that may not be available through larger observatories, and therefore represent an additional resource to be exploited.

2.3.3 Spectrophotometry

Spectrophotometry aims to separate the incident flux into its constituent wavelengths, and in this sense could be viewed as being similar to broadband photometry, albeit with higher spectral resolution [6]. Howell [35] provides a similar description, giving the size of the wavelength ‘bins’ that the flux will be separated into to be $\Delta\lambda$ in size, where the flux of each bin can then be measured. The resulting distribution of energy as a function of wavelength is referred to as the spectral energy distribution (SED) of the light [7].

Jorgenson *et al.* [36] demonstrated the possibility to differentiate between different spacecraft materials by investigating their SED [36] and produced a database of material spectral energy distributions. This work was furthered by Bédard [7] who illustrated its use by analyzing the spectral distributions of the color ratios of Earth-orbiting satellites by integrating his results across specific bandpasses, and finding their ratios. His work demonstrated (amongst other results) the geometry-dependent nature of photometric results and the ability of spectrometric imaging to aid in satellite discrimination [7]. Figure 2.7 shows an example of Bédard’s results. The different spectral response for the four different solar cells illustrates the promise spectroscopy shows to perform a level of RSO characterization. Of note, the upper-most two solar cells are of similar design and manufacture, yet produce discernibly different spectral responses.

A further interesting example of the application of spectroscopy to spacecraft characterization can be seen in the work of Bowers *et al.* [37] who applied polarised and unpolarised light sources to various materials and recorded the spectral responses in a laboratory environment [37]. He concluded that the change in SED with respect to both polarisation and illumination/observation geometry can indicate changes to the sample’s orientation with respect to the observer, and also provide a means of differentiating between materials. Of note, the illuminating light used by Bowers was polarised; an important distinction to make when comparing results to those obtained through passive polarimetry.

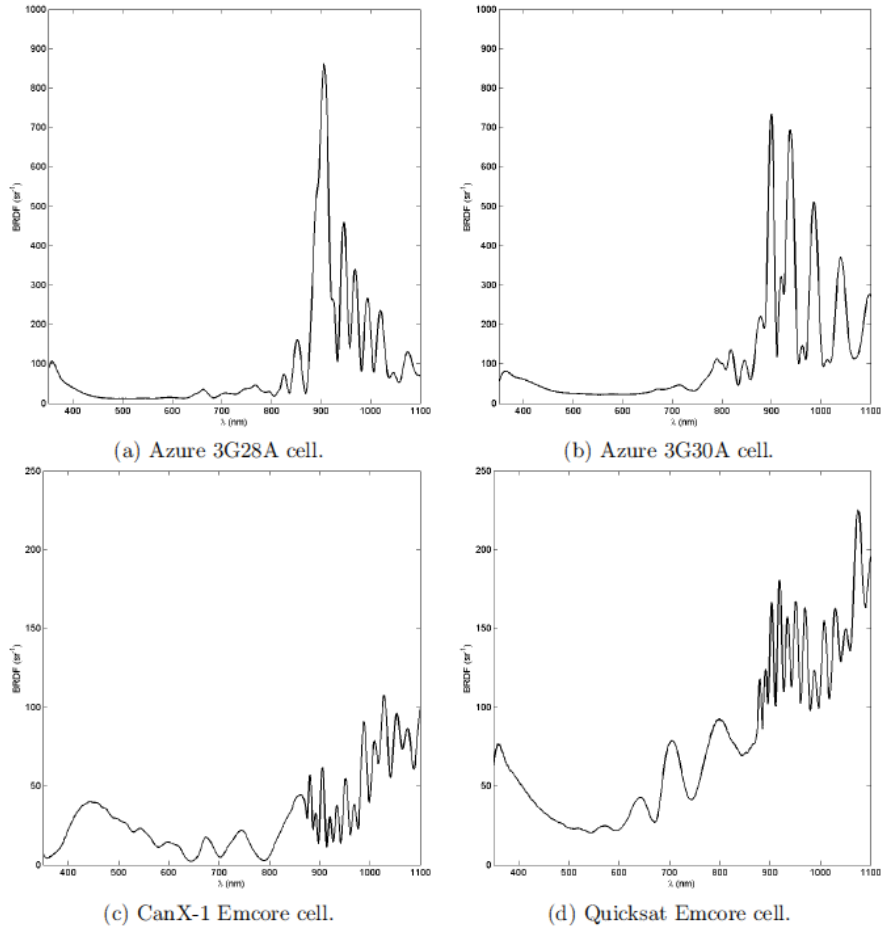


Figure 2.7: Results produced by Bédard, showing the spectral response of four different solar cells at the same observational geometry [7].

2.4 Polarimetry

The study of polarimetry as it applies to the problem of characterizing RSOs has been investigated since at least 2008 by Giakos *et al.* by suggesting a design for an active, laser-based multi-spectral imaging system for space surveillance [38]. Additionally, there are numerous instances of the polarimetric response of spacecraft materials being investigated amongst the surveyed literature with one of the earliest being undertaken by Culp *et al.* in 1995 [8].

The use of polarimetric techniques as a means through which characterization of RSOs, or at least RSO construction materials is possible has been recognized as a promising avenue of research ever since. As a convenient means of describing the various methods, categorizing each generally as either active or passive will be used. The active investigations are those in which polarised light is used to illuminate the target, and passive includes those that illuminated the target with unpolarised, or natural light. Each method will be briefly explained, highlighting the major differences and review of the work conducted within each general technique.

2.4.1 Active Polarimetry

The active polarimetric characterization of materials involves the use of a system of optical representations called Mueller calculus, named for H. Mueller who pointed out that in 1948 the Stokes vector could be regarded as components of a 4x4 matrix [18, 39].

The principle of the method is that the output (reflected or transmitted light beam) Stokes vector ($\vec{\mathbf{S}}_{out}$) can be constructed through the manipulation of the input light Stokes vector ($\vec{\mathbf{S}}_{in}$) by a matrix (\mathbf{M}), with the relation described by:

$$\vec{\mathbf{S}}_{out} = \mathbf{M} \cdot \vec{\mathbf{S}}_{in} \quad (2.4)$$

where \mathbf{M} is called the *Mueller Matrix* [40]. \mathbf{M} then represents the polarimetric properties of the illuminated sample. Lu and Chipman [10] describe a process for determining the Mueller matrix of material through a system of 16 individual polarimetric measurements of the sample. The sample is illuminated by a light source of known wavelength and polarisation state, with the the polarisation state being rotated through horizontal, vertical, left and right-handed circular polarisation states. The reflected (or transmitted) light energy is then sampled for the same four polarisation characteristics allowing

the 16 polarimetric measurements to be used in a system of 16 equations to solve for each element in the Mueller matrix [41]. A more thorough explanation of Mueller calculus and Mueller matrix decomposition is provided at Appendix B.

Notwithstanding, Mueller matrix decomposition fundamentally requires that all aspects of the illumination-sample-observer geometry be known and controlled, and that the sample is illuminated by light of a known frequency and polarisation state [28, 40]. By doing so, a material's full Mueller matrix can be determined and decomposed into meaningful physical characteristics. This process is called *Lu-Chipman decomposition*.

A conceptual illustration of the physical elements needed to perform Lu-Chipman decomposition is seen in Figure 2.8.

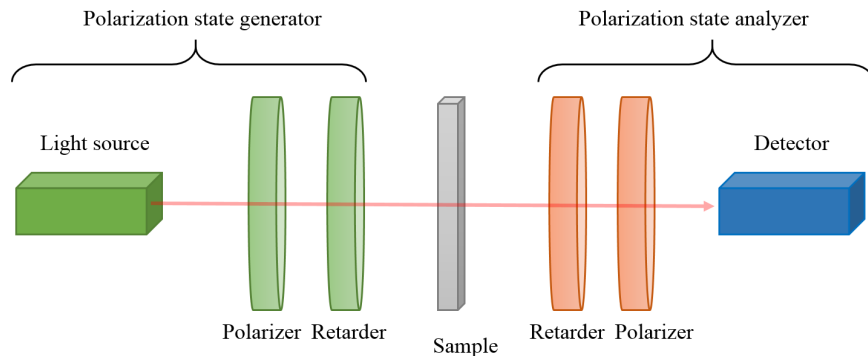


Figure 2.8: Conceptual illustration of the optical elements required for active polarimetry. Adapted from Goldstein [40].

When the requirements of active polarimetry are viewed within the SSA context, it can be imagined that a practical system used for characterization will experience numerous difficulties. These may include the time taken to fully sample the target [42], changes in target orientation during this time and would require a means of actively illuminating the target, most likely with a laser. Once these difficulties are overcome however, Mueller matrix decomposition represents a potential method of RSO characterization.

As a result the technique has been a topic of much research. A small selection of notable works is contained within Table 2.1 and reviews work

completed by Petermann *et al.* in 2012, Bowers *et al.* in 2011 and most recently by Shrestha *et al.* and Pasqual *et al.* in 2015. This review is not exhaustive but illustrates the thematic trends in active polarimetry research.

It should be noted that these research endeavors were laboratory efforts only, and were not performed with orbiting objects.

All of the works noted have at their heart some form of Mueller matrix decomposition, and therefore make them unsuitable to passive observations. Pasqual *et al.* suggest that characterization of orbiting RSOs is possible using a laser radar to irradiate their surfaces with light of a known polarisation state, detect the reflection and then from a library of materials, or a classification system, describe what the material may be. Pasqual *et al.* conclude that this method has benefits over the passive case of being able to distinguish particular materials; a complementary result to those presented by broadband photometry and spectro-photometry.

Of interest amongst the works presented is the influence of α , or the lack thereof. By considering the suggested active polarimetry systems where the source of illumination and the observer are co-located, Figures 2.4 and 2.8 can be combined to show the effect on α . Figure 2.9 illustrates the situation. By substituting the Sun vector (\vec{n}_{Sun}) for a vector pointing to the illuminating laser (\vec{n}_{ill}), it can be seen that the phase angle will be a function of the distance between the laser and the observing telescope. It will also be constant throughout all observation regimes, and the observations will not be limited by the Earth's shadow.

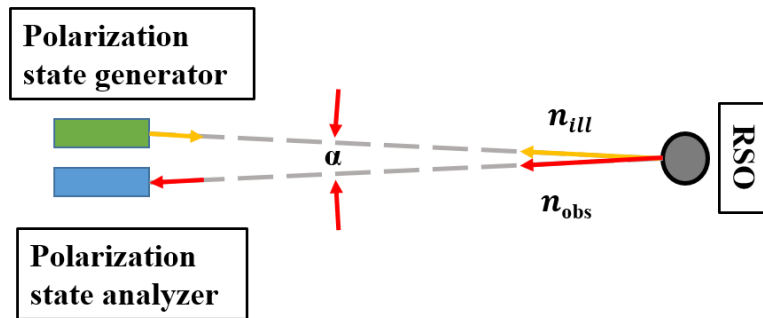


Figure 2.9: Illustration of phase angle in an active polarimetry system.

Notable Active Polarimetry Works		
Name, Year	Fundamental Investigation	Primary Conclusions
Petermann <i>et al.</i> , 2012 [42]	Mueller matrix determination of common spacecraft materials	Characterized Mylar film, Kapton and 2x Solar cells. Illustrated the utility of the method to be used by AFRL imaging polarimeter. Suggested a method for determining the angle of normal incidence of the material.
Pasqual <i>et al.</i> , 2015 [11]	Polarimetric BRDF determination of spacecraft materials	Measured polarimetric BRDF with respect to incidence angle and in-plane scatter (observation) angles. There were notable and particular trends in each materials. Laser radar may be able derive polarimetric characteristics of orbiting debris.
Shretha <i>et al.</i> , 2015 [41]	Characterization of materials using inverted Gaussian estimation and fractal analysis of the depolarisation, diattenuation and retardance sub-matrices.	Presented new methods to differentiate between material types, including between metallic and non-metallic materials. Modeled a real-life laser-based sensor. Showed that the operational design and data reduction methods proposed would be useful in discriminating between orbiting man-made objects.
Giakos <i>et al.</i> , 2015 [9]	Design, calibration and testing of an automated active polarimetric imaging system for characterizing LEO objects	Proposed a design able to use either a CCD or photo-detectors to produce images of Mueller matrix elements. Concludes that optical polarimetry in combination with active illumination would be useful for object discrimination.

Table 2.1: A review of notable recent works in the characterization of spacecraft materials using active polarimetry and Mueller matrix decomposition.

Spectralon

The polarimetric behavior of Spectralon white reflectance standards has been investigated separately by Goldstein *et al.*[40], Bhandari *et al.*[28] and Svensen *et al.*[43] In all cases except that conducted by Bhandari *et al.*, a form of Mueller Matrix decomposition was used [28, 40, 43]. Of note, all three investigators drew conclusions that the polarimetric behavior of Spectralon begins to deviate significantly from that of a Lambertian surface for large illumination incidence and scattering angles. This is an important consideration for the experimental component of this thesis.

2.4.2 Passive Polarimetry

Unlike active polarimetry, passive polarimetry cannot make use of Mueller matrix decomposition as the target object or sample is illuminated by unpolarised light, and cannot be altered. In practice the illumination would be provided by the Sun. As pointed out by Chenault *et al.*[44], Svensen *et al.*[43] and Pasqual *et al.*[11], the Mueller matrix provides the most complete information about the polarimetric nature of a sample. Pasqual *et al.* further suggest that as a result of this, active polarimetry is able to produce a comparatively higher level of knowledge of an objects polarimetric signature compared to passive polarimetry. Passive polarimetry is further complicated by the impact of changing observation and illumination geometries.

Investigations into the polarisation characteristics of unpolarised light reflected from common materials found on artificial satellites has been completed, most notably by Culp *et al.* [8] as part of a NASA research grant undertaken at the University of Colorado. Its aim was to investigate the reflective polarisation effects of materials such as Mylar, Kapton and aluminum to aid in the identification and tracking of space debris [8]. This investigation presents the closest replication of the passive polarimetric analysis of spacecraft materials, and the only identified experiment that attempts to further the use of passive optical polarimetry to address the challenge of RSO characterization.

Figure 2.10 provides a graphical description of the general arrangement of the experiment. The report does not make clear whether the sensor could be moved independently of the test object. The samples were illuminated by a collimated beam of unpolarised light while the sample surface normal remained in the same plane as the illuminating light beam. The description

provided for the light-sample-sensor geometry is unclear, other than stating that the sample was arranged at 20° and 30° with respect to the normal of the incident light when the measurements were taken. It is assumed from this description that the sample was illuminated at angles between 20° and 30° .

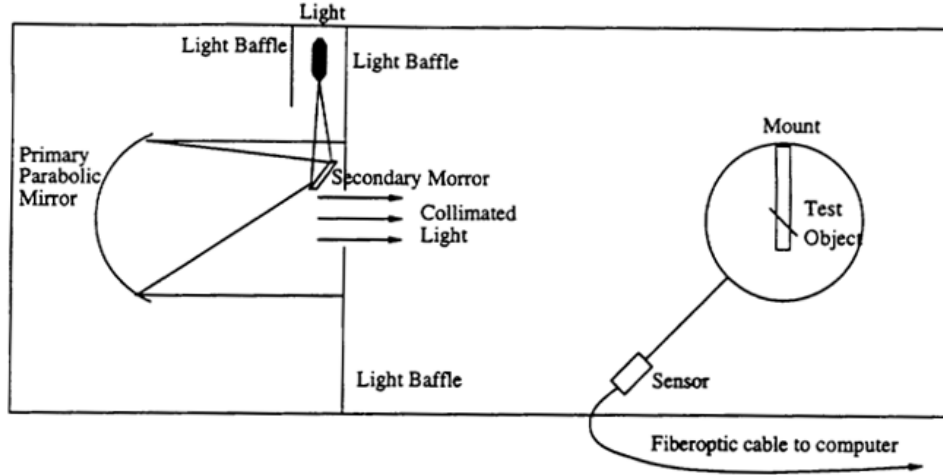


Figure 2.10: A plan view of the experiment conducted by Culp *et al.*[8], showing the general layout as provided by the authors.

Additionally, the range of ‘phase angles’ over which data was taken was provided as ‘ -35° to 135° ’. As the report does not make clear the coordinate system used nor clearly define what quantity ‘phase angle’ refers to, this quantity is not referred to as α as presented in Section 2.2 to avoid confusion.

Measurements were taken generally every 5° within the phase angle range, and every 1° within 20° of the specular reflection direction for the more specularly reflecting test subjects. The polarizing element used was a double Glan-Taylor linear polariser. The core relation used for the investigation was to describe the ‘amount of polarisation’ as the ratio of the difference and sum of the perpendicular and horizontal polarisation components, provided by Culp as:

$$P = \frac{P_{perp} - P_{horiz}}{P_{perp} + P_{horiz}} \quad (2.5)$$

This equation relates quite closely to Equations 1.21 and 1.26 seen in Section 1.4. From the description, the $P_{\text{subscript}}$ values are the ‘perpendicular and horizontal polarisations’ with respect to the experimental plane, and represent orthogonal polarisation intensity measurements. If the light beam has a state of polarisation that exists purely in either the 1st and 3rd quadrants, or 2nd and 4th quadrants, the Stokes parameter of the reflected light (S_r) is:

$$S_r = \begin{bmatrix} 1 \\ 0 \\ \pm 1 \\ 0 \end{bmatrix} \quad (2.6)$$

it can be realized that applying Equation 2.5 will return a value of zero which is incorrect. This indicates an incorrect understanding of the application of Equation 2.5. This may be explained through texts such as Clarke [21] and Hecht [13, 14] which provide a relation that is very similar in appearance to Equation 2.5, but very different in application. This relation gives the *degree of polarisation* (P) as:

$$P = \frac{I_{\text{max}} - I_{\text{min}}}{I_{\text{max}} + I_{\text{min}}} \quad (2.7)$$

where $I_{\text{subscript}}$ gives the maximum and minimum intensities of a beam of light measured by a linear polariser as it is rotated through 180°. As would be expected, these maximum and minimum values would be found at orthogonal linear polariser positions. It is an understandable, but incorrect conclusion for Culp *et al.* to apply this equation assuming that the maximum and minimum values will be found at the horizontal and perpendicular directions with respect to the experimental coordinates.

It can be seen however, that the numerator relation of $P_{\text{perp}} - P_{\text{horiz}}$ is that used to produce the Stokes Q parameter. In the combination as presented, Culp *et al.* do not measure the degree of linear polarisation, but rather the Q Stokes parameter (assuming a coordinate system based on the normal interpretation of horizontal and vertical directions) which has been normalized to the total intensity. An example of the results provided by Culp *et al.* is seen at Figure 2.11. The dotted line indicates the experimental data and the solid line a line of best fit to the experimental data.

This figure appears to confirm the incorrect application of Equations 2.5 and 2.7 as it illustrates a calculated ‘amount of polarisation’ of less than 0%. Plainly this is unachievable as a measurement of total polarisation, but is a

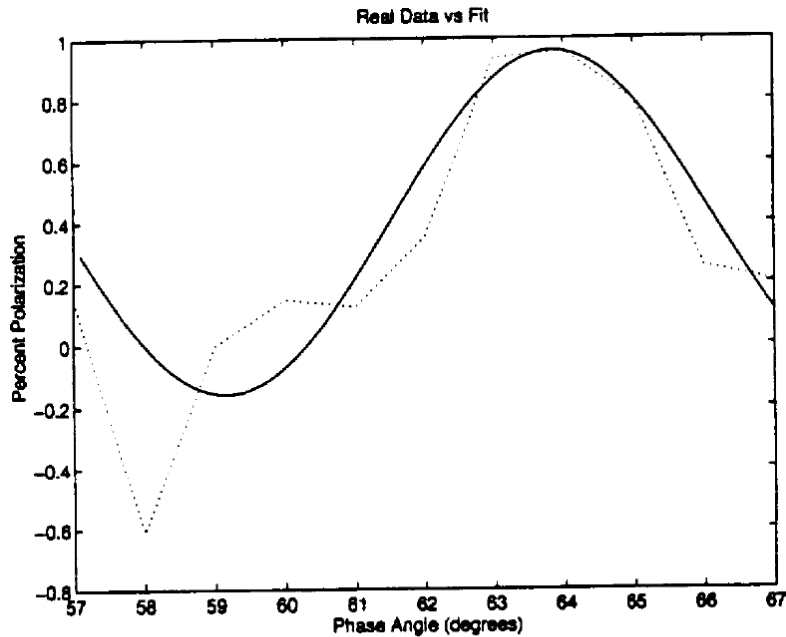


Figure H.9: Aluminum Sample

Figure 2.11: Example of the results obtained by Culp *et al.* for an Aluminum sample [8].

coherent result for the Q Stokes parameter. The conclusion is therefore that the data reduction process employed by Culp *et al.* was fundamentally flawed. As such, it is difficult to retrieve meaningful conclusions from the experimental report produced by Culp *et al.* beyond generalisations.

If Figure 2.11 is regarded as the Stokes Q parameter instead of ‘percent polarisation’ with respect to ‘phase angle’, it can be seen that the Q Stokes parameter approaches ± 1 at certain points. This is sufficient to suggest that the aluminum sample displayed polarizing characteristics. This same result was also seen for the other tested samples. Additionally, Culp *et al.* qualitatively suggest a link between ‘polarisation signal’, surface reflectance properties and observational geometry [8]. While there was ambiguity within the descriptions of geometry and a flawed calculation of total polarisation, it could be suggested from the results that the general observation holds true.

Lastly, Culp's investigation aimed to investigate materials properties only. The impact of the results to the SSA mission was not explored.

2.4.3 Un-resolved Issues

The literature survey has highlighted consistent themes within the optical characterization methods of RSO and RSO materials and the understanding of how they can contribute to SSA. They include the observational and geometric dependency of results, the utility of small aperture telescopes and a propensity to present results with respect to phase angle.

When considering the body of work dedicated to polarimetric characterization, specific trends persist throughout the literature and demonstrated results. An effort to relate the work of passive investigation to the practical problems presented by optical SSA as it exists today is lacking. The use of lasers and active polarimetry is similarly un-helpful in more thoroughly understanding the role, advantages and disadvantages of passive polarimetry as a means of RSO characterization. The lack of robust experimental data supporting or refuting the utility of passive polarimetry is similarly highlighted. As a result, this experiment aims to provide a first stepping stone to the following questions:

1. Can the relative degree and angle of linear polarisation for different materials be measured in a laboratory environment?
2. Is there an illumination and observational dependency on the measurable degree and angle of linear polarisation?
3. Is it possible to use a polarimetric response to distinguish between spacecraft materials?
4. Is it possible to derive polarimetric information about an observed RSO through the use of a linear analyzing polaroid, and widely used SAT technology?
5. Are the relative differences in the polarimetric information derived using existing optical observation equipment sufficient to encourage further research?
6. Does the polarimetric response of an RSO have a dependency on the attitude of the RSO with respect to the light measuring system, or is it possible to infer spacecraft attitude from a polarimetric response?

3 Laboratory Experiment

3.1 Introduction

This chapter describes the laboratory experiment that was conducted to investigate the dependence of the induced polarisation of reflected light on material type and observation geometry. In-depth descriptions of the major components, data gathering process and data reduction process are provided. Challenges encountered throughout the experiment are covered where appropriate, including technical and physical limitations of the laboratory environment.

3.1.1 Background

Investigation into the polarimetric behavior of individual materials has been undertaken previously, some using active investigation means (e.g. those studies involving the use of Mueller matrix decomposition such as those of Shrestha *et al.* [41] and Giakos *et al.* [9]), and others using passive methods [8]. Despite this, it could be said that the study of the application of passive polarimetric investigation to the SSA mission has been largely ignored.

To gain further insight into the polarimetric characteristics of light passively gathered from the reflections of RSOs and build upon the results obtained by Culp *et al.*, an experiment was designed to observe the change in polarisation of reflected light from spacecraft materials with respect to the incident and reflection angles. We used standard procedures for the analysis of CCD photometry, similar to those typically used for analysis of real telescopic observations of RSOs.

3.1.2 Experimental objectives and scope

There were two main objectives of the experiment. The first was to measure the polarisation induced in light reflected from the surfaces of a variety of

materials commonly found on the surfaces of spacecraft and how this varies with observation geometry. The second was to evaluate whether the study of the polarisation of light reflected from RSOs is of benefit to the optical characterization of RSOs within the SSA context.

An additional, collateral objective was to identify parameters that could guide the development and construction of a polarimeter suitable for use with small aperture telescopes for RSO observation and characterization. While not being a guiding consideration, the ability to further explore and extend where possible the capabilities of the SSRL's Optical Reflectance Laboratory was deemed .

3.1.3 Experimental requirements

There were requirements placed on the experiment that drove selection of individual components.

1. The selection of an appropriate CCD was based largely on well-depth and gain. The experiment required that the CCD should provide measurements without saturation of highly specular materials, while also being capable of measuring small fluxes from diffuse materials. As such, a higher gain was preferred such that saturation would not occur at the minimum possible exposure time. The CCD needed to have the ability to have a lens and an optical filter attached.
2. The experiment required precise positioning repeatability of the analyzing polaroid, and a precise sample angular displacement capability. A software system allowing automated manipulation of the analyzer and sample orientations coupled with an efficient duty cycle was preferred.
3. A need for the experiment to allow a wide range of observational geometries was identified. A range of light incident angles ranging from as close as possible to 0° to 90° was desired. A range of observation angles of at least $\pm 3^\circ$ from the specular reflection angle for the range of incident angles was also required.

3.2 Experimental set-up

The major components of the experiment consisted of a collimated light source, sample goniometer, analyzer and light metering system. Figure 3.1 provides a conceptual description of the experiment layout, and Figure 3.2 illustrates the experiment.

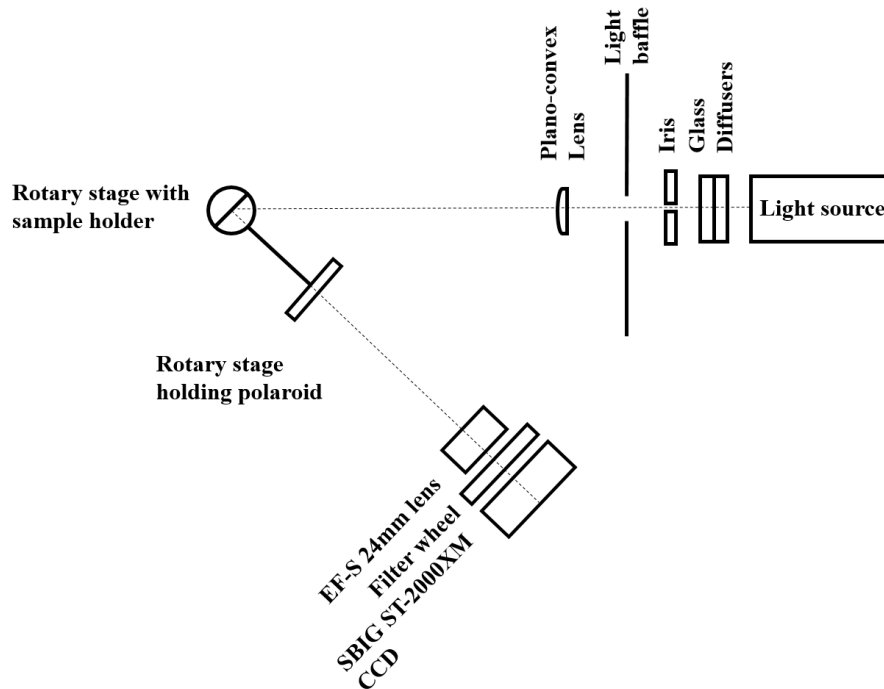


Figure 3.1: A conceptual representation of the experimental layout.

3.2.1 Collimated white light

A near-collimated light source was achieved using a Ushio JC14.5V 50 watt QTH lamp. The lamp was electro-thermally cooled to prevent overheating, and was powered using an un-interruptable power supply (UPS) to limit light intensity variance through power source oscillations. Two fused silica ground glass diffusers were used, a DGUV10-600 and a DGUV10-125, both sourced from Thorlabs. The selection of diffusers was made to achieve the most uniform illumination spot possible by reducing the relatively brighter bulb filament artefact evident in the light beam. Both diffusers had a manufacturer stated light transmission of greater than 90% in the bandpass of 350nm to 1100nm.

An iris diaphragm was then placed in the optical path. The diaphragm was adjusted to allow the CCD to achieve an acceptable signal to noise ratio with exposure times of 10 seconds or less at the off-specular directions, whilst preventing the CCD from saturation at the specular directions.

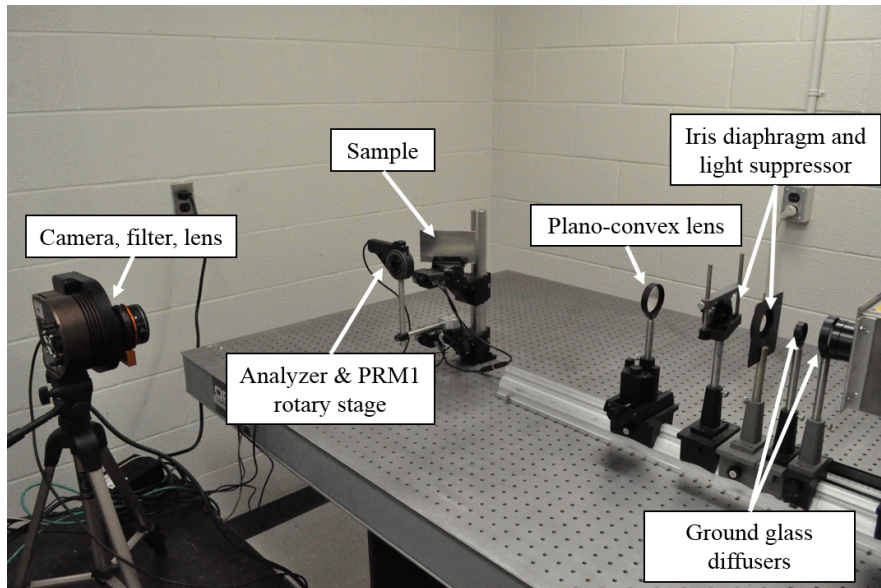


Figure 3.2: A photograph of the experiment with the light suppression boards removed.

A secondary consideration was to achieve an illuminated area of the sample much greater than the size of the small scale surface inhomogeneities of the samples such as manufacturing marks and scratches. This was done to negate small scale scattering effects from the sample to more closely replicate the practical environment. Lastly, a plano-convex lens was placed in the path such that its focal point corresponded with the iris diaphragm. This produced a nearly collimating light beam. The light source, excluding the plano-convex lens, was then baffled to reduce undesired light from reaching the sample and CCD. Figure 3.3 shows the light source and attendant optics with the light baffle removed.

3.2.2 Goniometer

The mounting device for the sample and analyzing polaroid was built around two Zaber T-RSW60A motorized rotary stages. These were mounted on a vertical post and aligned such that their axes of rotation were arranged vertically and co-incident. The top rotary stage functioned as the sample holder and held a machined aluminum bracket capable of holding all the required samples. The sample holder was covered in a diffuse black tape to reduce

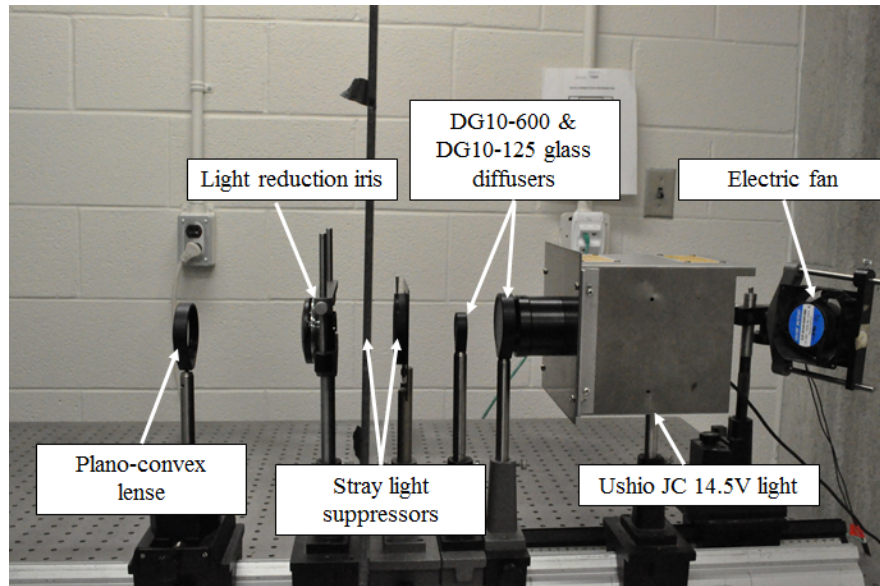


Figure 3.3: Light system components.

unwanted light reflections.

The lower rotary stage held a post arrangement that held the analyzer a constant distance and alignment relative to the sample, and was rotated in the laboratory horizontal plane. Figure 3.4 shows this arrangement.

Both rotary stages were driven independently by Zaber Inc propriety software. This arrangement allowed the sample and analyzer pairing to be rotated with an accuracy of within $\pm 0.1^\circ$ of the desired orientation, as estimated by the experimenter.

3.2.3 Analyzer

The analyzing linear polariser that was used was the LPVISE100-A produced by Thorlabs. It is a 1 inch linear polariser consisting of a dichroic polarizing film mounted between two anti-reflection N-BK7 glass windows. The operating characteristics of the polariser are provided in Table 3.1. The selection of this analyzer was made with regard to its effective bandpass and transmission factor.

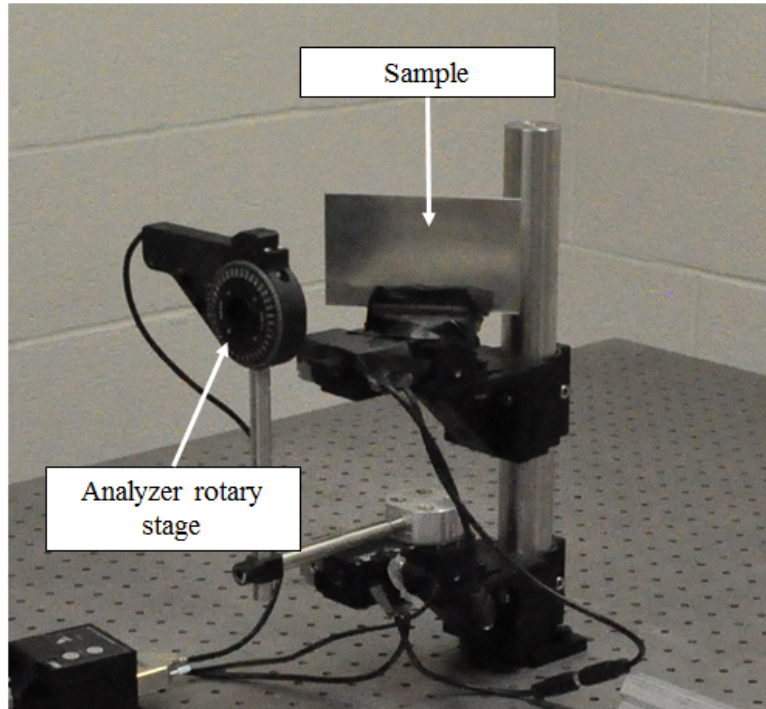


Figure 3.4: The two rotary stages of the goniometer with the 6061-T6 sample mounted in the sample holder. The black tape seen on the lower portion of the sample suppresses light being reflected from the sample holder onto the surface of the sample. Note the analyzer rotary stage mounted on the post, aligned vertically with the sample.

LPVISE100-A Linear Polariser	
Transmission (polarised)	0.73 (average over bandpass)
Transmission (unpolarised)	0.41 (average over bandpass)
Extinction Ratio	> 1 : 100 – 5000 (at limits of bandpass)
Bandpass	400-700nm

Table 3.1: Operating parameters of the analyzing polaroid provided by Thorlabs, Inc [45].

The transmission performance data for the analyser was also supplied by Thorlabs and is presented in Figure 3.5.

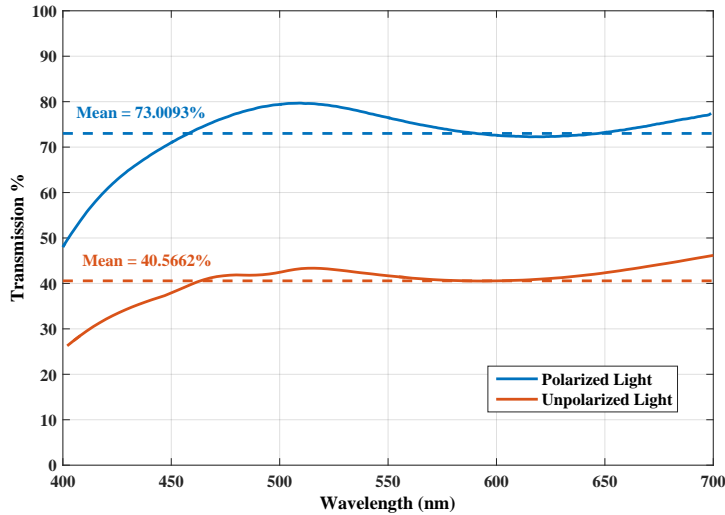


Figure 3.5: Linear polariser transmission performance, supplied by Thorlabs.

The polariser was mounted in an PRM1/MZ8 motorized rotation mount, acquired from Thorlabs Inc. An image of the analyzer rotary stage is seen at Figure 3.6.

It was mounted such that its normal was coincident with the required direction of observation, and its optical axis aligned with the 0° indentation of the rotary stage. The analyzing linear polariser was then able to be precisely rotated to the four required orientations. The analyzer holder was manipulated using the manufacturer's software, with a manufacturer-quoted absolute repeatable accuracy of $\pm 0.1^\circ$.

3.2.4 Imaging system

The imaging system consisted of three components, a lens, a filter wheel and a CCD.



Figure 3.6: Analyzer rotary stage with analyzer polaroid mounted. Note, the rotary stage has rotated the optical axis of the polariser to the 90° position.

Lens

The lens selected was a Canon EF 24mm f/2.8 wide-angle camera lens. The relevant specifications are contained in Table 3.2.

Canon EF 24mm f/2.8 wide angle lens	
Focal length	24mm
Maximum aperture	1:2.8
Diagonal field of view	84°
Minimum focus distance	0.2m

Table 3.2: Specifications for the Canon EF 24mm f/2.8 lens.

A wide field of view was chosen to imitate the on-sky environment. When combined with deliberate de-focussing of the image onto the CCD, the small-scale irregularities of the samples were able to be negated.

Filter wheel

A visual bandpass filter (400-700nm) was used between the lens and the CCD. It was mounted in the filter-wheel attached to the front of the CCD.

CCD

Lastly, the CCD selected was the Santa Barbara Instrument Group (SBIG) ST-2000XM. Table 3.3 contains the relevant operating specifications of the CCD.

SBIG ST-2000XM CCD	
ADU converter	16 bit
Gain	0.6 e ⁻ /ADU
Array size	1600 x 1200 pixels
Pixel size	7.4 x 7.4 μm
Dark current	<0.1 e ⁻ /pixel/sec
Read noise	7.9 e ⁻ rms
Bias	100 ADU
Full well capacity	45000 e ⁻
Exposure times	0.001 to 3600 sec

Table 3.3: Specifications for the SBIG ST-2000XM CCD.

A challenge for this experiment was being able to select a CCD with a gain that would allow both quite specular and diffuse materials to be imaged throughout the entire experiment. It was found that while imaging the white painted panel or the triple junction photo-voltaic (TJPV) cells with a CCD with a gain of 0.3 for the shortest possible exposure would saturate the CCD. The ST-2000XM, through the higher gain value of 0.6 and a minimum useful exposure time of 0.01 seconds, was able to capture all samples throughout the

range of observation geometries, and still be able to image the diffuse materials at the larger off-specular observation locations.

Alignment

Alignment of the imaging system was achieved through the use of a mirror and laser. Firstly, a mirror was placed in the sample holder and a laser placed on the light source rail such that the laser would propagate along the same path as the collimated light beam. The mirror then allowed the specular position of the reflection beam to be located precisely. The camera was then positioned and leveled by hand such that the reflected laser beam fell on the center of the lens. Care was taken to ensure that the surface of the lens was located perpendicular to the propagation direction of the beam. The mirror was then replaced by the sample to be tested, and the laser removed.

3.3 Material samples

The materials available and selected for analysis were:

- Spectralon reflectance standard
- 6061-T6 aluminum alloy plate
- Aluminum plate painted with Lord Aeroglaze 276A Reflective White, low out-gassing paint
- Azur Space 3G28A TJPV cell
- Emcore A TJPV cell from the CanX-1 program

and can be seen in Figure 3.7. The Spectralon, painted panel and Azur cell were evaluated to be in pristine, or near-pristine condition in that they had no obvious surface scratching or degradation. The 6061T6 Aluminum and Emcore cell had poor surface conditions. Both exhibited surface scratching and discoloration, evidence of which can be seen in Figures 3.7(b) and 3.7(d). As was mentioned in Section 3.2.1, by illuminating and analyzing a relatively large area of the sample, these surface irregularities could be somewhat negated.

3.3. Material samples

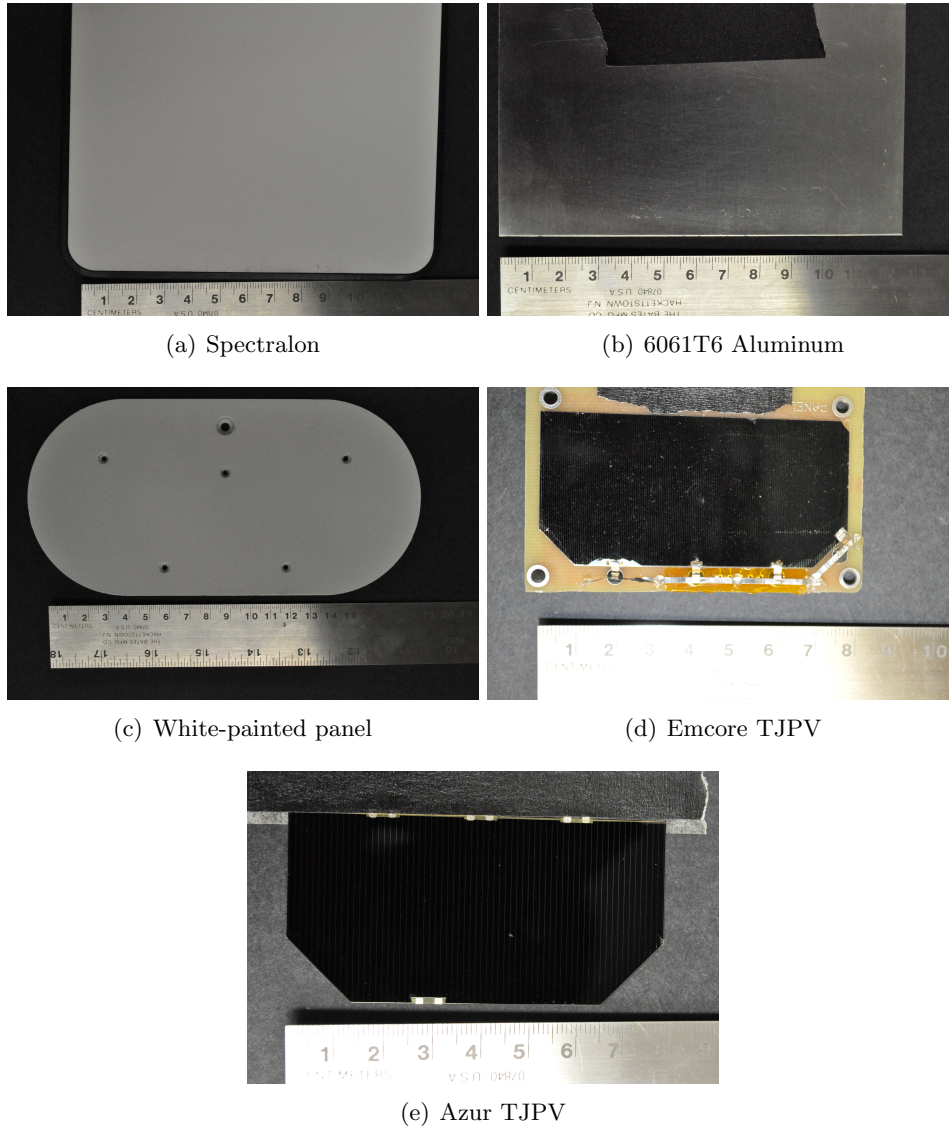


Figure 3.7: Experiment samples

3.4 Data collection

The data collection process required a series of images to be taken for a variety of observational arrangements, for all five material samples. In addition to this a master flat field image was built for each observational geometry.

As was seen with Equation 1.27, the normalized Stokes vector \vec{S}_n can be written in terms of analyzer position as:

$$\vec{S}_n = \begin{bmatrix} \frac{I_{total}}{I_{total}} \\ \frac{I_0 - I_{90}}{I_{total}} \\ \frac{I_{45} - I_{135}}{I_{total}} \\ \frac{I_{rh} - I_{lh}}{I_{total}} \end{bmatrix} = \begin{bmatrix} 1 \\ q \\ u \\ v \end{bmatrix} \quad (3.1)$$

where the subscript notation provides the polariser position relative to the plane of illumination and observation, and the *total* subscript indicates the total reflected flux I , measured in Analogue to Digital Units (ADU), the output of the CCD. Additionally, as the experiment aimed to determine the *linear* polarisation characteristics only, the v Stokes parameter was discarded.

Noting the use of I_{total} to produce the normalized Stokes parameters which is obtained by summing the I_0 and I_{90} images, it can be seen from Equation 3.1 that at least four images are required to be taken for each material at each observation arrangement, with the analyzer positioned at 0° , 90° , 45° and 135° . The apparent non-sequential nature of the list above follows the Pickering formulation [13], and represents a logical method of data acquisition and arrangement for storing and later retrieval. The process employed to obtain these four images is provided in Figure 3.8.

The process resulted in all required images being saved in appropriately named directories ready for processing with the format:

PPP_SSS_Sample_data00n.FITS

where PPP is the phase angle, constructed from the addition of the incident and specular reflection angles, SSS is the angle relative to the specular direction and n is the image number relating to the analyzer position. For example,

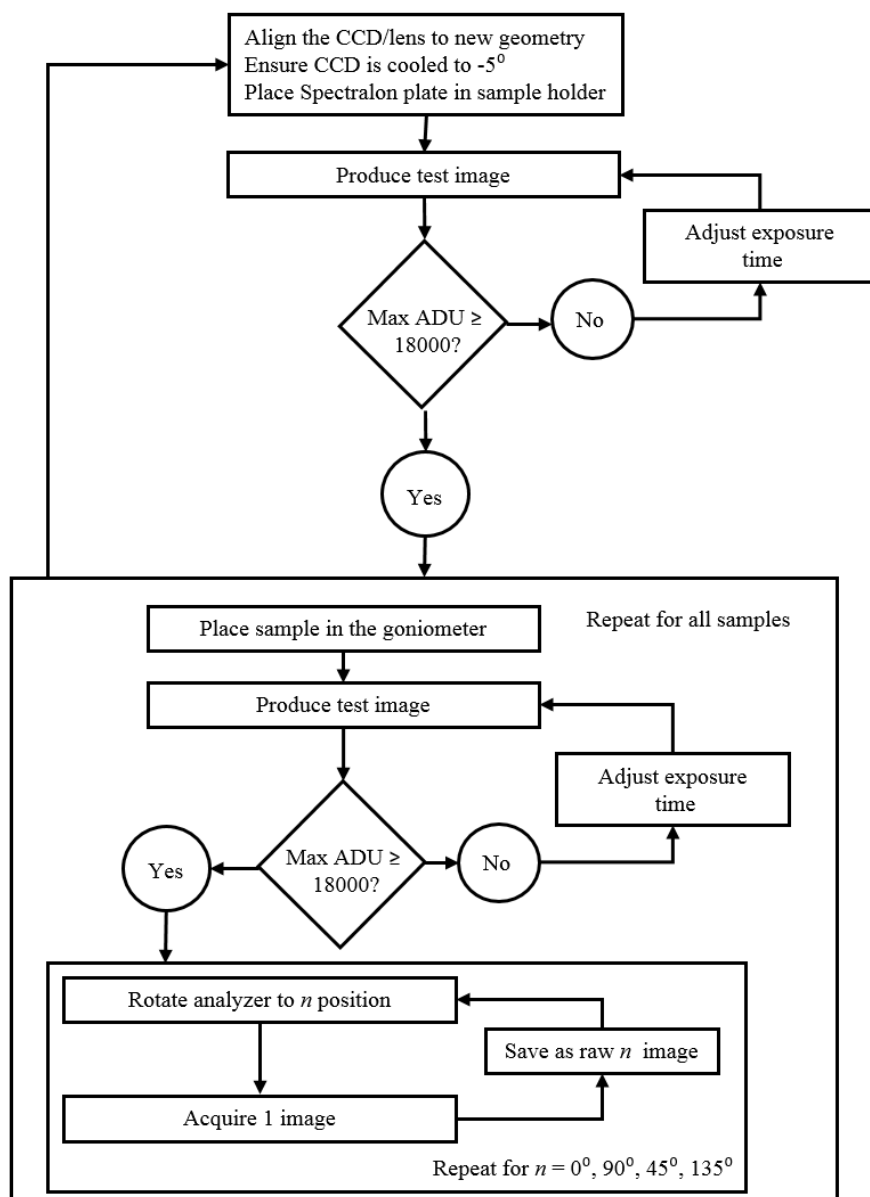


Figure 3.8: Data acquisition flow

90_0_A1_data002.FITS is the image at the specular direction of the 45° illumination angle, with the analyzer at 0° for the aluminum sample. Figure 3.9 gives an example of the raw images collected.

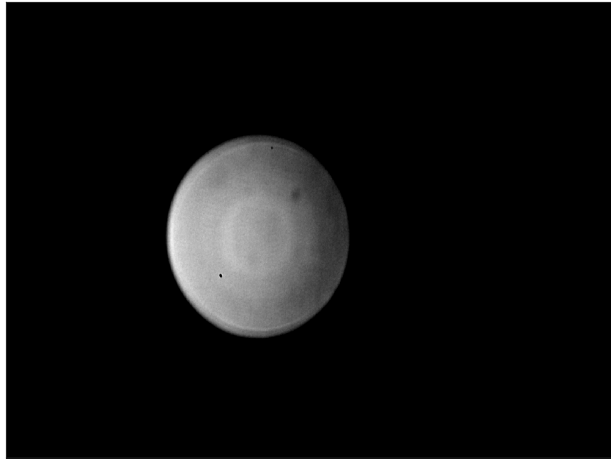


Figure 3.9: Example of a raw data image showing the Azur TJPV cell, at $\theta_i = 45^\circ$. Note the dust spots and the rings within the disk, assumed to be artefacts of the lens.

3.4.1 Master dark and bias

To account for the bias and dark current, master bias and dark images were produced. These were made out of a median combination of 10 images of each type. The dark images were produced with exposure times of 10 seconds with the CCD cooled to the same temperature as used for the data collection images. As the experiment was conducted in a laboratory environment which was temperature controlled, only one master dark and bias image were produced. It was not expected, nor was it experienced, that significant temperature fluctuations would exist over the data collection period. The master dark image shown in Figure 3.10. Of note, the dark image shows that the CCD chip has various artefacts including bright pixels and lines. Whilst noticeable to the eye, these CCD inhomogenities were on a much smaller spatial scale than the area of the CCD used for data capture, and therefore were not expected to alter the results in an appreciable way.



Figure 3.10: Master dark image.

The single master dark and bias images were used as the repositories for the required dark and bias information for all flat field and data image processing.

3.4.2 Master flat

Four master flat images were produced for each observation geometry; one for each of the four analyzer orientations. The Spectralon standard was used as the target surface, with ten flat images taken at each analyzer orientation with the same integration time used for all 40 images. These images were individually bias and dark subtracted before being normalized to their median pixel values. The mean of the ten images was then found, following the process described by Chromey [46]. A process of flat fielding was implemented to remove any pixel to pixel variations within CCD. It also allowed a level of reduction of imaging system inhomogeneities such as the circular feature seen in Figures 3.9 and 3.17 to be achieved. The process used to produce the flat images is explained graphically in Figure 3.11. The general steps employed were:

1. Reduce 10 raw flat images for each analyzer position to the required analysis area,
2. Subtract dark current and bias levels,
3. Divide each image by its median pixel value,

4. Sum all ten images for each analyzer position pixel by pixel, and find each pixels mean value,
5. Store the resulting four images, one for each analyzer position.

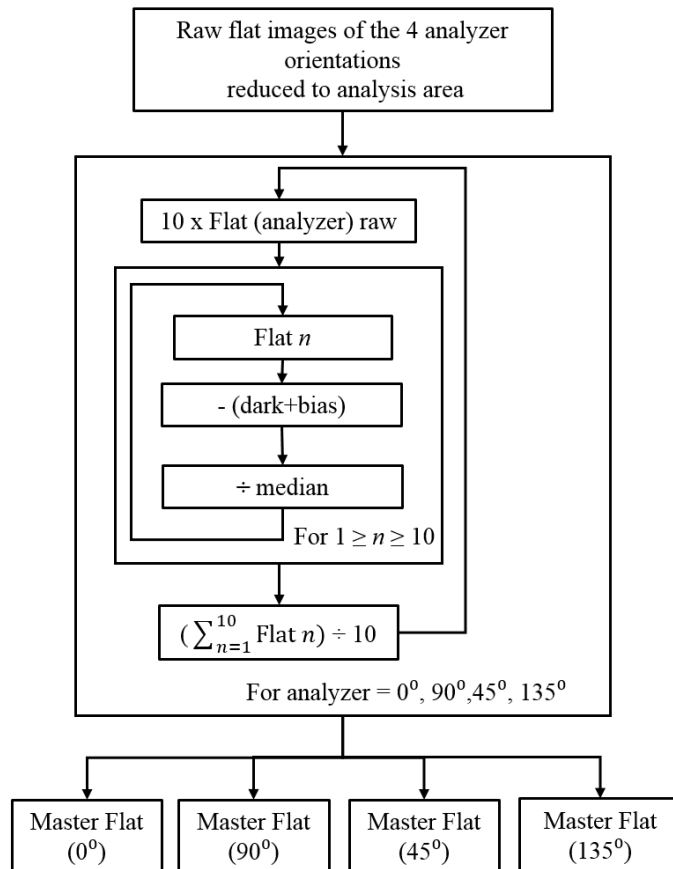


Figure 3.11: Master flat production process. This process is completed for each of the four analyzer orientations. The master bias and master dark images are external inputs.

An example of a resultant master flat image is seen in Figure 3.12. Of note, the individual raw flat images were sub-sectioned to a smaller analysis area prior to their use in producing the master flat image. This is further explained in Section 3.5.1. This example image also shows that the circular features of the data images, as seen in Figures 3.9 and 3.17 are a function of either the imaging system or the analyzer, and not the target sample.

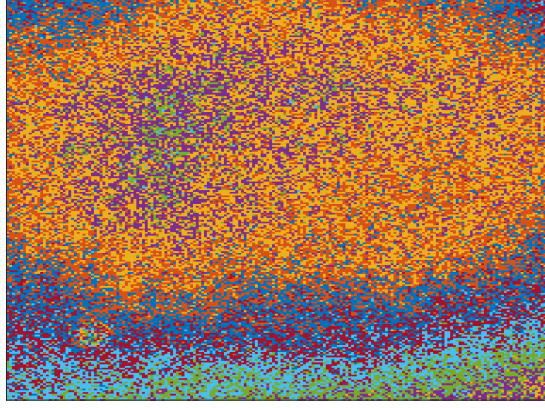


Figure 3.12: Example of a master flat sub-section image of the same size seen in Figure 3.17 at the specular observation angle, with $\theta_i=45^\circ$. This image has been produced with a high contrast color map to show the circular features of Figure 3.17 that can be removed by utilizing a master flat reduction. Note the dust object in the lower left hand corner corresponding to the same in Figure 3.17.

3.4.3 Co-ordinate System

The co-ordinate system used for the experiment uses the normal of the sample surface as a reference axis. Figure 3.13 provides a graphical definition of the coordinate system in Cartesian coordinates, where the cross product of the \hat{Z} and \hat{X} directions provide the \hat{Y} direction and surface normal, with the positive direction definition being towards the hemisphere containing the light source and polarimeter. The positive \hat{Z} direction is towards the roof of the laboratory, orthogonal to the observation/illumination plane. The measurements are taken solely in this plane. Of note, as the sample holder is rotated to achieve the different incident light angles, so too does the coordinate system rotate with respect to the laboratory. The axis of this observation and illumination geometry rotation is the \hat{Z} axis.

The angle of light incident (θ_i) upon the sample is defined as positive in an anti-clockwise direction, with 0° being co-incident with the \hat{Y} direction and increasing towards the positive \hat{X} direction. The angle of observation (θ_{obs}) is 0° at the \hat{Y} axis and increases in a clockwise direction towards the negative \hat{X} direction. The directionality of these two angles was selected for ease of data

recording.

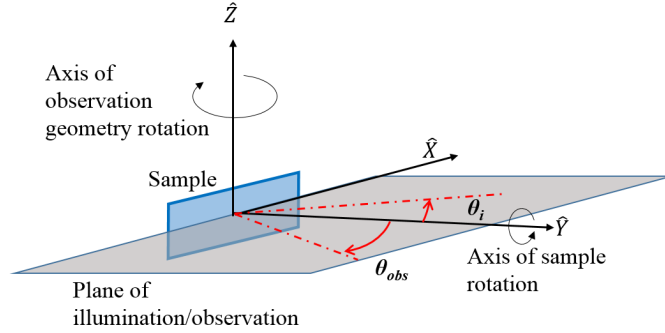


Figure 3.13: A graphical definition of the coordinate system used for the experiment.

It is useful to define a second plane of rotation that is parallel to and co-located with the XZ plane with the axis of rotation co-located with the surface sample normal \hat{n} , which is the same direction as denoted by \hat{Y} . The direction of rotation starts with 0° located in the XY plane, and rotates with positive values anti-clockwise towards the \hat{Z} direction when observed from a $+\hat{Y}$ location. This rotation value was maintained at zero for the experiment, meaning the samples remained ‘horizontal’ to the laboratory and experimental frame of reference throughout. It should not be confused with the rotation used to alter the observation and illumination geometries. Figure 3.14 provides a graphical illustration of the experimental arrangement.

The observation angles selected for analysis were the specular, and three degrees either side of the specular direction in 1° increments. The illumination angles selected were restricted by the size of the laboratory, as were the resulting observation angles. The lower limit to the illumination angle range of 15° was imposed by the light suppression box surrounding the light source, and the upper limit imposed by the laboratory wall preventing the CCD from being located at the specular observation direction greater than 75° as seen in the illustration at Figure 3.15. The set of θ_i angles then selected for use in the experiment was $15^\circ \leq \theta_i \leq 75^\circ$, in 10° steps.

The set of observation angles able to be assessed at 15° illumination angle were impinged by the light suppression box, meaning the range of observations at this illumination angle was restricted to $14^\circ \leq \theta_{obs} \leq 18^\circ$. For the

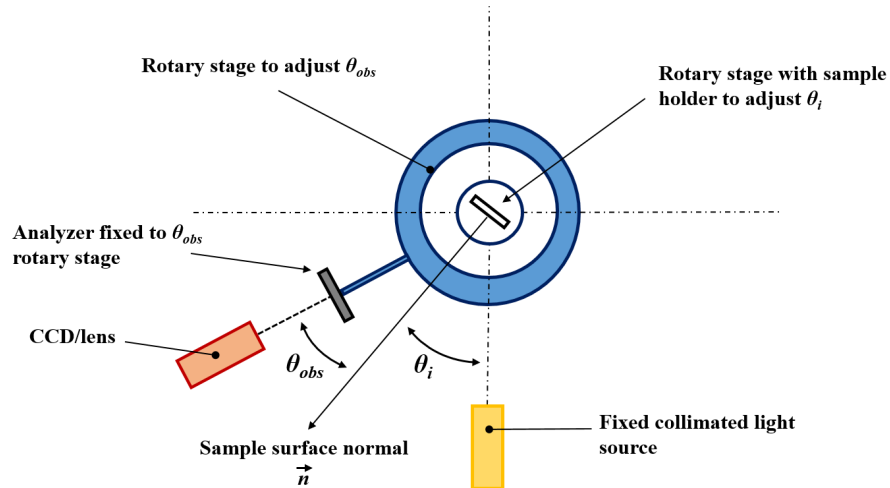


Figure 3.14: Plan view illustration of the experiment showing the angles of illumination and observation

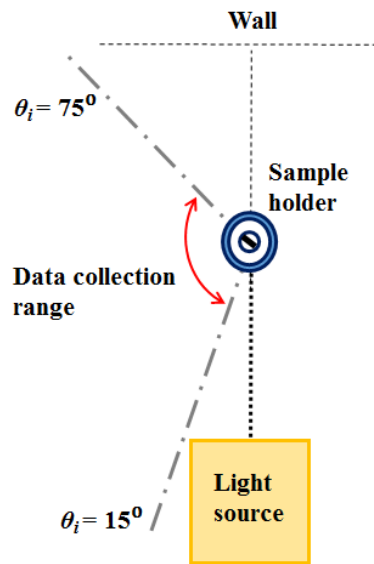


Figure 3.15: An illustration of the experiment showing the effect of the physical laboratory boundaries on the experiment, specifically on the illumination angles used.

remainder of the illumination angles, θ_{obs} was selected by the experimenter to be $\pm 3^\circ$ of the specular reflection direction. While this selection of observation angles is small compared to those that would reasonably be encountered in an RSO observation campaign, they provide

3.5 Data reduction

All data processing was completed using Matlab 2015b. The initial data reduction procedures followed general CCD photometry procedures [35, 46] used previously at the SSRL[6]. It included the correction of the images for dark current, CCD gain and pixel to pixel variations. The secondary processing allowed the spatially dependent extraction of the I , q and v Stokes parameters, and determination of DOLP and AOP. It followed the general process provided by Tinbergen [17], but also leant on the mathematical derivations provided by Hecht [13] [14] and Clarke [16], and those described in Section 1.3.

The main steps to the data reduction process were:

1. Further processing subsection area identification
2. Dark and bias subtraction
3. Flat fielding
4. Stokes parameter calculation
5. Normalized Stokes parameter calculation
6. Degree and angle of linear polarisation calculation

These steps are illustrated in Figure 3.16. This process was performed for each observation geometry. The inputs to this process were the master bias image, master dark image and the four analyzer orientation master flats.

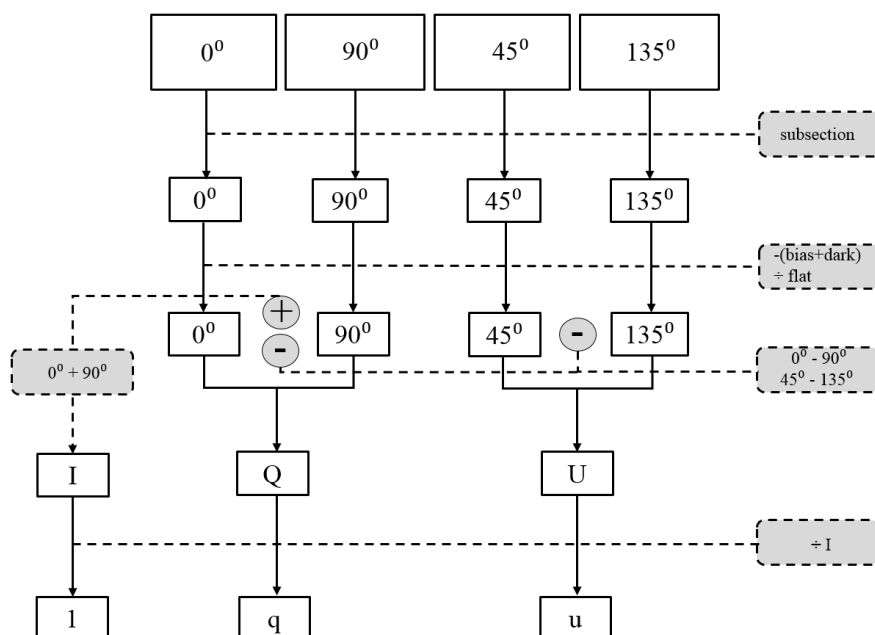


Figure 3.16: The data image reduction process.

3.5.1 Analysis area

A subsection of the CCD was selected for processing by visually inspecting the image taken of the Spectralon standard with the analyzer in the optical path. This was performed for each observation geometry. A rectangular area within the illuminated portion of the image was selected that appeared to be uniform. The size of the area was manually selected to ensure it was as large as possible while remaining relatively uniform in intensity. Its location on the CCD was spatially defined by the corner pixel addresses. As the CCD was not moved for each geometry arrangement and great care was taken to prevent it from being disturbed from its position at the start of each set of images, this rectangular area represented the same area of the CCD for all samples and images taken at that observation geometry. Of note, by keeping this analysis area constant for all images, error caused by pixel-to-pixel variations in the imaging system were removed across the sample set. Figure 3.17 gives an illustration of an analysis subsection.

The illuminated area of the samples was approximately 2cm x 2cm at the acute illumination angles, and increased to approximately 6cm x 2cm at the

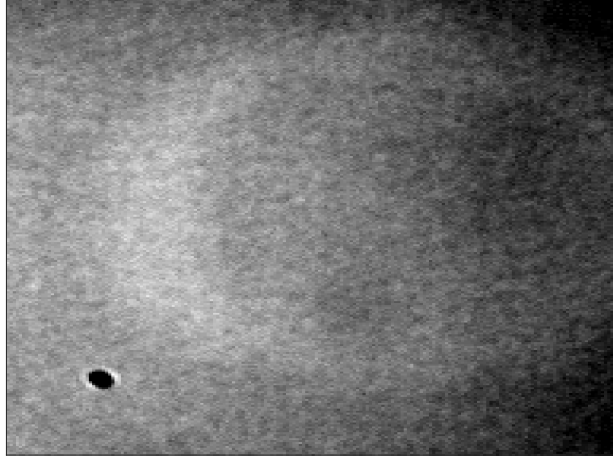


Figure 3.17: Analysis area of the Azur TJPV seen in Figure 3.9. This area is 192 x 232 pixels in size. The same dust feature and large circular patterns can be seen as in Figure 3.9.

obtuse illumination angles.

All images for the observation arrangement were then sub-sectioned in Matlab to the area that corresponded to this rectangular area of the CCD. This area was also used to retrieve the corresponding data from the master dark, bias and flat images.

3.5.2 Stokes parameter retrieval

Once the data images have had the dark, bias and flat corrections applied, they can then be arranged to achieve images containing the Stokes parameters. This is done by forming the relations given by:

$$\begin{bmatrix} I \\ Q \\ U \end{bmatrix} = \begin{bmatrix} I_0 + I_{90} \\ I_0 - I_{90} \\ I_{45} - I_{135} \end{bmatrix} \quad (3.2)$$

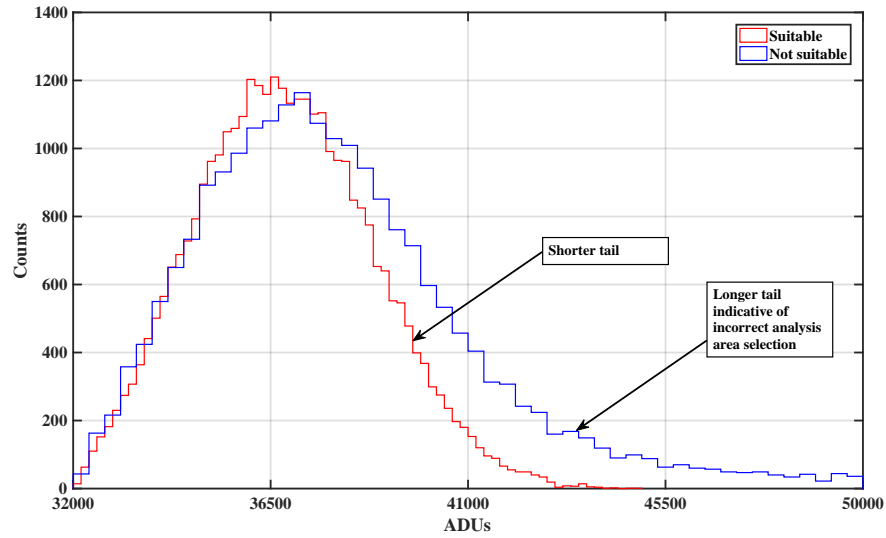
These operations are performed for each pixel resulting in images containing spatial representations of the Stokes parameters. The final operation is to then divide each parameter by the I image to arrive at the normalized Stokes parameters.

3.5.3 Polarisation retrieval

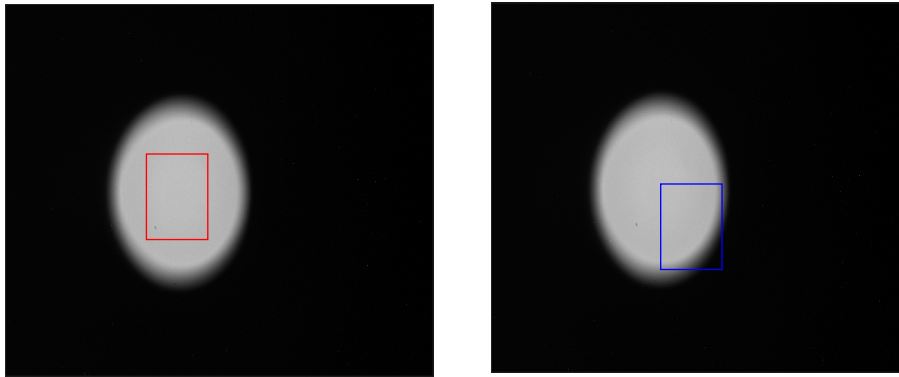
The DOLP and AOP are computed from the normalized Stokes parameter images through the use of Equations 1.30 and 1.35 respectively, as seen in Section 1.3.

The normalized Stokes parameter images were used to produce images containing the DOLP and AOP, from which the median values for each sample and observational geometry were plotted. Qualitative assessment of the sample surface inhomogeneity was performed by producing a histogram of the results. Figure 3.18(a) contains two histograms of DOLP data. One illustrates an acceptable normal distribution of values, and the other a distribution indicating an incorrect selection of analysis area. The image used to produce the histograms is shown in Figure 3.18(b) with the two analysis area selections shown.

This process formed a simple feedback loop for assessing the selection of the sub-image region. If significant features existed outside the main distribution of values on the histogram it was assumed that the analysis subsection included unwanted areas of the CCD (e.g., outside the analyzer), or areas of the sample illuminated differently. The data reduction process was re-run in these instances.



(a) Histograms



(b) Images.

Figure 3.18: Example of the analysis area selection assessment and feedback. The red and blue rectangles are the areas used to produce the histograms in Figure 3.18(a).

4 Results

This chapter provides an overview of the laboratory results obtained from the experiment. The data were organized and plotted in order to demonstrate that the experiment was able to measure systematic changes in the polarimetric behavior of light. This was accomplished showing trends in the DOLP and AOP of the samples with regard to the angle of the incident light (θ_i), the angle of observation (θ_{obs}) and the total reflected intensity given by the I Stokes parameter. All data were acquired and reduced to instrumental values, and as the absolute response of the light metering system and polarimeter in general were not established, understanding the sample responses can only be done comparatively. As the quantitative data was uncalibrated, only qualitative and comparative trend results are presented, with the acquired polarimeter response to the Spectralon taken as the comparative measure. Had the polarimeter been calibrated, the DOLP and AOP calculations could form a quantitative component to the body of results. However, the premise of the work is satisfied by providing qualitative analysis only.

The raw data were processed and stored as images (arrays) of spatially-dependent values of I , q and u of equal size. The median pixel value of the array was used when determining and plotting the results. The use of the median value to represent the larger image is appropriate as it removes the influence of outlier data resulting from sample surface and imaging system inhomogeneities. As the samples were removed and replaced for each observation geometry, their position within the sample holder was judged by eye with the aim of illuminating the same area of the sample for each geometry. To mitigate this as a possible source of error, especially for the samples with a poorer surface homogeneity, the flat-fielding process was applied and the median value used for the calculations. These considerations were covered in Chapter 3.

The observed general trends of the results are described with example

cases used to illustrate particular phenomena where appropriate. The full set of data and constructed visualizations are not presented in this chapter, but are presented in Appendix C. An illustration of the integration times used to acquire the data images is also presented.

4.1 Spectralon standard plate

Data illustrating the performance of the laboratory polarimeter while analyzing Spectralon are presented in Figure 4.1. DOLP, AOP and total intensity are plotted as a function of observation angle (θ_{obs}).

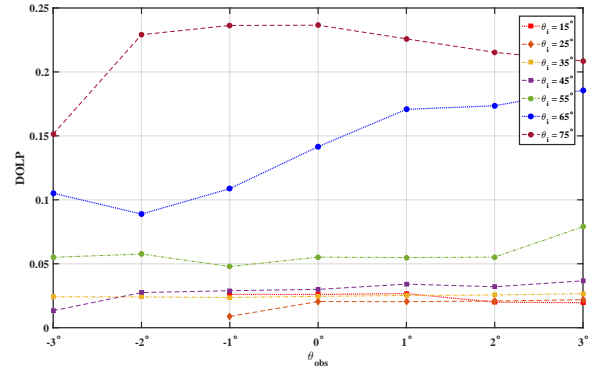
As explained in Section 2.4.1, Spectralon does not behave as a perfectly Lambertian surface, where a perfect Lambertian surface will exhibit a constant intensity of reflection regardless of observation angle. The non-Lambertian nature of Spectralon is especially evident for angles of illumination greater than 60° . To illustrate this, the AOP and DOLP from all observation angles was plotted with respect to the illumination angle (θ_i) on the same plot as the total intensity flux. The DOLP versus total intensity is at Figure 4.2(a) and the AOP versus total intensity at Figure 4.2(b).

These plots suggest that the trends in both the DOLP and AOP as θ_i changes are independent of the trend seen in the total flux. Generally, the DOLP tends to increase as the angle of incidence increases, whereas the AOP tends to remain centered on 0° except for the observations taken at $\theta_i = 75^\circ$.

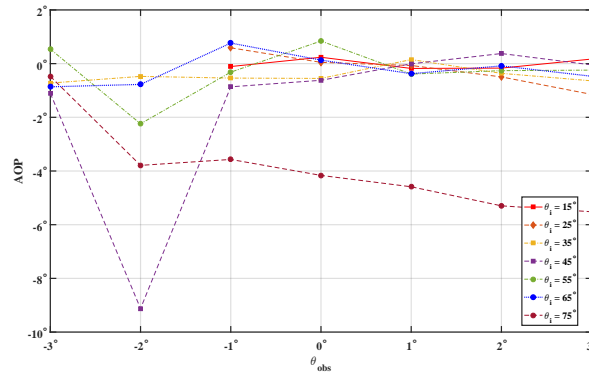
The apparent outlier data point seen in Figure 4.2(b) at $\theta_i = 45^\circ$ corresponds to the $\theta_{obs} = -2^\circ$ observation direction. The reason for its apparent inconsistency with the remainder of the data-set was not determined, however similar outlier data points at the same illumination and observation geometries for the other samples are not observed. There also appeared to be a trend in the $\theta_i = 75^\circ$ illumination geometry data, with the AOP values being recognizably more negative across the observational range compared to the other illumination geometries.

The DOLP and AOP can also be represented as three dimensional plots where θ_i and θ_{obs} are presented on the X and Y axes respectively, and the magnitudes shown on the Z axis. The DOLP and AOP are shown as such in Figures 4.3(a) and 4.3(b) respectively, with the total flux shown for reference at Figure 4.3(c).

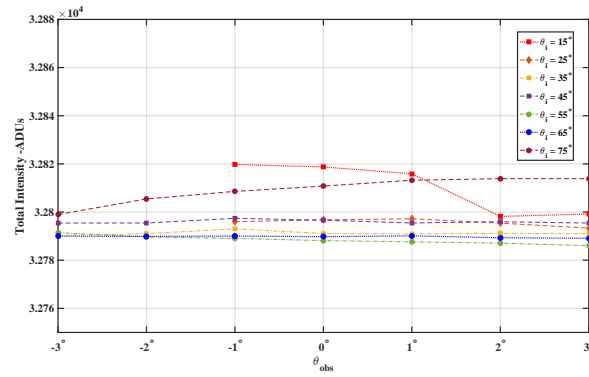
4.1. Spectralon standard plate



(a) DOLP

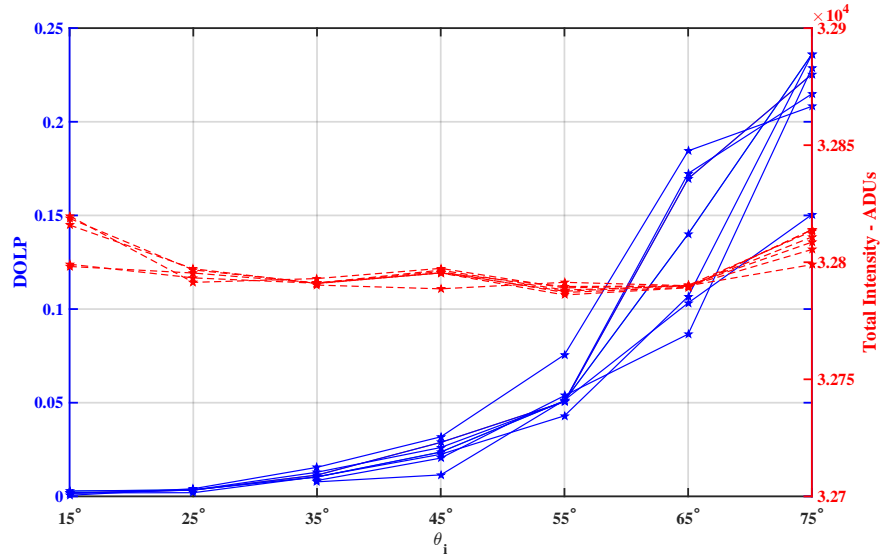


(b) AOP

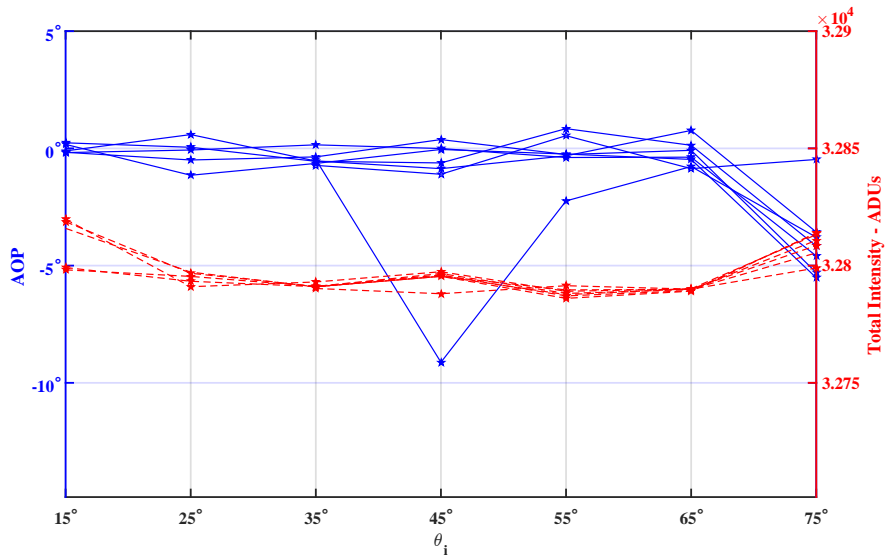


(c) Total Intensity

Figure 4.1: Spectralon DOLP, AOP and total intensity as a function of observation angle (θ_{obs}).



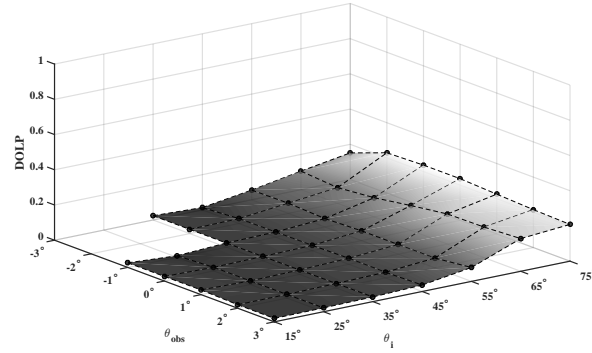
(a) DOLP



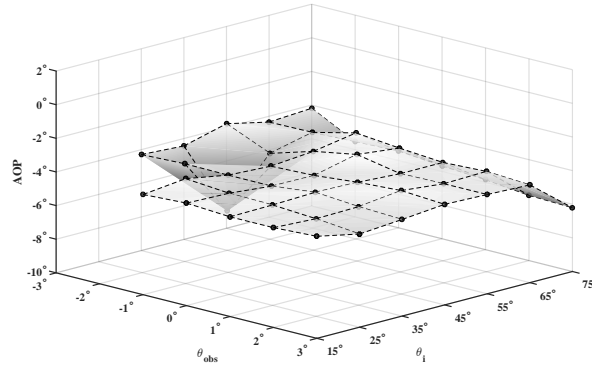
(b) AOP

Figure 4.2: DOLP and AOP as a function of incident light angle (θ_i), compared to the total intensity (I). The DOLP and AOP values are presented as solid lines, and the I values are the broken lines.

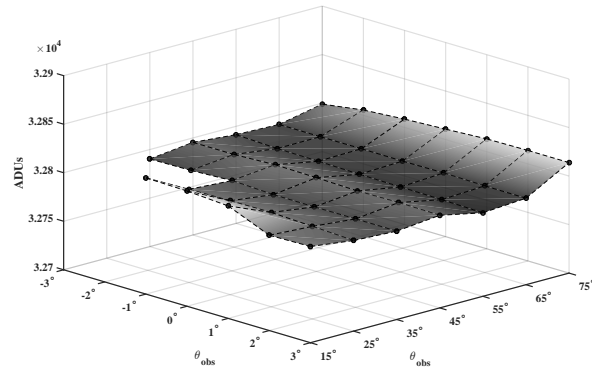
As predicted by Svensen *et al.*, Spectralon did not exhibit Lambertian polarimetric characteristics throughout the experimental sampling range. However, instrumental response to the Spectralon reflectance standard appeared to indicate a level of coherency for the DOLP, AOP and total intensity across the data acquisition geometries.



(a) DOLP



(b) AOP



(c) Total intensity

Figure 4.3: DOLP, AOP and total intensity (I) of the Spectralon sample as a function of incident light angle (θ_i) and observation angle (θ_{obs}).

4.2 Polarimeter analysis

While the aim of the thesis was to qualitatively investigate the ability to determine polarisation trends, a simple understanding of the quantitative performance of the polarimeter is presented. This work was completed to provide weight to the experimental results based on an independent and external assessment of the polarimetric nature of Spectralon. It should be noted that rigorous metrics on the performance of the polarimeter, light source, sample surface conditions and laboratory environment were not captured. Ideally, these tasks should have been completed but were deemed unachievable within the time constraints allowed. None the less, the resulting uncalibrated quantitative data are able to be interpreted qualitatively.

Notwithstanding, two simple tasks were completed to understand the veracity of the results. Firstly, the calculated DOLP of Spectralon as presented in Section 4.1 was compared against that provided by a modeled polarimetric response of Spectralon. Secondly, 70 additional individual DOLP calculations were performed for the Spectralon sample, each using separate raw data images. The results of these calculations illustrate the reproducibility of the data reduction and Stokes parameter calculations. Lastly, a brief discussion of error and uncertainty is presented.

4.2.1 Model comparison

In order to illustrate a basic level of polarimeter quantitative performance, an empirical model of the polarimetric characteristics of Spectralon was employed. Svensen *et al.*[43] performed a laboratory polarimetric characterization of Spectralon that resulted in the development of an empirical model of the Mueller matrix of Spectralon. Reflection intensity measurements were made every 2.5° from -90° to $+90^\circ$ reference to the normal of the Spectralon sample using illumination light with a wavelength of 532 nm. The illumination angles used were 0° , 30° , 45° and 60° . This model required only illumination and observation angle inputs to obtain a unique Mueller matrix for each observation geometry. The matrix was then used to estimate the Stokes vector of the light reflected from Spectralon. The stated error in the model is less than 3%. By employing a process of Mueller calculus using the model matrix, an estimation of the polarisation characteristics of light reflected from Spectralon was calculated.

To take advantage of the Spectralon model, an implementation of an ide-

alized polarimeter in Matlab was produced. The implementation is described by:

$$\mathbf{S}_{out} = \mathbf{M}_{spec} \cdot \mathbf{S}_{in} \quad (4.1)$$

where \mathbf{S}_{in} is the Stokes vector for unpolarised light, \mathbf{M}_{spec} is the Mueller matrix output of the empirical model and \mathbf{S}_{out} is the Stokes vector of the reflected light. Svensen *et al.*[43] should be consulted for a more thorough explanation of the model, however \mathbf{M}_{spec} in its expanded form is:

$$\mathbf{M}_{spec} = \begin{bmatrix} 1 & -(pK_2 + K_4) & 0 & -K_4 \\ -\left(pK_2 - \left(\frac{K_4}{2}\right)\right) & p_2 + K_4 & -pK_2^2 & pK_2K_3 \\ -K_5 & -pK_2^2 & p^2 - K_4 & pK_2 \\ 0 & -pK_2K_3 & -pK_2 & p^2K_1 \end{bmatrix} \quad (4.2)$$

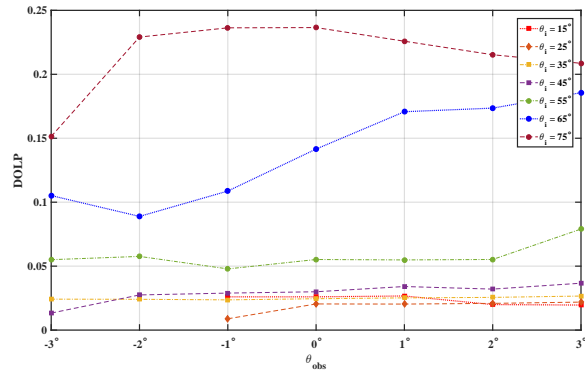
where:

$$p = \left| \frac{(\theta_{obs} + \theta_i)^3}{22} \right| \quad (4.3)$$

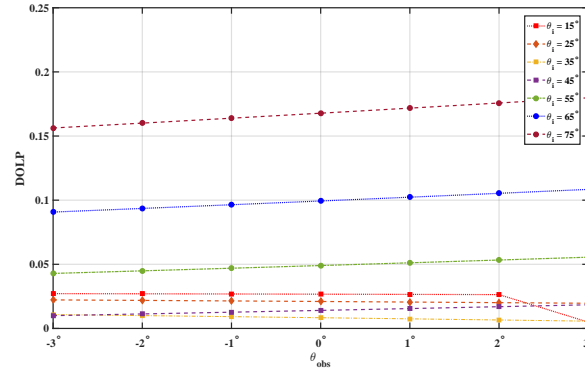
and the K values are coefficients were found by applying a process of best fit to the measured results. The values of K are provided by Svensen *et al.* as: $K_1 = 0.67$, $K_2 = 0.17$, $K_3 = 0.45$, $K_4 = 0.04$ and $K_5 = 0.03$.

This model enabled the introduction of θ_i and θ_{obs} values, defined with respect to the normal of the Spectralon surface, to produce a $\text{DOLP}(\theta_i, \theta_{obs})$ figure. The modeled DOLP, experimental DOLP and the magnitude of the difference between them are illustrated in Figure 4.4.

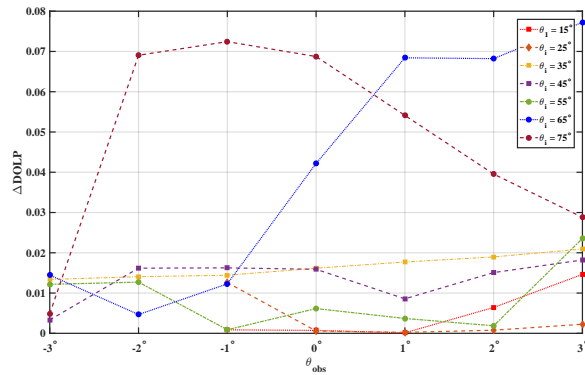
A general observation can be made from Figure 4.4 that suggests the polarimeter is able to detect trends in polarisation across a range of illumination angles. Specifically, as the angle of illumination increases, so does the magnitude of the degree of linear polarisation. This concurs with the modeled behavior of Spectralon. Figure 4.4(c) illustrates that the difference between the calculated and modeled DOLP for all illumination and observation angles. It can be seen that the difference between the experimental and modeled results was less than 2% except for the $\theta_i = 65^\circ$ and 75° datasets. While this may suggest a fault of the polarimeter, the authors of the empirical model state that significant deviations in behavior occur for large illumination and observation angles.



(a) Experimental DOLP.



(b) Modeled DOLP.



(c) Magnitude difference between modeled and experimental DOLP.

Figure 4.4: DOLP for Spectralon calculated from the experiment and an empirical model.

The model provided confidence that the data reduction process used to arrive at the Stokes parameters was valid. Additionally, while the polarimeter was not rigorously characterized, the model provided confirmation that it was able to detect polarisation trend information with respect to illumination and observation geometry.

4.2.2 Data replication

In an ideal case each sample would have been measured numerous times in order to arrive at values for uncertainty and to demonstrate experimental repeatability. Due to the time restraints and the manual nature of the polarimeter, only the Spectralon was sampled numerous times at each observations. Consequently, the repeatability of the data was assessed by performing the data reduction and DOLP calculation for the Spectralon sample 10 times at the specular observation direction for all illumination geometries. Seventy individual calculations were performed using a combined total of 240 separately collected images of Spectralon across a range of illumination and observation geometries. Each calculation used different raw data images and the same data reduction process. These images were acquired over a number of days, at different times of the day and after differing periods of polarimeter and light source operation.

By doing so, the influence of sources of stray light, variance in the light source due to changes in temperature, differences in the area of sample illumination and CCD operating times would be captured. The images used for each set of 10 calculations took on average 5 minutes to acquire, with the Spectralon sample being removed from the sample holder after a set of images were acquired, and replaced for the next. Additionally, the area of the CCD used to capture data was different for each set of images.

The output of the data reduction process was spatially dependent arrays of the calculated values. The median of each array was found as was the standard deviation (σ). The median DOLP with error bars set at 1σ above and below the data-point for each of the ten images across each of the observation geometries were plotted and is included at Figure 4.5. While the X axis provides the calculation number, it could also be considered analogous to time slices within the data collecting process. As stated, each set of data images for each of the illumination geometries took approximately 5 minutes to acquire, therefore the X axis in this figure can represent different times of data collection. This allows the calculated DOLP at each time slice to be

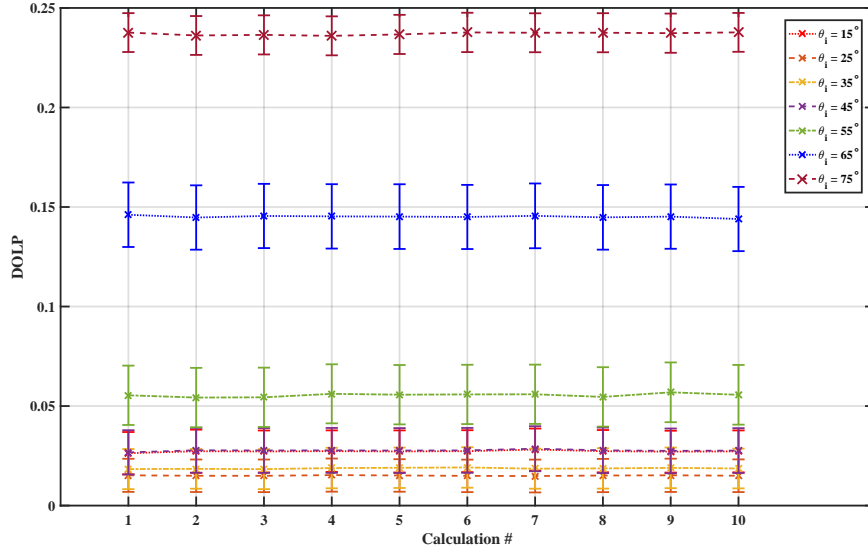


Figure 4.5: DOLP with error bars set at 1σ for 10 individual DOLP calculations. The raw data images were taken at a variety of times of the day and after varying times of source light and CCD operation.

influenced by the time-variant nature of the experimental errors impacting the data collection process. That is, if a systematic error was present with a time-variance less than the time taken to perform data collection for each geometry, it would be illustrated within Figure 4.5.

The maximum σ calculated across the illumination geometries was at the $\theta_i = 65^\circ$ geometry with a value of approximately 1.65%. This value was consistent across the 10 test calculations. The smallest σ value was achieved at the $\theta_i = 25^\circ$ geometry for a value of approximately 0.008%.

Figure 4.5 illustrates a level of repeatability across the data collection and reduction process for the Spectralon sample. There are no obvious increasing or decreasing trends within each geometry data-set, with all geometries exhibiting a similar level of constancy. This suggests that sources of error do not vary over a time period less than that required to acquire the raw data images. The differences in DOLP between illumination angles was expected, as discussed in Section 4.2.1. The data used were collected at various times of the day under controlled, but still slightly varying lighting conditions. The light source and CCD had been operating for varying amounts of time at the

time the images were collected.

While this analysis used only the Spectralon, it should be noted that the apparatus was not touched aside from changing the sample for each observation geometry. These observations suggest that the experiment achieved an acceptable level of repeatability within each illumination geometry data-set. Future work should aim to repeat this process for all samples, with a more automated experiment and polarimeter being a key enabler.

4.2.3 Error and uncertainty estimation

An absolute error estimation for the calculated values of DOLP and AOP was not made. As the polarimeter and its constituent optics were not rigorously characterized, their influence on systemic error are not quantified. Misalignment of the CCD/lens pairing, polarimetric characteristics of the multi-optical component lens, and the spectral response and polaroid defect of the analyzer, all forms of instrumental error that could lead to cross-talk in the Stokes parameters, are acknowledged as sources of error. Further, unwanted light pollution within the laboratory environment varied with the time of day. As the experiment was conducted over numerous days at different times of the day, this stray light also contributed to error.

However, as sources of error were constant for the polarimeter for each observation geometry and sample, the results presented are still valid to make comparative and trend observations. It is suggested as a further task that the experiment be at least partially repeated with a different lens, CCD and analyzing polaroid arrangement to gain a more thorough appreciation of the magnitude of uncertainty in the individual sample DOLP and AOP calculations. This should include analysis of uncertainty in the integration times used, especially for those of approaching the manipulation time of the shutter mechanism of the CCD. This could be completed in concert with a polarimeter characterization campaign.

4.3 Integration time

The raw image intensities were normalized to one second integration times within the data reduction process for ease of comparison. The integration times used to acquire the images were not necessarily constrained to one second however with the goal ADU count of 18000 able to be reached with longer

or shorter exposures as discussed in Section 3.2.4. The normalization was performed by dividing the value of each pixel by the exposure time of the image. This technique assumed that the data images were acquired within the linear operating range of the CCD; a constraint managed through imposing the ADU count goal, and monitoring of the signal to noise ratio of the images. The exposure time for each image was automatically accessed within the data reduction process by examining the header information contained within each image file.

Plots providing examples of the integration times used to acquire the images are shown at Figure 4.6. The integration times presented are representative in magnitude of those used throughout the experiment.

While the times were selected via a simple test and evaluate process with a target of 18000 ADUs, it should be noted that four images of the time lengths shown in Figure 4.6(a) were required at each θ_i, θ_{obs} arrangement, corresponding to the four orientations of the analyzer. In addition to the integration time, a short time period was required for the linear analyzer to be rotated to the next position as described in Section 3.4. This time period was three seconds and was a result solely of the performance of the analyzer rotary stage.

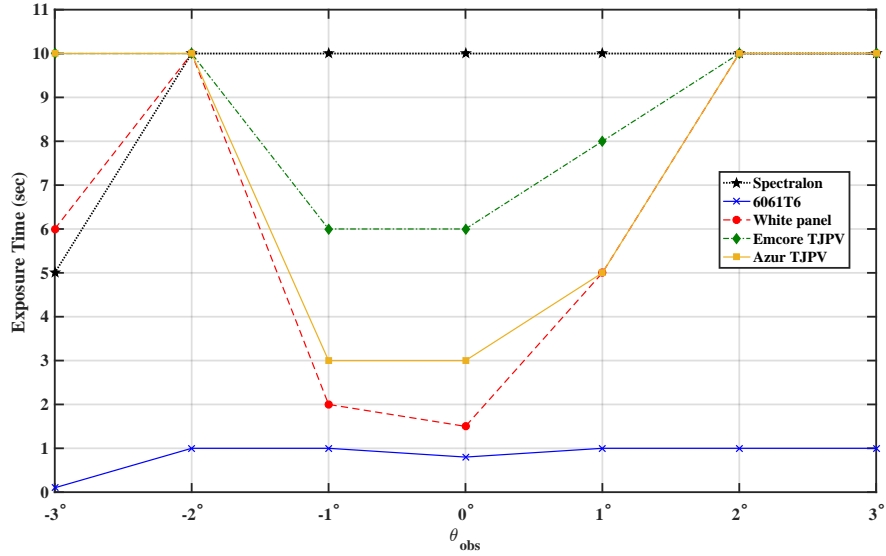
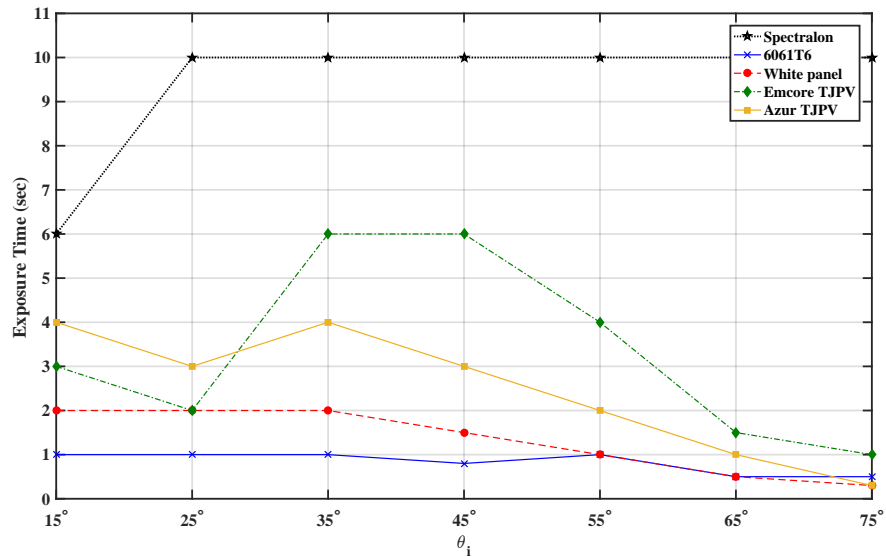
(a) $\theta_i = 45^\circ$ (b) $\theta_{obs} = 0^\circ$

Figure 4.6: Example integration times for all samples. Sub-figure 4.6(a) illustrates all observation locations at $\theta_i = 45^\circ$, and Sub-figure 4.6(b) illustrates the measurements at the specular direction for all θ_i .

4.4 General results

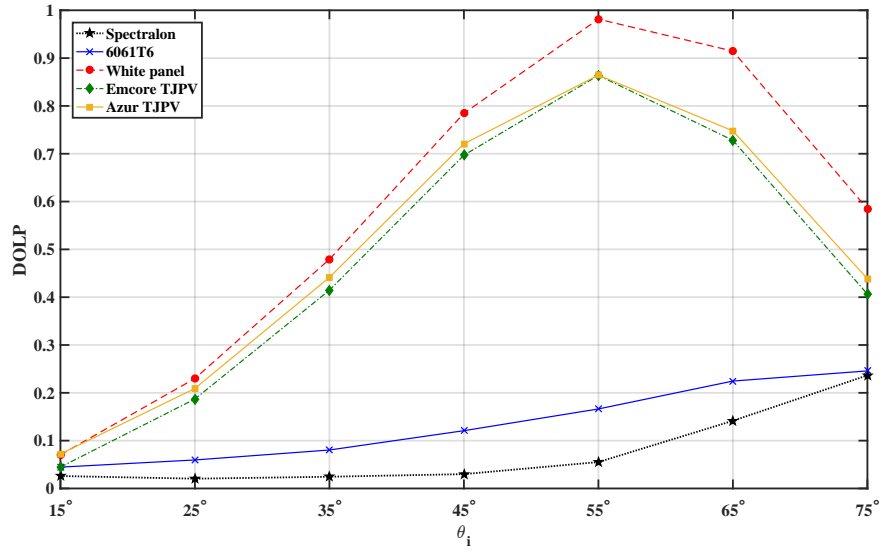
The overall results of the experiment are best illustrated through the DOLP and AOP as calculated at the specular reflection observation point for each material. These results are presented in Figures 4.7(a) and 4.7(b) respectively.

The samples exhibited different DOLP values for the range of tested illumination angles, with the less diffuse materials exhibiting more rapid changes and higher overall degrees of polarisation. The painted panel and two solar cells reached a maximum DOLP when the angle of illumination was 55° , while the DOLP of the 6061-T6 aluminum and Spectralon appear to gradually increase as θ_i increases. All samples appeared to show less difference in AOP as θ_i increased from 15° , while maintaining a trend towards a value of approximately 0° . Compared to Spectralon, the DOLP for the samples appeared to be the more readily discernible characteristic than the AOP, especially for the less diffuse materials.

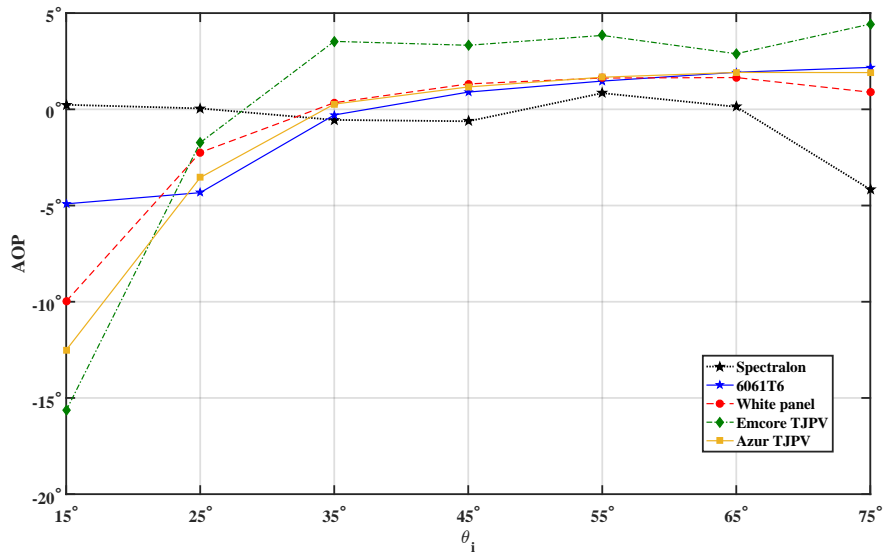
The DOLP and AOP data were compared against each individual sample's total intensity over all acquired observation points. Figure 4.8 and 4.9 provide examples of this showing the DOLP and total intensity at the specular observation direction for the four material samples. The Spectralon response data seen in Figure 4.2(a) are included for comparative purposes.

While the profiles of the DOLP for the more specular samples appears quite similar in magnitude with respect to the illumination angle, particularly those of the two TJPV cells, the trends of the total flux for these samples remains identifiably different especially when compared to the Spectralon data. These plots also illustrate the apparent independence in the trends of DOLP from the total reflected flux of the samples for the non-diffuse samples. That is, while the total flux increases with increasing θ_i , the DOLP appears to more rapidly increase to an observed maximum at $\theta_i = 55^\circ$ and then begins to decrease. The aluminum sample does not behave in this manner however, appearing to act much more like the Spectralon in terms of DOLP.

Each sample had three, three-dimensional plots constructed as was produced for Spectralon at Figure 4.3. These are presented to illustrate the changes in DOLP, AOP and I across both θ_i and θ_{obs} . Two dimensional plots showing the DOLP and AOP as functions of both θ_i and θ_{obs} for each of the samples are provided in Annex C.

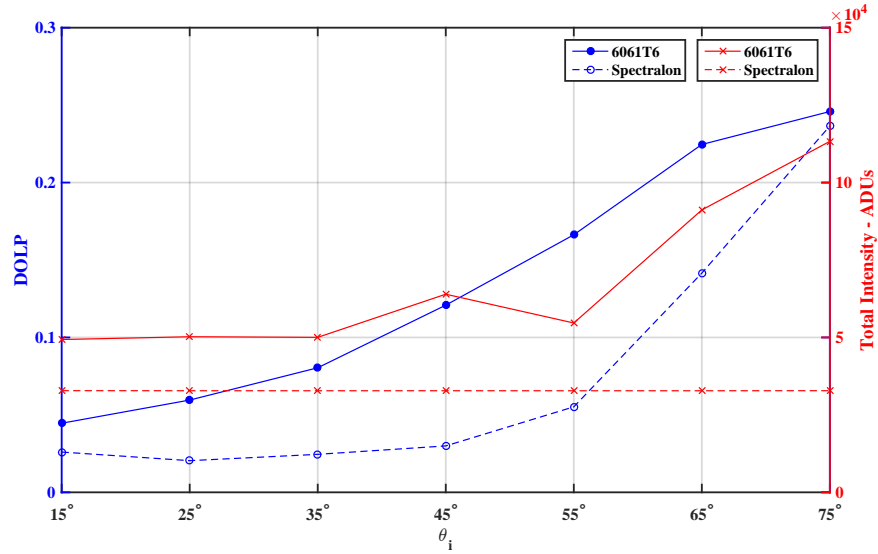


(a) DOLP

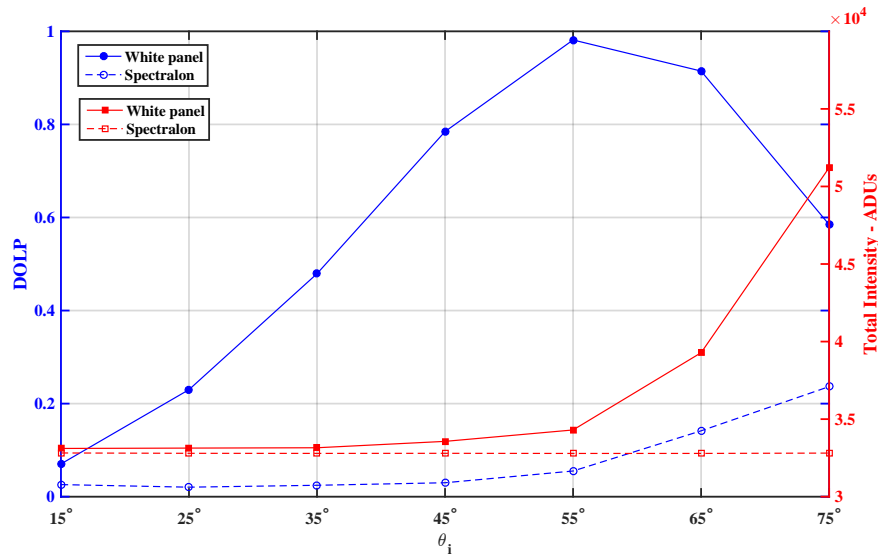


(b) AOP

Figure 4.7: DOLP and AOP for each material as a function of incident light angle (θ_i), calculated at the specular reflection direction.

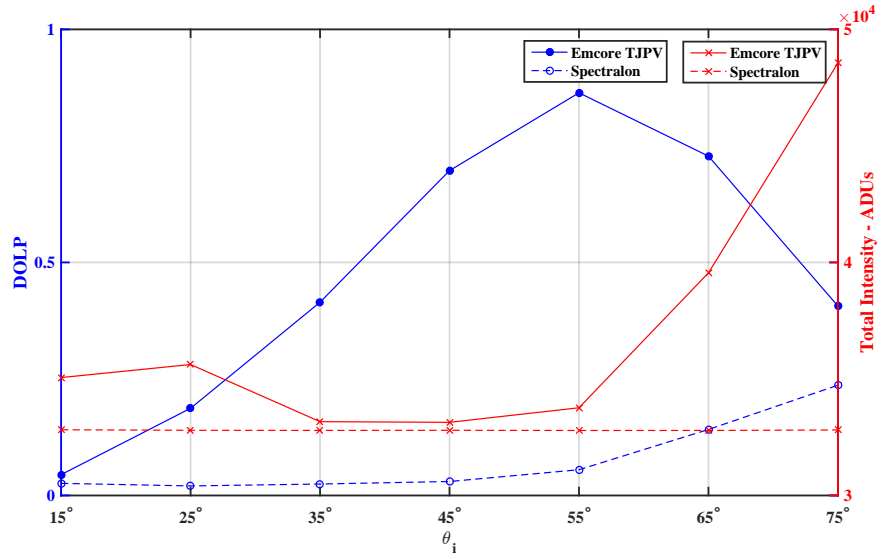


(a) Aluminum

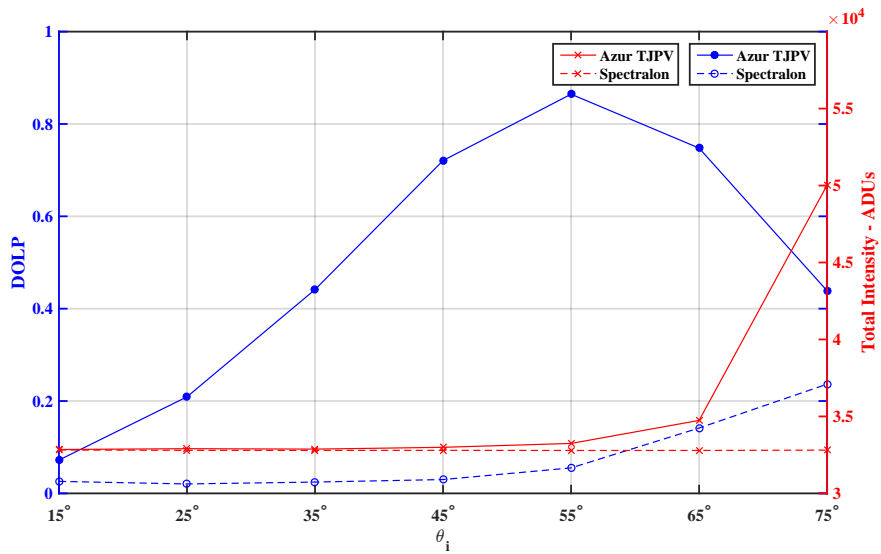


(b) White panel

Figure 4.8: DOLP v total intensity at the specular observation direction for the 6061T6 aluminium and white panel. The solid lines provide the values of the sample, and the broken lines for the Spectralon.



(a) Emcore TJPV cell



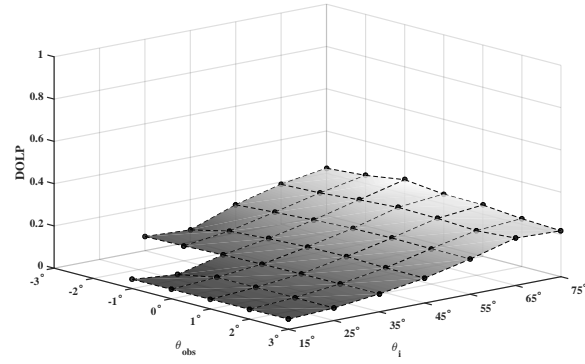
(b) Azur TJPV cell

Figure 4.9: DOLP v total intensity at the specular observation direction for the Emcore and Azur TJPV cells.

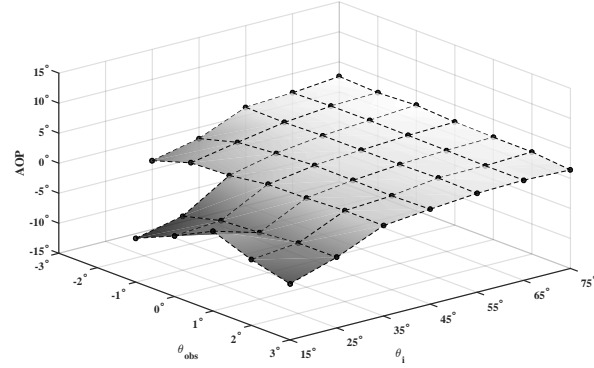
4.4.1 6061-T6 Aluminum

The aluminum sample exhibited trends in both DOLP and AOP with respect to geometry that were similar to Spectralon in behavior, but with recognisable differences in magnitude for both DOLP and AOP. As would be expected for a more diffusely reflective surface, the total intensity remained relatively constant throughout the illumination and observational range. A recognizable increase in DOLP towards larger θ_i values was seen however. The DOLP results appeared especially similar to those produced by the Spectralon. It is noted that the surface topology of the sample was dominated by machining marks that were orientated at 90° to the plane of observation. It is postulated that the effect of this was to degrade an obvious Brewster's angle effect thereby reducing any noticeable peak in the DOLP, especially when compared to the TJPV cell samples.

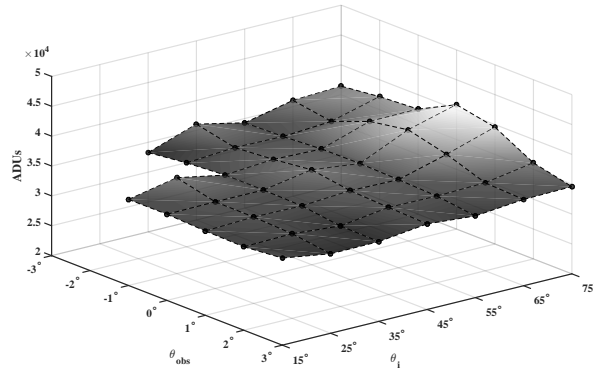
The AOP appeared to vary in much the same way as the Spectralon with the more acute θ_i values displaying greater variation. The decreasing feature in the AOP for Spectralon at $\theta_i = 75^\circ$ was not seen with the aluminum sample.



(a) DOLP



(b) AOP



(c) Total intensity

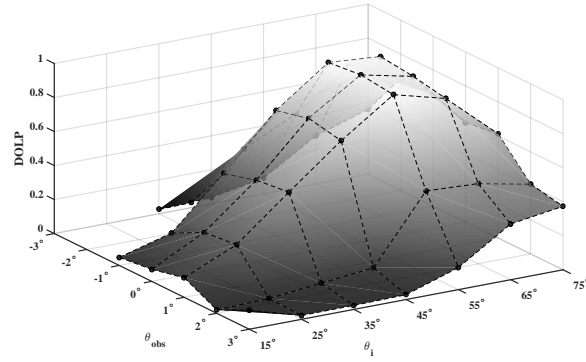
Figure 4.10: DOLP, AOP and total intensity (I) of the aluminum sample as a function of incident light angle (θ_i) and observation angle (θ_{obs}).

4.4.2 White-painted panel

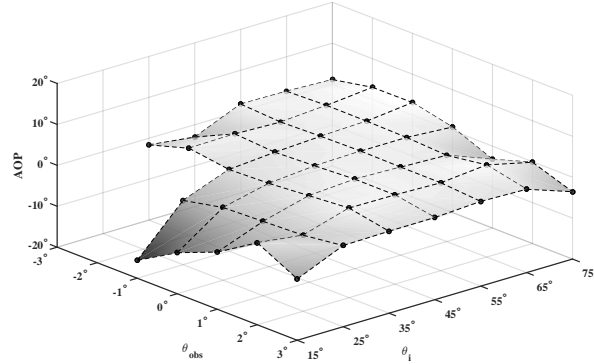
The white-painted panel exhibited significantly different profiles from the Spectralon for the DOLP and total flux as expected. The AOP appeared to vary across the range of data in generally the same fashion as both Spectralon and aluminum, but with different magnitudes of change. The smaller θ_i values appeared to result in a greater range of AOP values across the observational range, with a constant trend appearing to exist from $\theta_i = 35^\circ$ up to 75° . This trend appeared to center or settle about an AOP value of 3° .

The DOLP showed a specific trend towards a maximum value at $\theta_i = 55^\circ$, with the off-specular observation points also following this trend. The DOLP appeared to change quite rapidly with changes to both θ_i and θ_{obs} .

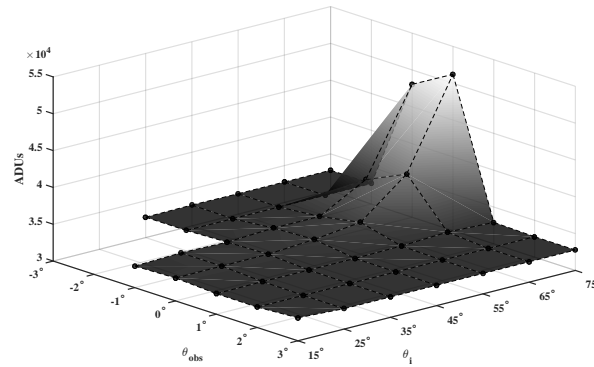
No specific correlation was seen to exist between the AOP with either the DOLP or total flux trends.



(a) DOLP



(b) AOP



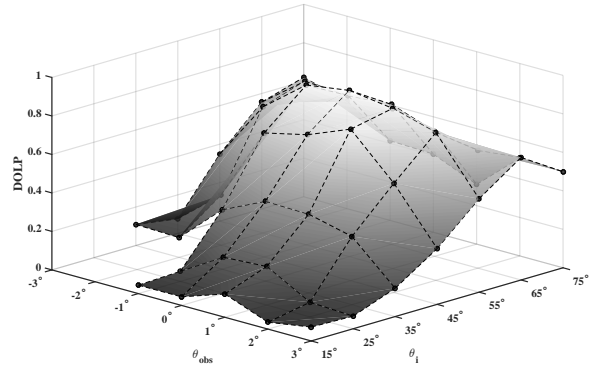
(c) Total intensity

Figure 4.11: DOLP, AOP and total intensity (I) of the white-painted panel sample as a function of incident light angle (θ_i) and observation angle (θ_{obs}).

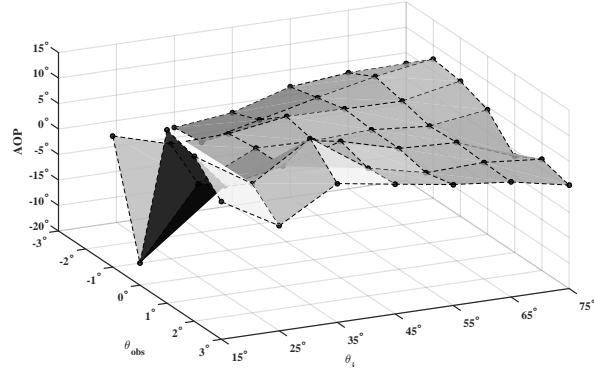
4.4.3 Emcore TJPV cell

The Emcore TJPV cell followed the basic trends displayed by the painted panel. The AOP exhibited a trend towards 3° as θ_i increased, with little variation with respect to θ_{obs} . The most obvious feature was the large change as θ_{obs} changed in the $\theta_i = 15^\circ$ data-set. This was also a feature of the white panel and aluminum. No obvious correlation existed between the AOP and DOLP or total flux.

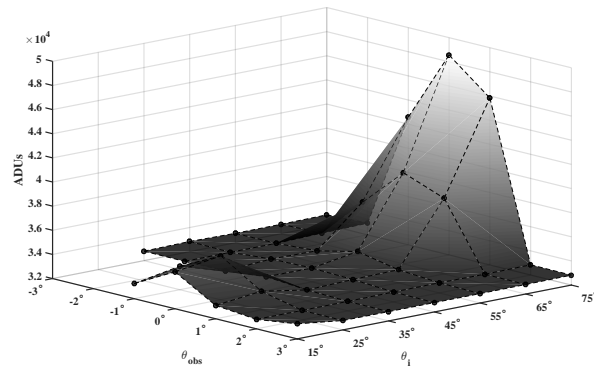
The maximum DOLP was reached at $\theta_i = 55^\circ$, but was not the same magnitude as the white panel.



(a) DOLP



(b) AOP



(c) Total intensity

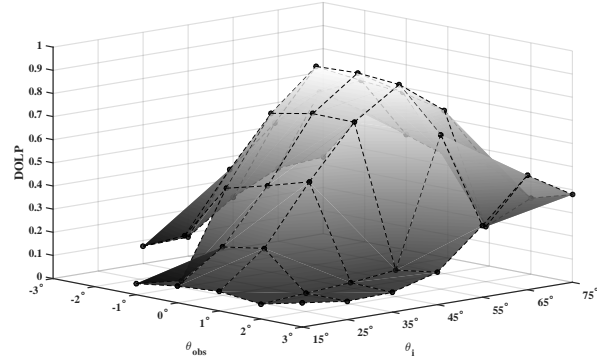
Figure 4.12: DOLP, AOP and total intensity (I) of the Emcore TJPV cell sample as a function of incident light angle (θ_i) and observation angle (θ_{obs}).

4.4.4 Azur TJPV cell

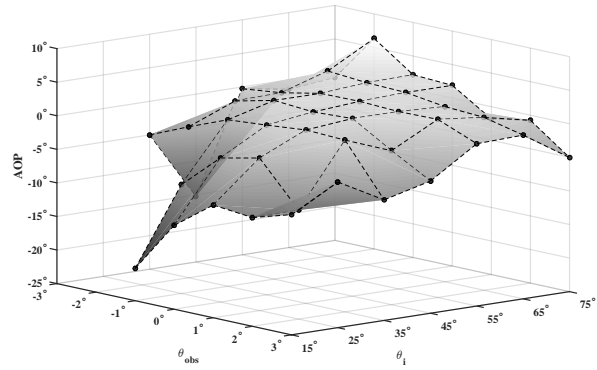
The Azur TJPV cell displayed characteristics very similar to both the white painted panel and Emcore cell. The DOLP appeared to reach a maximum at the specular observation direction with an incident light angle of 55° . The DOLP changed quite rapidly with both θ_i and θ_{obs} although the changes, and maximum, appeared to be less than that of the white panel but very similar to the Emcore cell.

The basic trends in the AOP data appeared to follow those seen amongst all the samples, with the greatest variation in values occurring when the light was incident at 15° . Again, a trend towards an AOP of about 3° is seen as the incident light angle became greater. This appeared to be the case regardless of the angle of observation.

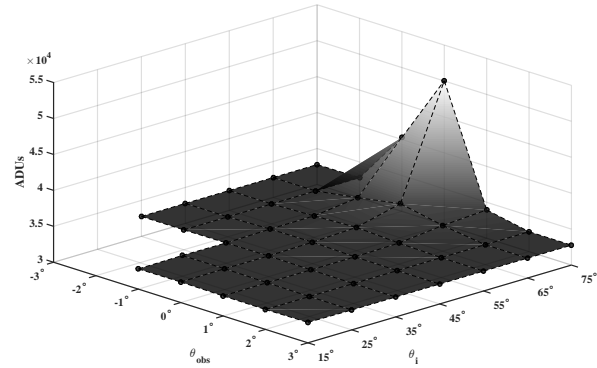
The total flux behavior also mimicked the white panel, with a maximum occurring at the specular observation direction and incident light angle of 75° .



(a) DOLP



(b) AOP



(c) Total intensity

Figure 4.13: DOLP, AOP and total intensity (I) of the Azur sample as a function of incident light angle (θ_i) and observation angle (θ_{obs}).

5 Discussion

This chapter discusses the results of the experiment aiming to present information useful for addressing the main premise of the thesis as presented in Chapter 1. This was to advance the application of passive, visible-wavelength polarimetric techniques to the challenges of space situational awareness, specifically through the use of common CCD and small aperture telescope equipment and techniques. The task was further focused through the literature review, with the experimental tasks posed in Chapter 2 providing additional specificity to the experimental work. For review, these were;

- to confirm that the relative degree and angle of linear polarisation for different materials can be determined in the laboratory environment,
- to determine whether the polarisation characteristics of the reflected light had an observational geometry dependency,
- to determine whether a passively-derived polarimetric response is able to distinguish between different spacecraft materials,
- to determine whether the polarimetric characteristics of light reflected from RSOs can be determined using equipment often used with small aperture telescopes,
- to determine whether the polarisation characteristics will have a dependency on the orientation of an RSO with respect to the light metering system, or is it possible to infer spacecraft orientation from a polarimetric response,
- to understand the whether the relative differences in polarimetric characteristics of reflections from common spacecraft materials to first order are sufficient to encourage or recommend further research,
- and to identify the utility, or otherwise, of polarimetry as a photometric SSA technique.

The experiment provided results sufficient to advance the understanding of these points, and ultimately enabled conclusions to be drawn about the main premise of this work. The trends observed in the angle and degree

of polarisation for each material confirm that further investigation into the utility of polarimetry as a complimentary technique in RSO characterization is appropriate.

5.1 Degree and angle of linear polarisation

The results illustrate the ability of the polarimeter and data reduction process to produce polarisation characteristic data for each sample. The degree and angle of polarisation data displayed similar trends for similar materials, providing a level of confidence that the polarimeter component parts, data collection and data reduction processes were appropriate. The experimental results were in general agreement with the overall result of similar experiments such as that conducted by Culp *et al.* [8], namely that materials having specular reflective properties could display a higher degree of linear polarisation. This added further confidence to the validity to the experimental process.

As the polarimeter used in the experiment was not calibrated or rigorously characterized against a known standard, the polarisation data retrieved from the samples was not considered absolute and was therefore unable to provide calibrated quantitative characterization of the samples. Notwithstanding, the experiment's results confirm the ability of a linear polariser and CCD camera to qualitatively ascertain polarisation properties of some common spacecraft materials, and suggest that quantitative analysis is also possible. These conclusions can coalesce with the conclusions of other experimenters using optical methods of spacecraft characterization such as Bédard [7]. Where broad-band photometry and spectrophotometry have displayed promise in materials identification, this experiment shows that passive polarimetric analysis can also aid in the differentiation between and identification of RSO surface materials.

For the primary aim, the experiment showed that using equipment and techniques commonly used by the SSRL, specifically the CCDs paired with small aperture telescopes, would be able to arrive at the polarimetric information required.

5.2 Integration times

The experiment illustrated particular idiosyncrasies that would impact the practical application of polarimetry for space object characterization.

The integration times used, especially for the less diffuse samples at the larger off-specular observation directions, were up to four times larger than at the specular direction as explained in Section 3.2.4. While this result was expected, it nevertheless leads to an untested hypothesis that in practice the time taken to acquire the four images necessary to produce the reduce Stokes vector could lead to data interpretation and reduction difficulties. Specifically, this problem would manifest as a degradation in the temporal resolution of the data being produced. Conversely, an attempt may be made to address this problem by using lower integration times leading to lower signal to noise ratios, or limiting the technique to brighter targets or even to smaller periods of useable observations over a night or season.

In any case, the degradation in temporal resolution of the polarimetric data would impact on the utility of the measurements. This would be the case particularly for RSOs with observer aspects or Sun-object-sensor geometries that have a rate of change with a period similar to the temporal resolution.

Incidentally, it could be suggested that this same problem would manifest itself in the active polarimetry and Mueller matrix decomposition processes reviewed in Chapter 2. As the active polarimetric and Mueller matrix decomposition requires 16 individual measurements, a similar problem with temporally accurate data extraction may result. This hypothesis was not tested within the work.

For illustrative purposes, the data contained within Figure 4.6(a) was re-plotted with the time required to obtain all necessary data images plus the time taken to rotate the analyzer (three seconds per rotation) plotted as a function of observation angle. This is seen in Figure 5.1.

To improve the temporal resolution of the polarimeter, two methods could be employed. The first is to improve the duty cycle of the analyzing element of the polarimeter, and the second to reduce the length of the exposures. As an illustration, the duty cycle of the analyzer can be calculated and plotted with respect to the total data acquisition process, with the duty cycle (DT) given by;

$$DT = \frac{4 \times IT}{4 \times IT + (\#Images - 1) \times AR} \times 100\% \quad (5.1)$$

where IT is the integration time, $\#Images$ is the number of data images required and AR is the time taken for the analyzer to rotate to the next

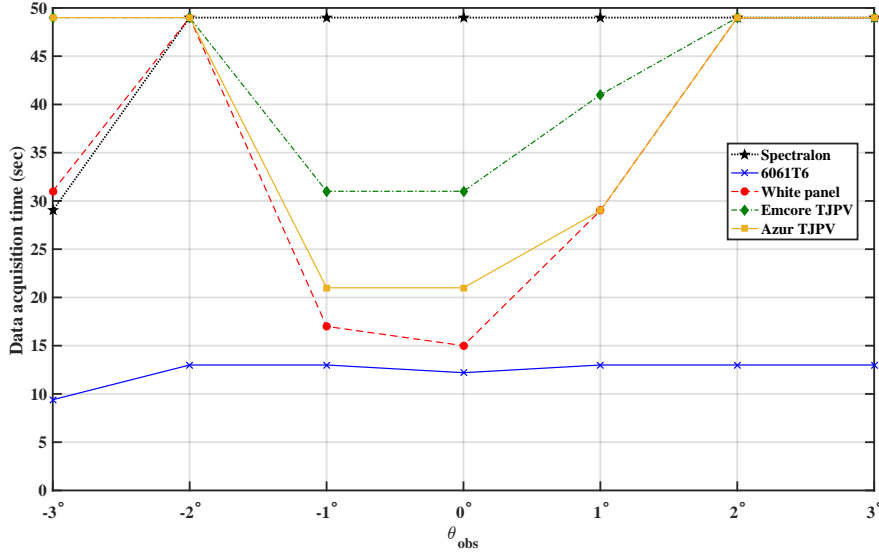


Figure 5.1: The total time required to acquire all data images necessary to produce one set of reduced Stokes vector calculations for the $\theta_i = 45^\circ$ illumination geometry.

position. An example is provided in Figure 5.2 which illustrates the duty cycle of the analyzer for the white painted panel at the $\theta_i = 45^\circ$ illumination geometry. It can be seen that the duty cycle of the analyzer ranges from 40% to 80%. For the aluminum sample, the duty cycle remained at approximately 30% as would be expected from the trends seen in the total flux seen in Figure 4.10(c).

This suggests an opportunity to improve analyzer efficiencies within the data acquisition process and hence improve the temporal resolution of the process.

A method of increasing the analyzer's duty cycle while maintaining an imaging polarimeter design would be to use a beam splitting polarising prism in place of the linear analyzer such as a Wollaston or Glan prism. This would enable the capture of two orthogonally polarised light beams simultaneously. This would allow the experimenter to arrive at a degree of linear polarisation value using only one integration period, and the calculation method similar to that employed by Culp *et al.* seen at Equation 2.5. This method removes the necessity to allow time for analyzer rotations but does not allow for the

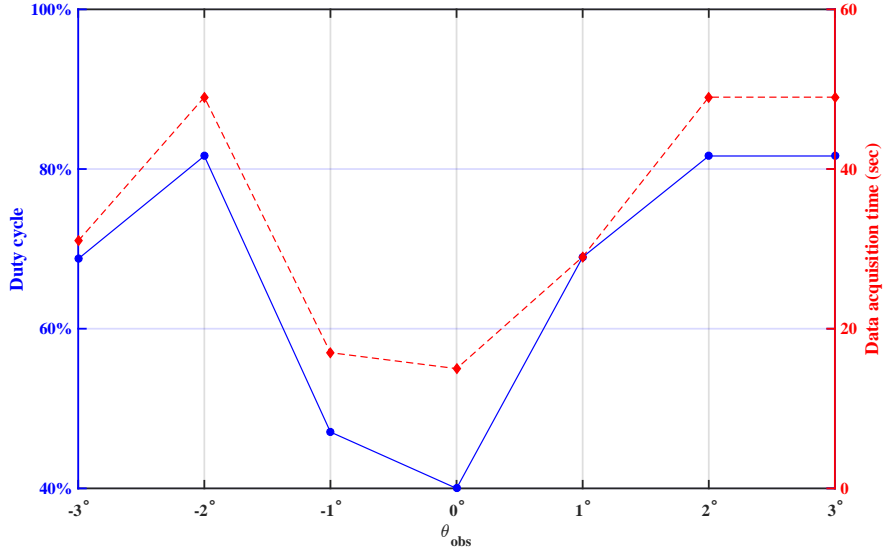


Figure 5.2: Duty cycle of the analyzer with respect to the total data acquisition time period for the white painted panel at the $\theta_i = 45^\circ$ illumination geometry.

recovery of the Stokes parameters.

The addition of a rotatable half wave phase retarder in front of the polarising beam splitting prism would also allow the full capture of the q and u Stokes parameters. This would take advantage of the increased duty cycle through a reduction in the number of rotations required while maintaining the imaging nature of the device. This second method would include an added level of data reduction complexity.

Another method of improving the temporal resolution of a polarimeter for RSO characterization would be to employ a retarder that rapidly modulates the orientation of the incoming polarisation ellipse, and an analyzing beam splitting prism. This concept has been employed before by others including Monin *et al.* [47], Bueno [48] and Ye [49]. A method of comparing the orthogonal polarisation signal outputs from the beam splitting prism can be arranged such that the amplitude of the signals of the two beams will correspond to the relative intensities of the orthogonal components of the polarisation. An additional half wave retarder could then be added with an appropriate fast axis offset to the first allowing the calculation of both the q , u and v param-

eters. This method represents many benefits, beyond the scope of this work, but would also require the use of photon counting devices as the light meter as opposed to an imager such as the CCD used in this experiment. In this arrangement the polarimeter would be restrained to analyzing one target at a time, removing its imaging capability.

5.3 Geometry dependency

Given the polarimeter and data processing was the same for each material, illumination and observation geometry, the differences in the instrumental polarimetric values calculated provide sufficient justification to conclude that the polarimeter was able to detect changes in the polarimetric characteristics of the reflected light. This was shown to be the case as the sample, observation and illumination geometries changed. This suggests that analysis of the polarimetric characteristics of light reflected from RSOs over time can aid in the understanding of the observer-RSO-Sun geometry, beyond a simple description of phase angle.

The experiment illustrated a level of dependency of the polarimetric characteristics of the reflected light on RSO aspect with respect to both the source of illumination and observer. While comprehensive *a priori* knowledge of the geometry and sample orientation was held, the results suggest an ability for polarimetric analysis to provide data on the long-term preference of a target object's aspect with respect to the observer and source of illumination. The ability of the technique to suggest instantaneous information was limited by integration times, as seen in Section 5.2.

As the experiment was conducted solely within the illumination-sample plane defined using the normal of the sample surface, the results do not allow conclusions to be made about the impact of moving the observer outside the plane. It is reasonable to suggest though, that moving the observer out of the plane of illumination may also affect the detected polarisation characteristics however.

As sample rotation with respect to the plane of observation/illumination was not introduced in the experiment, the results can not illustrate changes in polarimetric response with respect to sample rotation. A similar suggestion to that made about out of plane observations is made though, that sample rotation may also introduce changes in the polarisation of the reflected light.

5.4 Characteristics of different materials

Generally, the results showed that the samples exhibited polarimetric characteristics sufficient to be detected and differentiated. In particular, the samples that would be described as diffusely reflecting had identifiably different polarisation characteristic trends to those samples described as less diffusely reflecting. While this was the expected outcome, the experiment showed that the magnitude of the differences between the samples was sufficiently large to allow level of superficial differentiation.

The results of the degree and angle of polarisation of the two TJPV cells provide insight into the limitations of the method to enable individual material identification. The trends of both of these materials were quite similar as seen in Figure 4.7(a). The same plot also illustrates the dissimilarity between diffusely reflecting materials such as the Spectralon and the aluminum compared to the more directionally specularly reflective materials such as the TJPV cells and the white painted panel.

6 Conclusion

The task of characterizing resident space objects as a contributory effort in the wider space situational awareness mission is a demanding one. Various methods are employed. In the optical spectrum these methods include broadband photometry and spectro-photometry. This work focused on understanding the role passive optical polarimetry can play in RSO characterization.

This work explained and presented the results of an experiment that aimed to survey of the polarimetric characteristics of a small number of common spacecraft materials. The experiment utilised current and CCD device technology and data reduction methods to do this. The degree of linear polarisation and angle of polarisation of the samples were determined across a range of illumination angles and observation angles. The results were then plotted in ways to compare the polarimetric characteristics to those of the other materials, to the total reflected flux of the individual samples, and to the changes in illumination-sample-observer geometry. A Spectralon optical standard plate was used as a comparative measure.

The results of the experiment illustrate an ability for the techniques used to determine differences in the polarimetric characteristics of the samples with respect to the Spectralon, the illumination and observation geometry and between the different material samples. The results presented were qualitative in nature, with no intention or attempt made to understand the absolute polarimetric characteristics of either the polarimeter, or the samples themselves.

These results allowed a series of conclusions to be drawn. Primary amongst them is that the application of passive polarimetry to the challenge of characterizing Earth-orbiting resident space objects is worth further research to more fully appreciate its advantages and disadvantages. Additional conclusions were drawn that are intended to guide further research, and aid in the construction of an operational SSA polarimeter.

6.1 Future work

It is suggested that future work be conducted into three primary areas:

1. Understanding the absolute polarimetric characteristics of a wider range of specific spacecraft materials including multi-layer insulation, over a wider range of observation geometries including off-plane locations. This should include assessing the polarimetric behavior of samples comprising more than one material type.
2. Conduct investigations to understand the behavior of samples as they are rotated in more than one plane with respect to the source of illumination. Appreciating the impact of a rotating RSO with respect to the source of illumination will help assess the validity of observations made of orbiting spacecraft.
3. The construction, characterization and calibration of a polarimeter, of either an imaging design or making use of photon counting methods. This will allow for the assessment of the broad operating restrictions of polarimetry to observations of RSOs using small aperture telescopes.

These avenues of research will provide the data necessary to assess the validity of observations made using a polarimeter for the characterization of man-made Earth orbiting objects. As the nature of the polarisation characteristics of the reflected light is dependent upon the aspect of the RSO to the illumination source, having an appreciation of the impact of a rotating RSO is necessary to the understanding of any observations made.

Bibliography

- [1] NASA. Orbital Debris Quarterly News. Technical report, National Aeronautics and Space Administration, 2013.
- [2] J. Liou D. Kessler, N. Johnson and M. Matney. Telescope Syndrome: Implications to Future Space Operations. In *33rd Annual Guidance and Control Conference*, 2010.
- [3] P. LeVan. Discrimination of Closely Spaced Geosynchronous Satellites - Phase Curve Analysis and New Small Business Innovative Research Efforts. In *Proceedings of the 2010 AMOS Technical Conference, Kihii, Maui*, 2010.
- [4] D. Hall. AMOS Galaxy-15 Satellite Observations and Analysis. In *Proceedings of the 2011 AMOS Technical Conference, Kihii, Maui*, 2011.
- [5] P. Kervin. Anomaly Resolution Using Optical Signatures. In *Proceedings of the 2011 AMOS Technical Conference, Kihii, Maui*, 2011.
- [6] A. Jolley. Multicolour Optical Photometry of Active Geostationary Satellites Using a Small Aperture Telescope. Master's thesis, Royal Military College of Canada, 2014.
- [7] D. Bédard. *Spectrometric Characterization of Artificial Earth-Orbiting Objects*. PhD thesis, Royal Military College of Canada, 2013.
- [8] Robert D. Culp, Ian Gravseth, and Nicole King. Polarization Signals of Several Common Spacecraft Materials. Technical report, University of Colorado, 1996.
- [9] G. Giakos, S. Shrestha, T. Farrahi, J. Petermann, A. Deshpande, D. Godsoe, and E. Voudouri. Electro-Optical Polarimetric Imaging System for Characterization of Resident Space Objects. *Journal of Spacecraft and Rockets*, Vol 52, 2015.
- [10] Shih-Yau Lu and Russell A. Chipman. Interpretation of Mueller matrices based on polar decomposition. *J. Opt. Soc. Am. A*, 13(5):1106–1113, May 1996.
- [11] Michael C. Pasqual, Kerri L. Cahoy, and Eric L. Hines. Active Polarimetry for Orbital Debris Identification. In *AMOS2015 Technical Papers*. MIT, 2015.

-
- [12] W.A. Shurcliff. *Polarized Light; Production and Use*. Harvard University Press, 1962.
- [13] Eugene Hecht. *Optics - Second Edition*. Pearson Education Inc, 2002.
- [14] Eugene Hecht. *Optics - Fourth Edition*. Addison Wesley, 2004.
- [15] Frank Pedrotti and Leno Pedrotti. *Introduction to Optics - Second Edition*. Prentice-Hall International, Inc., 2005.
- [16] D. Clarke. *Stellar Polarimetry*. WILEY-VCH Verlag GmbH & Co. KGaA, 2010.
- [17] Tinbergen. *Astronomical Polarimetry*. Cambridge University Press, 1996.
- [18] M.J. Walker. Matrix Calculus and the Stokes Parameters of Polarized Radiation. *American Journal of Physics*, 22:170–174, 1954.
- [19] H.G. Berry, G. Gabrielse, and A.E. Livingston. Measurement of Stokes parameters of light. *Applied Optics*, 1977.
- [20] S. Johnston and J. Reynolds W. van Straten and, R. N. Manchester and. PSRCHIVE and PSRHITS: Definition of the Stokes Parameters and Instrumental Basis Conventions. *Astronomical Society of Australia*, 27:104–109, 2010.
- [21] D. Clarke and B. G. Stewart. *Statistical Methods of Stellar Polarimetry. Vistas in Astronomy*, 1986.
- [22] Michael Bass, Eric Van Stryland, David Williams, and William Wolfe. *Handbook of Optics - Volume II - Edition 2*. McGraw-Hill, Inc., 1995.
- [23] Raymond A. Serway. *Modern Physics - 3rd Edition*. Thomson, Brookes/Cole, 2005.
- [24] N.S. Fatemi, H.Q. Hou, P.R. Sharps, P.M. Martin, B.E. Hammons, and F. Spadafora. Development, space qualification, and production of high-efficiency large-area ingap/gaas dual-junction solar cells on Ge at emcore photovoltaics. In *Proceedings of the 16th Space Photovoltaic Research and Technology Conference, Cleveland, OH*, 1999.
- [25] Raymond A. Serway. *Physics for Scientists and Engineers with Modern Physics - 9th Edition*. Brookes/Cole, 2014.
- [26] F. E. Nicodemus. Reflectance Nomenclature and Directional Reflectance and Emissivity. *Appl. Opt.*, 9(6):1474–1475, Jun 1970.
- [27] Sylvia C. Pont and Jan J. Koenderink. Bidirectional Reflectance Distribution Function of Specular Surfaces with hemispherical Pits. *Journal of the Optical Society of America*, 19:2456–2466, 2002.
- [28] Anak Bhandari, Børge Hamre, Øvynd Frette, Lu Zhao, Jakob J. Stamnes, and Morten Kildemo. Bidirectional reflectance distribution function of Spectralon white reflectance standard illuminated by incoherent unpolarized and plane-polarized light. *Appl. Opt.*, 50(16):2431–2442, Jun 2011.
- [29] P. Kervin, D. Hall, M. Bolden, and J. Toth. Phase Angle: What is it Good For? In *Proceedings of the 2010 AMOS Technical Conference*, 2010.

-
- [30] M.S. Bessel. UVBRI Passbands. *Publications of the Astronomical Society of the Pacific*, 102:1181–1199, 1990.
- [31] T.E. Payne, S.A. Gregory, D. Payne, L. Kann, D. Sanchez, D. Werling, C. Davis, and L. Finker. Determination of Photometric Filters for Satellite Observations Using SILC Data. In *Proceedings of the 2000 Space Control Conference*, 2000.
- [32] T. E. Payne, S. A. Gregory, D. J. Sanchez, T. W. Burdillis, and S.A. Storm. Color Photometry of Geosynchronous Satellites Using the SILC Filters. In *SPIE 4490*, 2001.
- [33] H. Cowardin. *Characterization of Orbital Debris Objects Over Optical Wavelengths via Laboratory Measurements*. PhD thesis, University of Houston, 2010.
- [34] F. J. Vrba, H. F. Fliegel, and L.F. Warner. Optical brightness measurements of the GPS Block II, IIA and IIR Satellites on Orbit. In *Proceedings of the 2003 AMOS Technical Conference, Kihei, Maui*, 2003.
- [35] Steve B. Howell. *Handbook of CCD Astronomy - Second Edition*. Cambridge University Press, 2006.
- [36] K. Jorgensen, J. Okada, M. Guyote, K. Hamada, and E. Barker. Reflectance Spectra of human-made space objects. In *Proceedings of the 2004 AMOS Technical Conference*, 2004.
- [37] D.L. Bowers, L.D. Welles, M.J. Duggin, W. Glass, and L.G. Vaughn. Broad-band Spectral-polarimetric BRDF Scan System and Data for Spacecraft Materials. In *Proceedings of the 2011 AMOS Technical Conference, Kihei, Maui*, 2011.
- [38] G.C. Giakos, Richard H. Picard, and Phan D. Dao. Super-resolution Multispectral Imaging Polarimetric Space Surveillance LADAR Sensor Design Architectures. *SPIE Europe Remote Sensing*, 7107, 2008.
- [39] Hans Mueller. Foundations of Optics. *Journal of the Optical Society of America*, 38:661, 1948.
- [40] Dennis H. Goldstein. Polarization Signature Research. Technical report, Air Force Research Laboratory - Munitions Directorate, 2003.
- [41] Mahmoud Amin Nolan Quinn Roger Alayo Suman Shrestha, George Giakos. Polarimetric Characterization of Unresolved Space Objects. *Journal of Spacecraft and Rockets*, 2015.
- [42] Jeff Petermann. Design of a Fully Automated Polarimetric Imaging System for Remote Characterization of Space Materials. Master's thesis, University of Akron, 2012.
- [43] Oyvind Svensen, Morten Kildemo, Jerome Maria, Jakob J. Stamnes, and Oyvind Frette. Mueller Matrix Measurement and Modeling Pertaining to Spectralon White Reflectance Standards. *Optics Express*, 20, 2012.

- [44] D. B. Chenault, D. H. Golstein, and D. H. M. Hayes. Fourier Transform Spectropolarimetry for Optical Diagnostics of Transmissive Materials. Technical report, SY Technology, Air Force Research Laboratory, University of North Texas, 1998.
- [45] Thorlabs Inc. Economy Glass Polarizer Transmission Data. Website, 2015. Excel Spreadsheet.
- [46] Frederick R. Chromey. *To Measure the Sky: An Introduction to Observational Astronomy*. Cambridge University Press, 2010.
- [47] David A. Bohlender and Dmitry Monin. The Dominion Astrophysical Observatory Magnetic Field Survey (DMFS). In *Proceedings of the IAU Symposium No. 302*, 2013.
- [48] Juan M Bueno. Polarimetry using liquid-crystal variable retarder: theory and calibration. *Journal of Optics*, 2:2216–222, 2000.
- [49] Chun Ye. Construction of an Optical Rotator using quarter-wave plates and and optical retarder. *Optical Engineering*, 34(10):3031–3035, 1995.
- [50] M. K. Swami, S. Manhas, P. Buddhiwant, N. Ghosh, A. Uppal, and P.K. Gupta. Polar Decomposition of 3x3 Mueller Matrix: A tool for Quantitative Tissue Polarimetry. *The Journal of the Optical Society of America*, 14:9324–9337, 2006.

Appendices

A Stokes Parameters

A definition for the Stokes values based on those presented by Shurcliff [12], and refreshed by Hecht[13] provides a description based on the ‘operational use’ of the values, as opposed to a definition based on electromagnetic theory.

Consider a set of four filters, each of which would transmit half of the natural (unpolarised) light incident upon it. Unpolarised light is incident upon the first filter, which allows half to be transmitted. The filter does not affect the nature of the light in any way; it is essentially isotropic except for the transmittance value. A perfect detector is then placed behind the filter and the flux density of radiation (or irradiance) is measured and given a value of I_1 . This value is used in determining the first Stokes Parameter (I);

$$I = 2I_1 \tag{A.1}$$

Note, I could also be thought of as the total intensity of light incident upon the first filter.

The second filter is now placed in the beam, replacing the first. This filter will only allow the transmission of light that has a horizontal polarisation (when correct consideration of a coordinate system has been completed). That is, this filter is opaque to the vertical component of the natural light incident upon it. The detector is read with the intensity value (I_2) used to calculate the second Stokes parameter Q by;

$$Q = 2I_2 - 2I_1 \tag{A.2}$$

The value Q allows insight into the state of polarisation of the light; if Q is greater than 0 then a trend towards a state of horizontal polarisation is present, and conversely if Q is less than 0 a trend towards vertical polarisation is present. If no preference is shown, (ie, $Q = 0$), the beam could be thought to be elliptically polarised with an axis at $\pm 45^\circ$, completely circularly

polarised or completely unpolarised. It is worth noting that as the incident light was natural, or completely unpolarised, the horizontal component of the light would be half of the total with the other half being vertical.

Next, the third filter replaces the second which has its axis of polarisation positioned at 45° to the horizontal. The same detector is used, with the value (I_3) read to produce the third Stokes parameter U given by:

$$U = 2I_3 - 2I_1 \quad (\text{A.3})$$

where a value greater than 0 indicates a preference for polarisation vibration to be in the $+45^\circ$ direction (in the 1st and 3rd quadrants), and -45° direction (in the 2nd and 4th quadrants) if less than zero. If both Q and U are zero indicating no linear or elliptical polarisation preference, then the last polarisation state available to be tested for is whether the light has a circular direction preference.

To confirm what direction (either left hand or right hand) the circularly polarised light prefers, the fourth filter is used. This filter allows only right-handed circularly polarised light through to the detector, producing an intensity I_4 , and produces the Stokes Parameter V by:

$$V = 2I_4 - 2I_1 \quad (\text{A.4})$$

with a value for V greater than 0 indicating a right hand polarisation tendency, and less than 0 for left handed.

Lastly if the beam shows absolutely no tendency for polarisation, then;

$$Q = U = V = 0 \quad (\text{A.5})$$

which agrees with the discussion that there is no discernible preference to a direction, be it linear or major axis of an ellipse, nor is there a rotation direction preference for perfectly circular polarisation. It follows that the only option is for the light to be completely unpolarised, as was the assumption at the start of the operational derivation.

B Mueller calculus and decomposition

The Mueller matrix decomposition is a process by which the polarising characteristics of a material can be found through the use of illumination light of known polarisation states, and capturing the Stokes vector of the resulting reflection. A basic understanding of Mueller calculus is presented in order to aid the reader in understanding the process of Mueller matrix decomposition.

B.1 Mueller calculus

The explanation begins with the understanding that a surface can have an effect on the polarisation characteristics of the light incident upon it. The polarisation characteristics of the material can be described by a real 4x4 matrix called the Mueller matrix \mathbf{M} [13, 22] that transforms the incident light into the reflected light. This relation is illustrated by;

$$\vec{\mathbf{S}}_{out} = \mathbf{M}\vec{\mathbf{S}}_{in} \quad (\text{B.1})$$

where $\vec{\mathbf{S}}_{in}$ is the Stokes vector of the incident light, and \mathbf{S}_{out} is the reflected (or transmitted) light. It should be noted that the Mueller matrix for a material is a function of both the direction of propagation of the light and its wavelength [22].

If the light travels through or is reflected off more than one surface or medium, then the Muller matrix for each surface can be included in turn. The order through which the Mueller matrices are considered is important as matrix multiplication is not commutative. A practical appreciation of this can be gained by considering Equation B.1 a second time, where \mathbf{S}_{out} for the first surface Mueller Matrix \mathbf{M}_1 becomes the input light Stokes vector for the

second surface \mathbf{M}_2 . That is, the first surface interacted with is dealt with last in the Mueller calculus operation.

The relation now becomes;

$$\vec{\mathbf{S}}_{out} = \mathbf{M}_2 \mathbf{M}_1 \vec{\mathbf{S}}_{in} \quad (\text{B.2})$$

This process is important for the characterization process of optical instruments as the polarisation characteristics of each optical element within the light collecting system needs to be considered in order correctly.

A simple example of the method of Mueller calculus can be seen with the theoretical application of a linear polariser. Consider incident light (\mathbf{S}_{in}) that is perfectly linearly polarised with a $45/225^\circ$ orientation, that is, existing only in the 1st and 3rd quadrants. The Stokes vector for light with these characteristics is:

$$\mathbf{S}_{in} = \begin{bmatrix} 1 \\ 0 \\ 1 \\ 0 \end{bmatrix} \quad (\text{B.3})$$

and the Mueller matrix for a linear polariser (\mathbf{M}_{lin}) with a fast axis aligned along the x axis is given by:

$$\mathbf{M}_{lin} = \begin{bmatrix} 0.5 & 0 & 0 & 0 \\ 0 & 0.5 & 0 & 0 \\ 0 & 0 & 0 & 0 \\ 0 & 0 & 0 & 0 \end{bmatrix} \quad (\text{B.4})$$

The relation in Equation B.1 can then be formed and the result calculated:

$$\begin{bmatrix} 0.5 & 0 & 0 & 0 \\ 0 & 0.5 & 0 & 0 \\ 0 & 0 & 0 & 0 \\ 0 & 0 & 0 & 0 \end{bmatrix} \begin{bmatrix} 1 \\ 0 \\ 1 \\ 0 \end{bmatrix} = \begin{bmatrix} 0.5 \\ 0.5 \\ 0 \\ 0 \end{bmatrix} \quad (\text{B.5})$$

with inspection showing that the resultant Stokes vector agrees with what we know is the horizontal component of the polarisation orientation of the incident light.

B.2 Mueller decomposition

If a material of unknown polarimetric characteristics is illuminated by light with a known polarisation state and the Stokes parameters of the reflected (or transmitted) light calculated, then information about the nature of the material's optical nature can be determined. This process is referred to as Mueller matrix decomposition or Lu-Chipman decomposition [9–11, 22].

The premise of the process is that the Mueller matrix for a surface \mathbf{M} can be de-constructed to three component characteristics, namely; diattenuation (\mathbf{M}_D), retardance (\mathbf{M}_δ) and depolarisation, otherwise known as polarizance (\mathbf{M}_P), where;

$$\mathbf{M} = \mathbf{M}_D \cdot \mathbf{M}_\delta \cdot \mathbf{M}_P \quad (\text{B.6})$$

In order to determine the 16 individual elements of the 4x4 Mueller matrix however, a system of 16 independent equations needs to be constructed with 16 different pairs of incident and received polarisation states used [11]. These are shown in Figure B.1. The $I_{\text{subscript}}$ values are the measured intensities of light with the subscript pair of incident and detected polarisation components and H , V , $+45$ and RC refer to horizontal, vertical, 45° and right hand circularly polarised light respectively.

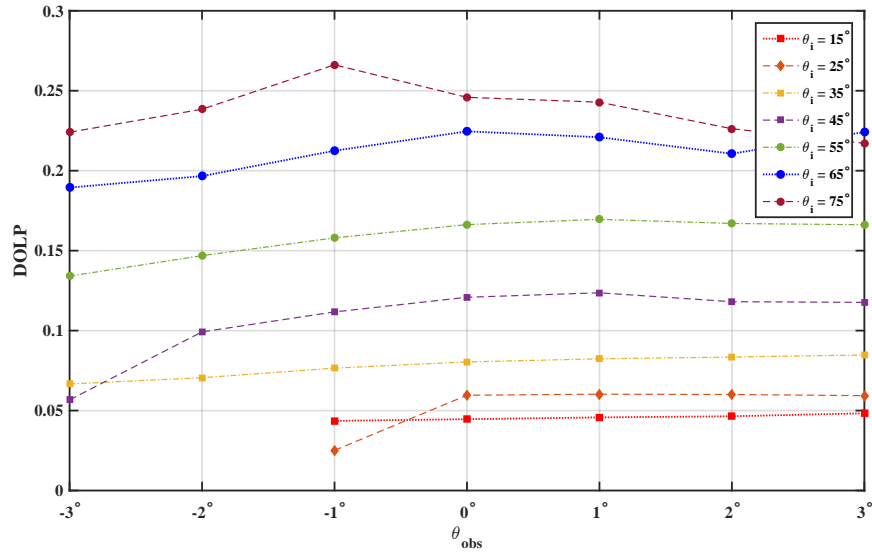
		Illumination Polarisation			
		H	V	+45	RC
Detected Polarisation	H	I_{HH}	I_{VH}	I_{+45H}	I_{RCH}
	V	I_{HV}	I_{VV}	I_{+45V}	I_{RCV}
	+45	I_{H+45}	I_{V+45}	I_{+45+45}	I_{RC+45}
	RC	I_{HRC}	I_{VRC}	I_{+45RC}	I_{RCRC}

Figure B.1: Description of the 16 individual illumination/detected polarisation characteristic pairs used in a full Lu-Chipman Muller matrix decomposition. Adapted from Pasqual *et al.* [11].

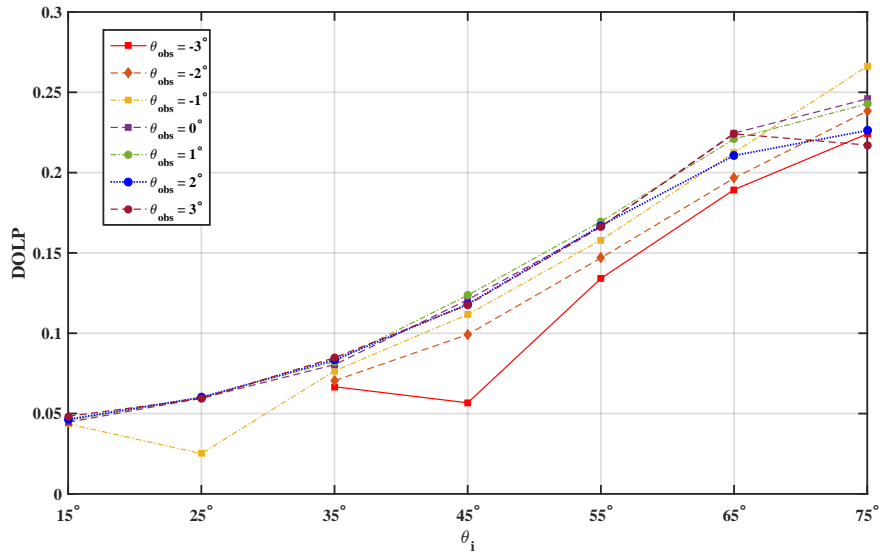
These include all possible combinations of vertical, horizontal, circularly left and right handed polarisation states [50]. With active polarimetry this is possible by controlling the nature of the incident light as well as well as which component of the reflected light is measured.

C Results

C.1 Aluminum

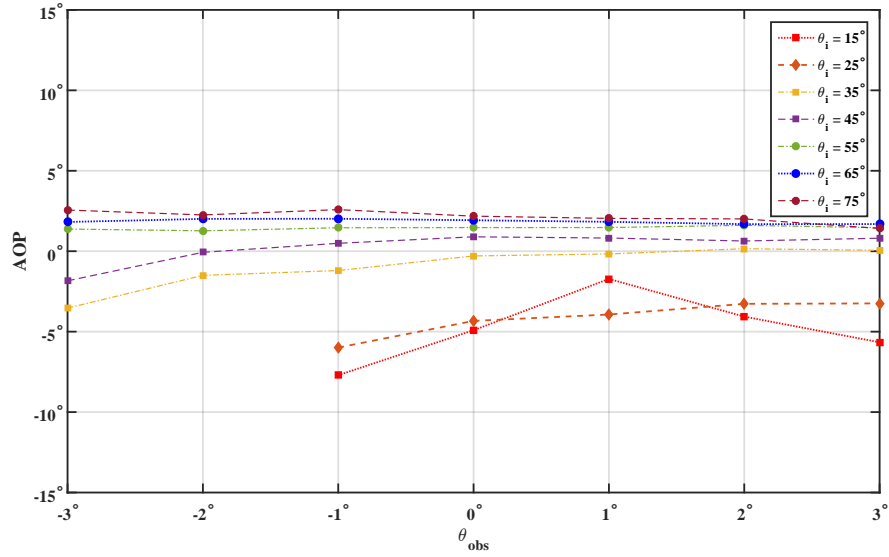


(a) Observation angle

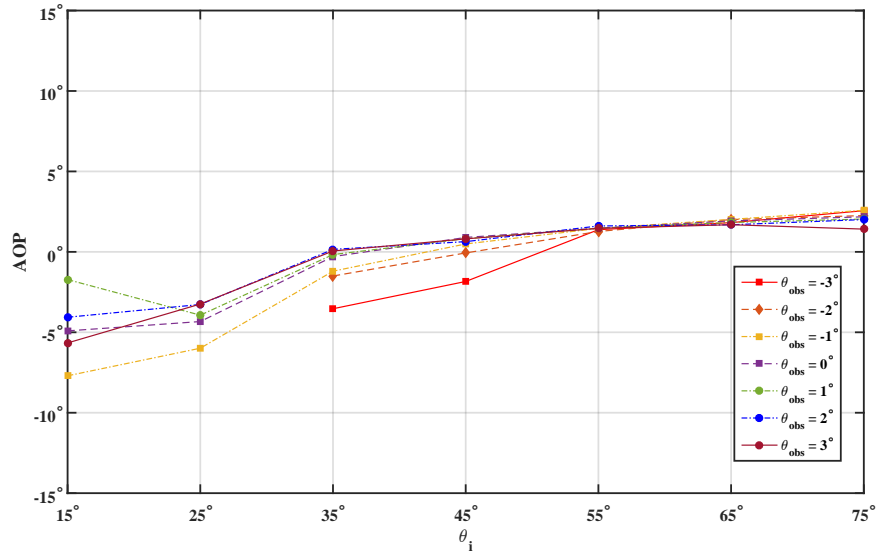


(b) Illumination angle

Figure C.1: 6061T6 DOLP with respect to θ_{obs} and θ_i .



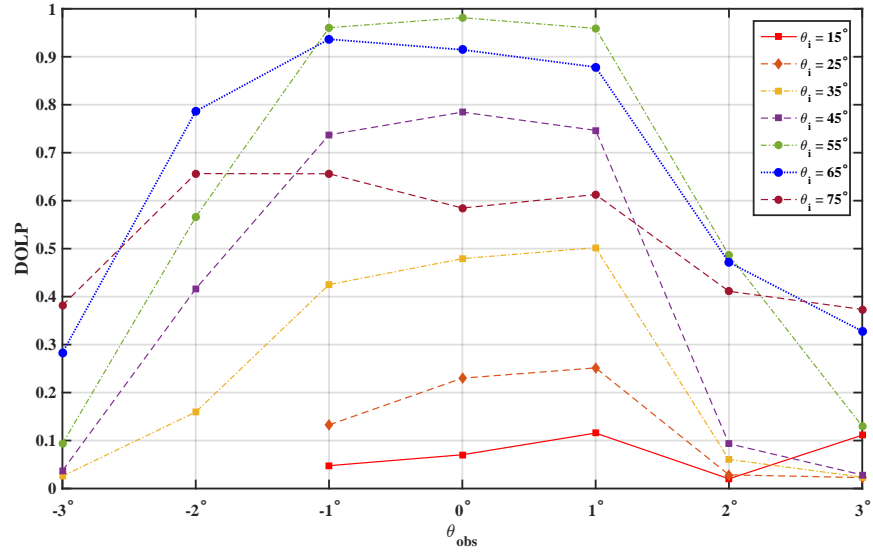
(a) Observation Angle



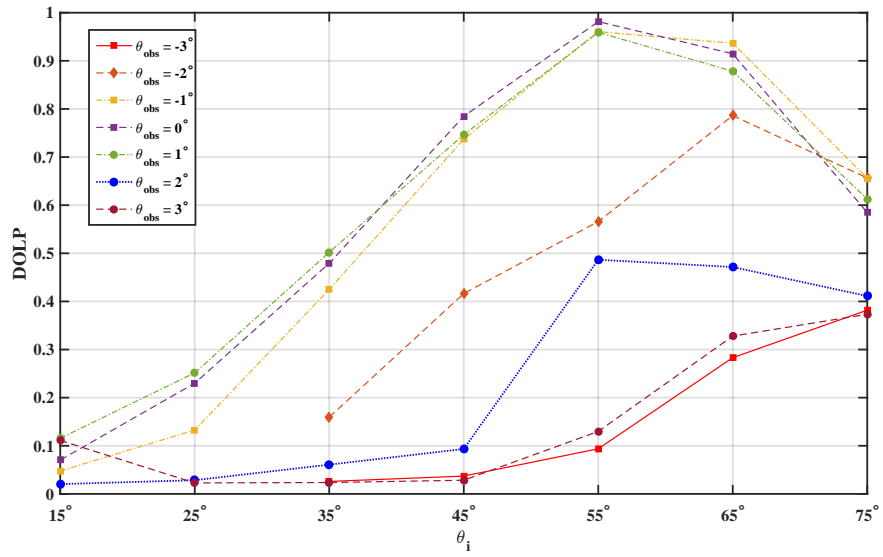
(b) Illumination angle

Figure C.2: 6061T6 AOP with respect to θ_{obs} and θ_i .

C.2 White panel

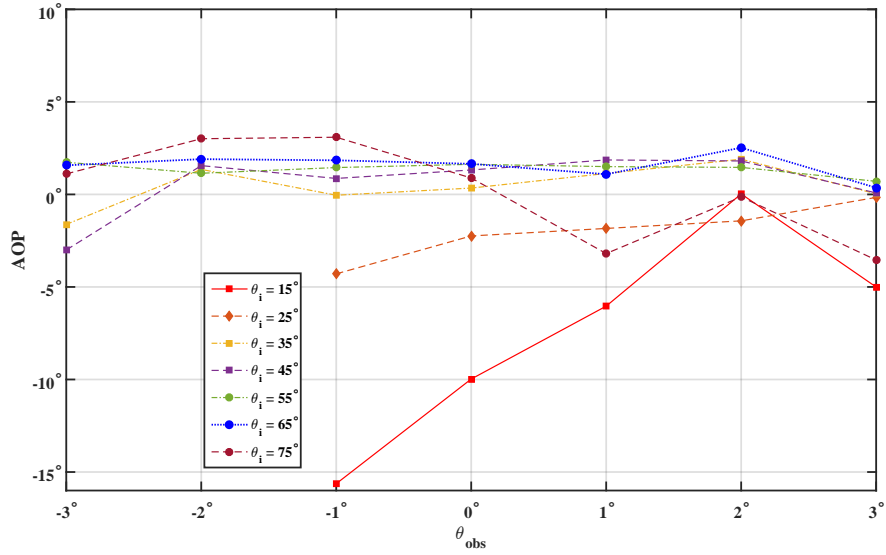


(a) Observation angle

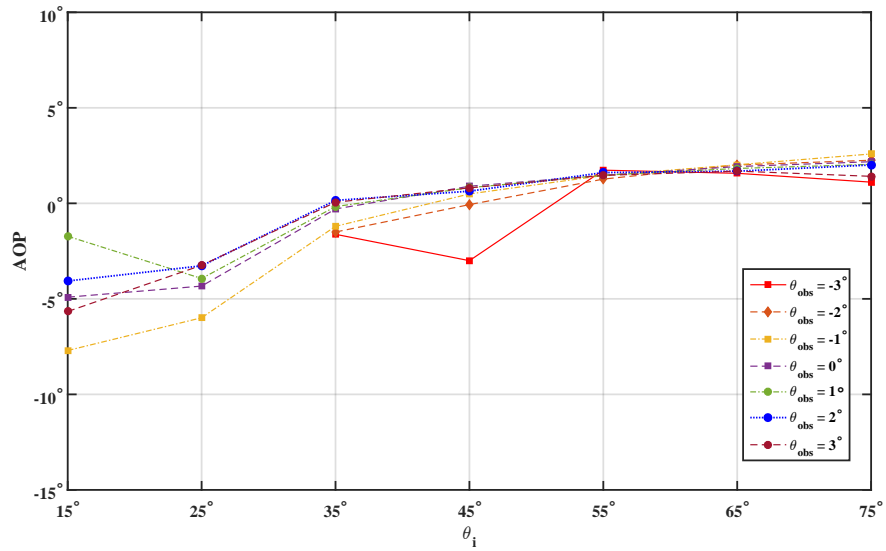


(b) Illumination angle

Figure C.3: White painted panel DOLP with respect to θ_{obs} and θ_i .



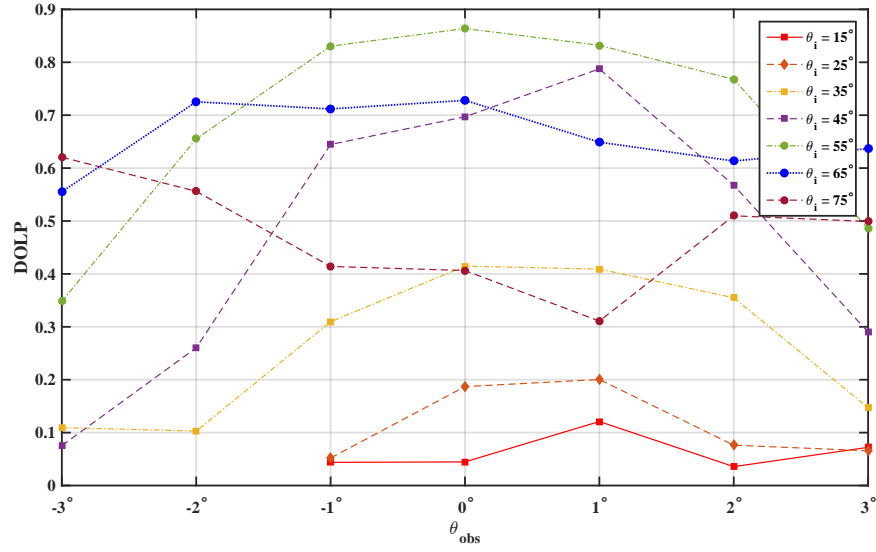
(a) Observation Angle



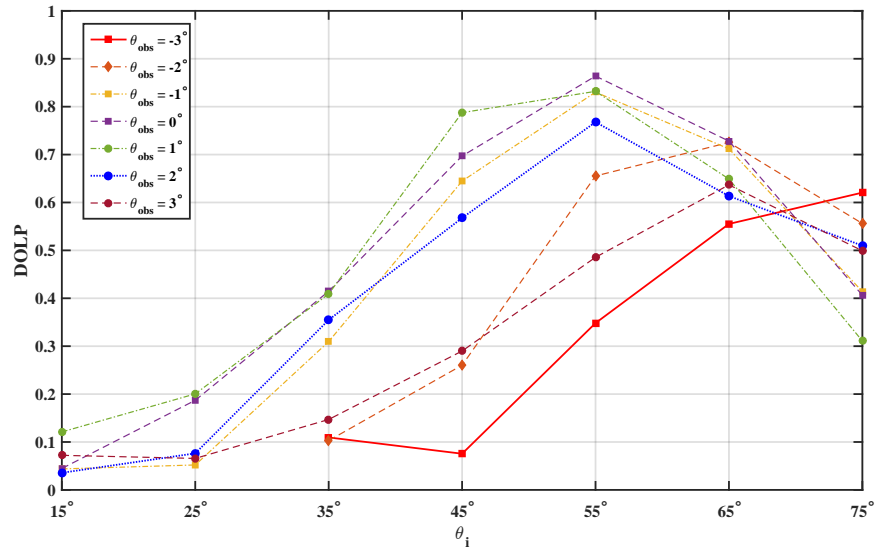
(b) Illumination angle

Figure C.4: White painted panel AOP with respect to θ_{obs} and θ_i .

C.3 Emcore TJPV cell

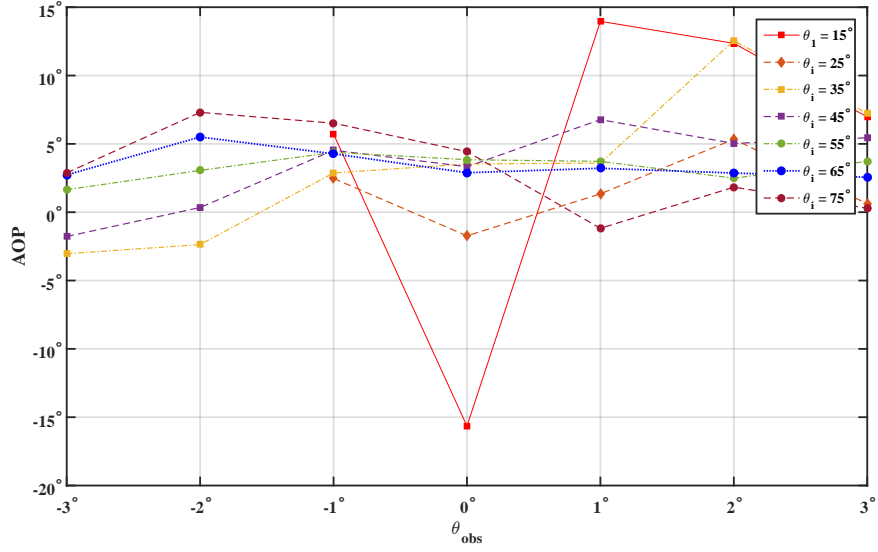


(a) Observation angle

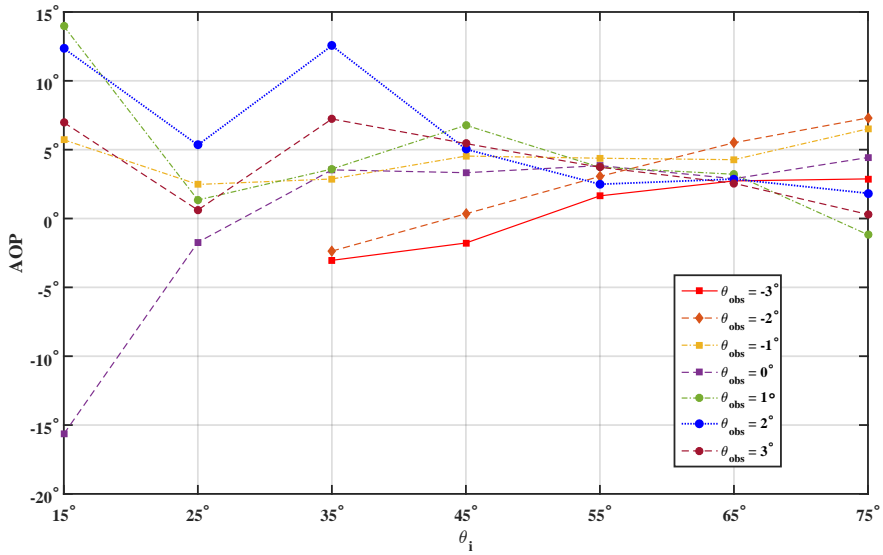


(b) Illumination angle

Figure C.5: Emcore TJPC cell DOLP with respect to θ_{obs} and θ_i .



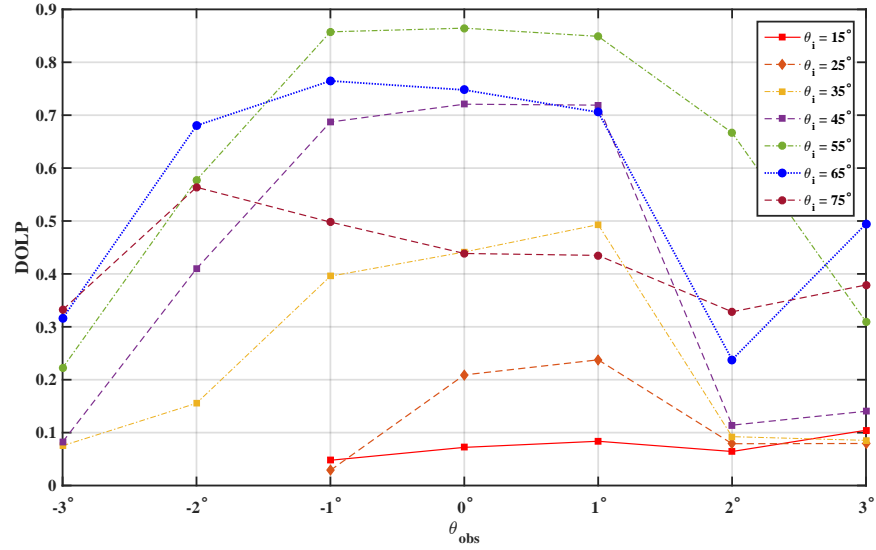
(a) Observation Angle



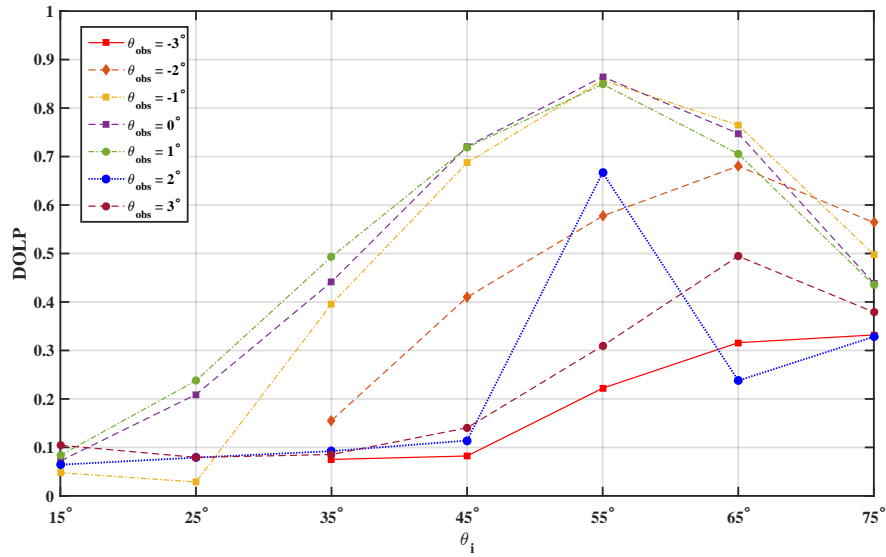
(b) Illumination angle

Figure C.6: Emcore TJPV cell AOP with respect to θ_{obs} and θ_i .

C.4 Azur TJPV cell

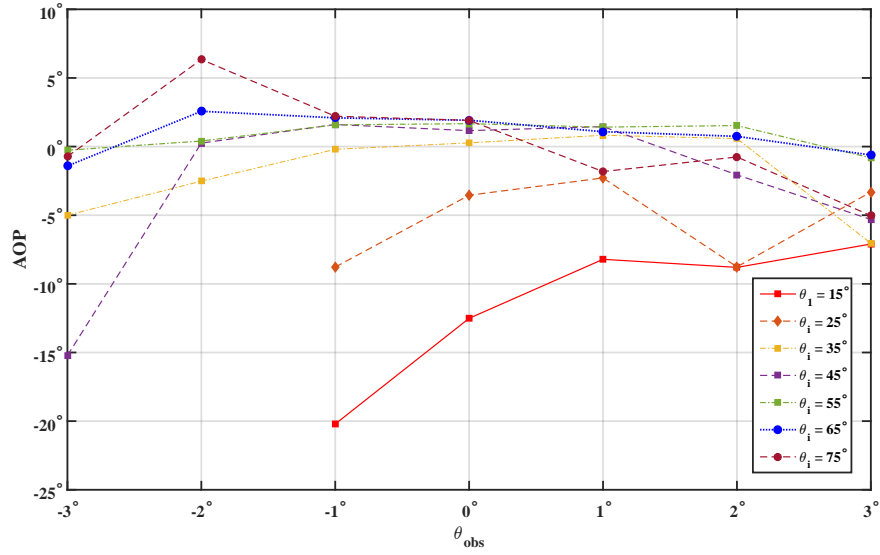


(a) Observation angle

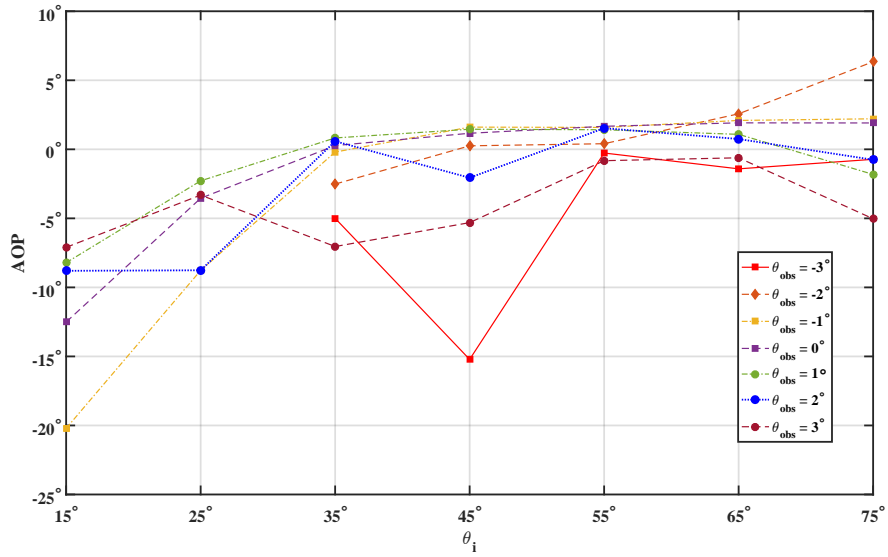


(b) Illumination angle

Figure C.7: Azur TJPC cell DOLP with respect to θ_{obs} and θ_i .



(a) Observation Angle



(b) Illumination angle

Figure C.8: Azur TJPV cell AOP with respect to θ_{obs} and θ_i .

D Resume

Name:	Carl Clancy	
Place of birth:	Yass, New South Wales, Australia	
Year of birth:	1983	
Post-secondary education and degrees:	Masters candidate	2014 - 2016
	Royal Military College of Canada Kingston, Ontario	
	Diploma of Air Force studies	2015
	School of Post-graduate Studies, RAAF Wagga Wagga, NSW	
	Southern Hemisphere Summer Session Program	2014
	International Space University Strasbourg, France	
	B.Tech. (Aviation)	2002 - 2004
	Australian Defence Force Academy Canberra, ACT	

Employment history:	Officer in Charge Space Flight Surveillance Crew Commander No.1 Radar Surveillance Unit Adelaide, SA	2012 - 2014
	Weapons Team Leader Surveillance Crew Commander No.3 Control and Reporting Unit, Williamtown, NSW	2008 - 2011
	Air Combat Officer OP SLIPPER Afghanistan	2008 - 2009
	Air Battle Managers Basic Course Surveillance and Control Training Unit, Williamtown NSW	2007 - 2008
	Basic Pilots Course ADF Basic Flying Training School Tamworth, NSW Perth, WA	2005 - 2007
Honors and awards:	Air Battle Managers Course Academic Dux Surveillance and Control Training Unit, NSW	2008
	JTF633 Commander's Commendation OP SLIPPER	2009